




# Heavy-heavy and heavy-light mesons in cold nuclear matter

Jésus J. Cobos-Martínez<sup>1</sup> , Guilherme N. Zeminiani<sup>2</sup> , and Kazuo Tsushima<sup>\*2</sup> 

<sup>1</sup> Departamento de Física, Universidad de Sonora, Boulevard Luis Encinas J. y Rosales, Colonia Centro, Hermosillo, Sonora 83000, México

<sup>2</sup> Laboratório de Física Teórica e Computacional (LFTC), Programa de Pósgraduação em Astrofísica e Física Computacional, Universidade Cidade de São Paulo (UNICID), 01506-000, São Paulo, SP, Brazil

\* Corresponding author: kazuo.tsushima@gmail.com, kazuo.tsushima@cruzeirodosul.edu.br

**Abstract:** We review the in-medium modifications of effective masses (Lorentz scalar potentials or phenomenon of mass shift) of heavy-heavy and heavy-light mesons in symmetric nuclear matter and their nuclear bound states. We use a combined approach with the quark-meson coupling (QMC) model and an effective Lagrangian. As demonstrated by the cases of pionic and kaonic atoms, studies of meson-nucleus bound state can provide us with important information on chiral symmetry in dense nuclear medium. In this review, we treat the mesons,  $K, K^*, D, D^*, B, B^*, \eta, \eta', \phi, \eta_c, J/\psi, \eta_b, Y$ , and  $B_c$ , where our emphasis is on the heavy mesons. In addition, we also present some new results for the  $B_c$ -nucleus bound states.

**Keywords:** Hadrons; nuclear matter; strong interactions; chiral symmetry restoration in medium

## 1. Introduction

Quantum chromodynamics (QCD) is the theory of strong interactions at the fundamental level, namely, at the level of quarks and gluons which compose the observed hadrons in the standard model (SM) [1–7]. However, a quantitative understanding of the strong force and strongly interacting matter from the underlying first principles of QCD is still limited, in particular when the hadrons are under the circumstance of many nucleons such as emerged in nuclei and dense nuclear medium. The study of the interactions of heavy-heavy and heavy-light mesons with atomic nuclei is an important tool for understanding the properties of strongly interacting matter in vacuum and in extreme conditions of temperature and density based on QCD Refs. [8–15]. In this review we treat the zero temperature case. The understanding of hadronic interactions with the nuclear medium is imperative for studying the production of heavy mesons in high energy heavy ion collisions [16,17], because the medium modifications of hadron properties may have a significant impact on the experimental results. Decay processes and decay rates involving mesons in a nuclear medium should also be modified. For example, decays of the type  $B_c \rightarrow D_s \ell^+ \ell^-$  involving a flavor-changing neutral-current process are highly suppressed in the Standard Model (SM) [18–24], thus being very important for investigating the physics beyond the SM. Moreover, the suppression or enhancement in the production of mesons such as  $J/\psi, Y$ , and  $B_c$  makes them interesting probes of quark-gluon plasma (QGP) [25–34].

To calculate the in-medium (effective) masses of the mesons that contain light quarks, such as  $K, K^*, D, D^*, B, B^*, \eta$  and  $\eta'$ , we use the quark-meson coupling (QMC) model [35]. Because of the Okubo-Zweig-Iizuka (OZI) rule, the heavy quarkonium-nucleus interaction via the exchange of mesons made of only light quarks is suppressed, so that the quarkonium-nucleus interaction is primarily by a QCD van der Waals type interactions [36]. For the mesons that do not contain light quarks, namely,  $\phi, \eta_c, J/\psi, \eta_b, Y$ , and  $B_c$ , we employ a combined approach, in which the mechanism for the meson interact with the nuclear medium through the excitation of the intermediate-state mesons which do contain light quarks, in the self-energy. Where the in-medium masses of the intermediate-state mesons

**Citation:** Lastname, F.; Lastname, F.; Lastname, F. Title. *Journal Not Specified* 2024, 1, 0. <https://doi.org/>

Received:

Revised:

Accepted:

Published:

**Copyright:** © 2025 by the authors. Submitted to *Journal Not Specified* for possible open access publication under the terms and conditions of the Creative Commons Attribution (CC BY) license (<https://creativecommons.org/licenses/by/4.0/>).

are calculated by the QMC model, and the meson self-energies are estimated with effective Lagrangians.

Partial restoration of chiral symmetry, and chiral symmetry itself in nuclear medium, are another interesting phenomena that can be studied in an empirical sense, because the (effective) mass reduction of the medium-modified hadron may be associated with a signature of partial restoration of chiral symmetry [37–40]. This negative mass shift can be regarded as an attractive Lorentz scalar potentials, that, if sufficiently attractive, can bind mesons to atomic nuclei. Deeply bound pionic atoms were first discussed in 1985 [41], and later observed in the  $^{208}\text{Pb}(d, {}^3\text{He})$  reaction [42]. In addition, studies of kaonic atoms were performed [43–47]. The studies of the pionic and kaonic atoms can provide us with very important information on chiral symmetry in dense nuclear medium. Furthermore, other possible meson-nucleus bound states were proposed [48–50]. Charmonium-nucleus systems were proposed in 1989 [51], followed by many predictions [8,10,11,36–38,52–67]. Lattice QCD have also predicted such states [68–70], and also  $\phi$ -nucleon bound states [71]. In the bottom sector of quarkonia, strong nuclear bound states with various nuclei [72–75] were predicted for  $Y$  and  $\eta_b$ . In this article, we review the downward shift of meson masses in nuclear matter, and the meson-nucleus bound states focusing on the heavy-heavy and heavy-light mesons. We also comment on some new results for the  $B_c$ -nucleus bound states.

This review is organized as follows. In Section 2 we present the details of quark-meson coupling (QMC) model needed to understand better most of our results. In Section 3 we present the results for the mass shift of mesons with heavy-light quark content using the quark-meson coupling (QMC) model. Since heavier flavor quarks  $Q = s, c, b$  do not directly interact directly with the mean fields in a nuclear medium, to compute the effective masses for the mesons with a (heavy quark)-(heavy antiquark) content, we use a combined approach using both the QMC model with and effective Lagrangians. We describe this in Section 4. In Section 5, using the calculated amounts of the downward shift of masses for the mesons considered in this work, we present our results for the meson-nucleus potentials for various nuclei in a wide range of nuclear masses. Using the meson-nucleus potentials obtained in the previous section, in Section 6 we present our results for meson-nucleus bound state energies and widths for some mesons) by solving the Klein-Gordon equation. Finally, in Section 7 we present a summary and conclusions.

## 2. The quark-meson coupling (QMC) model

The quark-meson coupling (QMC) model, the standard version we use, is a quark-based model for nuclear matter and nuclei that describes the internal structure of the nucleons using the non overlapping MIT bag model, and the binding of nucleons (nuclear matter) by the self-consistent couplings of the confined light quarks  $u$  and  $d$  to the Lorentz scalar- $\sigma$ , Lorentz-vector-isoscalar- $\omega$  and Lorentz-vector-isovector- $\rho$  meson mean fields generated by the confined light quarks in the nucleons [35].

In a nuclear medium, the hadrons with light quarks are expected to be modified their properties predominantly, such as evidenced by the European Muon Collaboration effect [76,77] and the modifications of bound proton electromagnetic form factors [78,79]. Thus, one can expect that the nuclear medium can modify the internal structure of nucleons and hadrons, and can affect the interaction with nucleons. Thus, to study such effects due to the hadron internal structure based on the quarks and gluons, can make the QMC model a useful phenomenological tool to describe the change of the internal structure of hadrons in a nuclear medium.

The QMC model has been successfully applied for the studies of various properties of infinite nuclear matter and finite (hyper)nuclei [11,80–83]. Here we briefly present the necessary details to understand our results better. For more detailed discussions and some successful features of the model, see Refs. [11,80,81,83], and references therein.

We consider nuclear matter (NM) in its rest frame, where all the scalar and vector mean field potentials, which are responsible for the nuclear many-body interactions, are constants in Hartree approximation. We assume  $SU(2)$  symmetry for the quarks ( $m_q = m_u = m_d$  and

$q = u$  or  $d$ ). Note that, the heavier quarks  $Q = s, c, b$  (we will denote simply heavy quarks as  $Q$  hereafter including the  $s$  quarks) are not affected directly by the mean field potentials in the standard QMC model. Thus, when dealing with mesons composed of valence (heavy quark)-(heavy antiquark) pairs, we will have to proceed in a different manner for hidden flavor heavier mesons with  $Q = s, c, b$  and two-heavy-flavored mesons such as  $B_c$  and  $B_s$  mesons. In this study, we will treat the  $B_c$  and  $B_c^*$  mesons only; however, for the other two-heavy-flavored mesons  $B_s, B_s^*, D_s$  and  $D_s^*$  mesons, see Ref. [84].

The Dirac equations for the quarks and antiquarks in nuclear matter (neglecting the Coulomb force), in a bag of a hadron,  $h$ , ( $q = u$  or  $d$ , and  $Q = s, c$  or  $b$ ), are given by ( $x = (t, \mathbf{r})$  and for  $|\mathbf{r}| \leq \text{bag radius}$ ) [50,85–88],

$$\left[ i\gamma \cdot \partial_x - (m_q - V_\sigma^q) \mp \gamma^0 \left( V_\omega^q + \frac{1}{2} V_\rho^q \right) \right] \begin{pmatrix} \psi_u(x) \\ \psi_{\bar{u}}(x) \end{pmatrix} = 0, \quad (1)$$

$$\left[ i\gamma \cdot \partial_x - (m_q - V_\sigma^q) \mp \gamma^0 \left( V_\omega^q - \frac{1}{2} V_\rho^q \right) \right] \begin{pmatrix} \psi_d(x) \\ \psi_{\bar{d}}(x) \end{pmatrix} = 0, \quad (2)$$

$$[i\gamma \cdot \partial_x - m_Q] \psi_Q(x) = 0, \quad [i\gamma \cdot \partial_x - m_Q] \psi_{\bar{Q}}(x) = 0, \quad (3)$$

where, the mean field potentials are defined by,  $V_\sigma^q \equiv g_\sigma^q \sigma$ ,  $V_\omega^q \equiv g_\omega^q \omega$ , and  $V_\rho^q \equiv g_\rho^q b$ , with  $g_\sigma^q, g_\omega^q$ , and  $g_\rho^q$  being the corresponding quark-meson coupling constants. We assume SU(2) symmetry,  $m_q = m_{\bar{q}} \equiv m_{u,\bar{u}} = m_{d,\bar{d}} \equiv m_{q,\bar{q}}$ . The Lorentz-scalar "effective quark masses" are defined by,  $m_q^* = m_{u,\bar{u}}^* = m_{d,\bar{d}}^* = m_{q,\bar{q}}^* \equiv m_q - V_\sigma^q$ , and thus  $m_q^*$  is dominated by  $-V_\sigma^q$  as baryon density increases, and can be negative, but one should not demand the positivity of usual particle mass, since this is nothing but the reflection of the strong attractive scalar potential. Note that,  $m_Q = m_Q^*$ , since the  $\sigma$  field does not couple to the heavier ("heavy") quarks  $Q = s, c, b$  in the QMC model. Furthermore, when we consider symmetric nuclear matter (SNM) with Hartree approximation, the  $\rho$ -meson mean field becomes zero,  $V_\rho^q = 0$ , in Eqs. (1) and (2), and we can ignore hereafter. However, when we consider the meson-nucleus bound states, the isospin dependent  $\rho$ -meson mean field, as well as the Coulomb potential in nuclei will be included if necessary. In this study, only the Coulomb potentials for the  $B_c$ -nucleus bound states will enter.

The static solution for the ground state quarks (antiquarks) in asymmetric nuclear matter (ANM) with a flavor  $f (= u, d, s, c, b)$  is written as  $\psi_f(x) = N_f e^{-i\epsilon_f t / R_h^*} \psi_f(\mathbf{r})$ , with the  $N_f$  being the normalization factor, and  $\psi_f(\mathbf{r})$  the corresponding spin and spatial part of the wave function.

The eigenenergies for the quarks and antiquarks in a hadron  $h$ , in units of the in-medium bag radius of hadron  $h$ ,  $1/R_h^*$ , are given by

$$\begin{pmatrix} \epsilon_u \\ \epsilon_{\bar{u}} \end{pmatrix} = \Omega_q^* \pm R_h^* \left( V_\omega^q + \frac{1}{2} V_\rho^q \right), \quad (4)$$

$$\begin{pmatrix} \epsilon_d \\ \epsilon_{\bar{d}} \end{pmatrix} = \Omega_q^* \pm R_h^* \left( V_\omega^q - \frac{1}{2} V_\rho^q \right), \quad (5)$$

$$\epsilon_Q = \epsilon_{\bar{Q}} = \Omega_Q, \quad Q = s, c, b. \quad (6)$$

The in-medium mass and bag radius of hadron  $h$  in the nuclear medium,  $m_h^*$  and  $R_h^*$  respectively, are determined from

$$m_h^* = \sum_{j=q,\bar{q},Q,\bar{Q}} \frac{n_j \Omega_j^* - z_h}{R_h^*} + \frac{4}{3} \pi R_\eta^{*3} B_p, \quad \left. \frac{dm_h^*}{dR_h} \right|_{R_h=R_h^*} = 0, \quad (7)$$

in particular, for the mesons  $h = K, K^*, D, D^*, B, B^*$ , while for the  $\eta$  and  $\eta'$  mesons, to take into account flavor mixing, these are given by

$$m_\eta^* = \frac{2[a_P^2\Omega_q^* + b_P^2\Omega_s] - z_\eta}{R_\eta^*} + \frac{4}{3}\pi R_\eta^{*3}B_P, \quad \left. \frac{dm_h^*}{dR_j} \right|_{R_h=R_h^*} = 0, \quad (h = \eta, \eta'), \quad (8)$$

$$a_P \equiv \sqrt{1/3}\cos\theta_P - \sqrt{2/3}\sin\theta_P, \quad b_P \equiv \sqrt{2/3}\cos\theta_P + \sqrt{1/3}\sin\theta_P \quad (9)$$

(for  $\eta'$ ,  $\eta \rightarrow \eta'$ , and  $a_P \leftrightarrow b_P$ ),

where  $m_q^* = m_q - V_\sigma^q$ ,  $m_Q^* = m_Q$  (as already mentioned),  $\Omega_q^* = \Omega_q^* = \left[ x_q^2 + (R_h^* m_q^*)^2 \right]^{1/2}$ ,  $\Omega_Q^* = \Omega_Q^* = \left[ x_Q^2 + (R_h^* m_Q)^2 \right]^{1/2}$ , with  $x_{q,Q}$  being the lowest mode bag eigenfrequencies;  $B_P$  is the bag constant;  $n_{q,Q}$  ( $n_{\bar{q},\bar{Q}}$ ) are the lowest mode valence quark (antiquark) numbers for the quark flavors  $q$  and  $Q$  in the corresponding mesons; and  $z_h$  parameterize the sum of the center-of-mass and gluon fluctuation effects and are assumed to be independent of density [89]. The MIT big parameters  $z_N$  ( $z_h$ ) and  $B_P$  are fixed by fitting the nucleon (hadron) mass in free space.

We choose the values  $(m_q, m_s, m_c, m_b) = (5, 250, 1270, 4200)$  MeV for the current quark masses, and  $R_N = 0.8$  fm for the free space nucleon bag radius. (See Ref. [90] for other values used  $(m_q, m_s) = (5, 93, 1270, 4180)$  MeV result.) The quark-meson coupling constants,  $g_\sigma^q, g_\omega^q$  and  $g_\rho^q$ , for the light quarks were determined by the fit to the saturation energy (-15.7 MeV) at the saturation density ( $\rho_0 = 0.15 \text{ fm}^{-3}$ ) of symmetric nuclear matter for  $g_\sigma^q$  and  $g_\omega^q$ , and by the bulk symmetry energy (35 MeV) for  $g_\rho^q$  [35,80]. The obtained values for the quark-meson coupling constants are  $(g_\sigma^q, g_\omega^q, g_\rho^q) = (5.69, 2.72, 9.33)$ .

Finally, for the mixing angle  $\theta_P$  appearing in Eq. (9), we use the value  $\theta_P = -11.3^\circ$ , neglecting any possible mass dependence and imaginary parts [90,91]. Furthermore, we also assume that the value of the mixing angle does not change in the nuclear medium.

### 3. Results with the QMC model

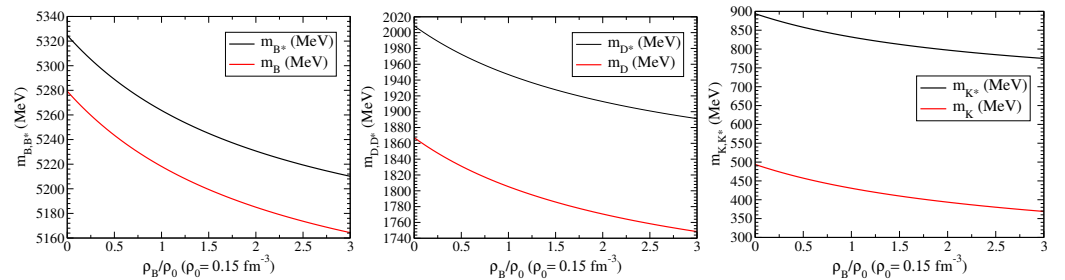


**Figure 1.**  $B$  and  $B^*$  (left panel),  $D$  and  $D^*$  (middle panel) and  $K$  and  $K^*$  (right panel) meson Lorentz-scalar effective masses in symmetric nuclear matter versus baryon density ( $\rho_B/\rho_0$ ), calculated with the QMC model.

In Figs. 1 and 2 we present respectively the QMC model predictions for the effective masses of  $B, B^*, D, D^*, K$  and  $K^*$  mesons [84], and the effective masses and the mass shift  $\Delta m_h(\rho_B) \equiv m_h^*(\rho_B) - m_h$  for  $\eta$  and  $\eta'$  mesons with  $m_h^*$  the in-medium meson mass and  $m_h$  the vacuum mass [123], in symmetric nuclear matter versus nuclear matter density  $\rho_0/\rho_B$ . Clearly, the masses of these mesons decrease in the nuclear medium, and this fact may be regarded as a signature of partial restoration of chiral symmetry in medium, although the QMC model does not explicitly have a chiral symmetry mechanism. Below, we will discuss and use the results shown in Figs. 1 and 2.

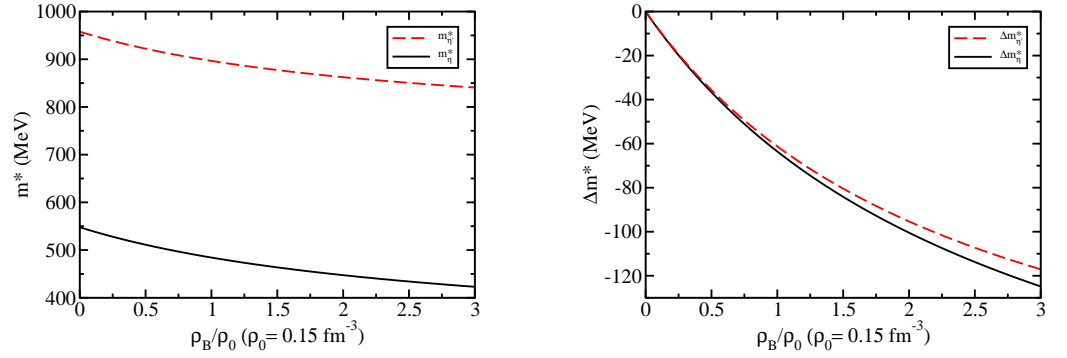


**Figure 2.**  $\eta$  and  $\eta'$  effective masses (left panel) and mass shift (right panel) in symmetric nuclear matter versus baryon density ( $\rho_B/\rho_0$ ), calculated with the QMC model.

#### 4. Combined the QMC model and effective Lagrangian approach

Since the Okubo-Zweig-Iizuka rule suppresses the interactions mediated by the exchange of mesons made of light quarks for the case of heavy-heavy mesons, it is therefore necessary to explore other potential sources of attraction which could potentially lead to the binding of heavy-heavy mesons to atomic nuclei. Furthermore since the heavy quarks  $Q = s, c, b$  do not directly interact with the mean fields in a nuclear medium (see Eqn. (3)), to compute the effective masses (Lorentz scalar potentials) for the mesons composed of a (heavy quark)-(heavy antiquark) pair, we take a different approach.

This approach consists of the combined treatment with the QMC model and an effective Lagrangian. We have already introduced the QMC model above, so we now describe the effective Lagrangian approach we rely on.

In the effective Lagrangian approach, mesons are treated as the structureless point-like particles, whose interactions are dictated by a local gauge symmetry principle. In order to be more explicit, we separate our study according to the different mesons. Part of the descriptions and treatments reviewed here have already been published in journals [67,72,75,100,101,115,123], as well as presented at various conferences [74,102–104,124,125].

##### 4.1. The $\phi$ vector meson

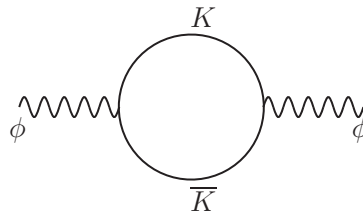


**Figure 3.**  $K\bar{K}$ -loop contribution to the  $\phi$  meson self-energy.

The  $\phi$  meson properties in nuclear matter, such as mass and decay width, are strongly correlated to its coupling to the  $K\bar{K}$ , which is the dominant decay channel in vacuum. Therefore, the density dependence of the  $\phi$  meson self-energy in nuclear matter arises mainly due to interactions of the kaons and antikaons with the nuclear medium, and the kaon and antikaon in-medium properties are calculated in the QMC model [85] (see also Fig. 1 for the effective mass of  $K(=\bar{K})$  meson). Here we use the effective Lagrangian approach of Ref. [98] to compute the  $\phi$  meson self-energy.

The lowest-order interaction Lagrangian providing the coupling of the  $\phi$  meson to the  $K\bar{K}$  pair reads [98]

$$\mathcal{L}_{\phi K\bar{K}} = ig_{\phi} \phi^{\mu} [\bar{K}(\partial_{\mu} K) - (\partial_{\mu} \bar{K}) K], \quad (10)$$

where  $g_\phi$  is  $\phi K\bar{K}$  coupling constant and we use the convention:

$$K = \begin{pmatrix} K^+ \\ K^0 \end{pmatrix}, \quad \bar{K} = \begin{pmatrix} K^- & \bar{K}^0 \end{pmatrix}. \quad (11)$$

The scalar self-energy for the  $\phi$  meson,  $\Pi_\phi(p)$ , is determined from Eq. (10). The Feynman diagram contributing to  $\Pi_\phi(p)$  at  $\mathcal{O}(g_\phi^2)$  is depicted in Fig. 3. For a  $\phi$  meson at rest the scalar self-energy is given by

$$i\Pi_\phi(m_\phi^2) = -\frac{8}{3}g_\phi^2 \int \frac{d^3q}{(2\pi)^3} \mathbf{q}^2 D_K(q) D_K(q-p), \quad (12)$$

where  $D_K(q) = (q^2 - m_K^2 + i\epsilon)^{-1}$  is the kaon propagator;  $p^\mu = (p^0 = m_\phi, \mathbf{0})$  is the  $\phi$  meson four-momentum vector ( $\phi$  at rest), with  $m_\phi$  the  $\phi$  meson mass;  $m_K (= m_{\bar{K}})$  is the kaon mass. When  $m_\phi < 2m_K$  the self-energy  $\Pi_\phi(p)$  is real. However, when  $m_\phi > 2m_K$ , which is the case here,  $\Pi_\phi(p)$  acquires an imaginary part.

The mass of the  $\phi$  meson is determined from the real part of  $\Pi_\phi(p)$  (see Eq. (17)), while its decay width  $\Gamma_\phi$  to a  $K\bar{K}$  pair from the imaginary part of  $\Pi_\phi(p)$  through the optical theorem (see Eq. (15)). The real and imaginary parts of  $\Pi_\phi(p)$  can be computed as [100]

$$\text{Re } \Pi_\phi = -\frac{2}{3}g_\phi^2 \mathcal{P} \int \frac{d^3q}{(2\pi)^3} \mathbf{q}^2 \frac{1}{E_K(E_K^2 - m_\phi^2/4)}, \quad (13)$$

$$\text{Im } \Pi_\phi = -\frac{g_\phi^2}{3\pi} \frac{1}{m_\phi} \left[ \frac{m_\phi}{2} \left( 1 - \frac{4m_K^2}{m_\phi^2} \right)^{1/2} \right]^3, \quad (14)$$

where  $\mathcal{P}$  denotes the Principal Value of the integral and  $E_K = (\mathbf{q}^2 + m_K^2)^{1/2}$ . The integral in Eq. (13) is divergent but it will be regulated using a phenomenological form factor, with cutoff parameter  $\Lambda_K$ , as in Ref. [37].

The decay width  $\Gamma_\phi$  for the process  $\phi \rightarrow K\bar{K}$  can be obtained from the imaginary part of the  $\phi$  meson self-energy  $\text{Im } \Pi_\phi$  through the optical theorem

$$\Gamma_\phi = -\frac{1}{m_\phi} \text{Im } \Pi_\phi, \quad (15)$$

where  $\text{Im } \Pi_\phi$  is given by Eq. (14). Thus, one gets

$$\Gamma_\phi = \frac{g_\phi^2}{3\pi} \frac{1}{m_\phi^2} \left[ \frac{m_\phi}{2} \left( 1 - \frac{4m_K^2}{m_\phi^2} \right)^{1/2} \right]^3. \quad (16)$$

The coupling constant  $g_\phi$  is determined by the experimental value for the  $\phi \rightarrow K\bar{K}$  decay width in vacuum, corresponding to a branching ratio of 83.1% of the total decay width (4.266 MeV) [93]. For the  $\phi$  meson mass  $m_\phi$  we use its experimental value in vacuum  $m_\phi^{\text{expt}} = 1019.461$  MeV [93]. For the kaon mass  $m_K$  there is a small ambiguity since  $m_{K^+} \neq m_{K^0}$  in the real world due to the isospin (or charge) symmetry breaking and electromagnetic interactions. The experimental values for the  $K^+$  and  $K^0$  meson masses in vacuum are  $m_{K^+}^{\text{expt}} = 493.677$  MeV and  $m_{K^0}^{\text{expt}} = 497.611$  MeV, respectively [93]. For definitiveness we use the average of  $m_{K^+}^{\text{expt}}$  and  $m_{K^0}^{\text{expt}}$  as the value of  $m_K$  in vacuum. (However, the effect of this tiny mass ambiguity on the properties of kaon (antikaon) in medium, to be presented in next section, is negligible compared with those obtained by using the value  $m_{K^+} = 493.7$  MeV [85].) This gives  $g_\phi = 4.539$  [100]. The mass of the  $\phi$  meson will be obtained from the solution of

$$m_\phi^2 = \left(m_\phi^0\right)^2 + \text{Re } \Pi_\phi(m_\phi^2) = \left(m_\phi^0\right)^2 - |\text{Re } \Pi_\phi(m_\phi^2)|, \quad (17)$$



where  $\text{Re } \Pi_\phi$  is given by Eq. (13) and  $m_\phi^0$  is the bare  $\phi$  meson mass. In vacuum, Eq. (17), together with the value obtained for the coupling constant, actually fixes the bare  $\phi$  meson mass  $m_\phi^0$ .

Critical to our results of the in-medium  $\phi$  meson mass  $m_\phi^*$  and decay width  $\Gamma_\phi^*$  at finite baryon density  $\rho_B$ , is the in-medium kaon mass  $m_K^*$ . The nuclear (baryon) density dependence of the  $\phi$  meson mass and decay width are driven by the interactions of the kaon with the nuclear medium, which enter through  $m_K^*$  in the kaon propagators in Eq. (12). The in-medium kaon mass  $m_K^*$  were calculated previously in the QMC model, and the results are shown in the right panel of Fig. 1. We note that the kaon effective mass at normal nuclear density  $\rho_0 = 0.15 \text{ fm}^{-3}$  decreases by about 13% [100]. We remind that, to calculate the kaon-antikaon loop contributions to the  $\phi$ -meson self-energy in symmetric nuclear matter, the isoscalar-vector  $\omega$  mean field potentials arise both for the kaon and antikaon. However, they have opposite signs and cancel each other, or can be eliminated by the variable shift in the loop integral calculation.

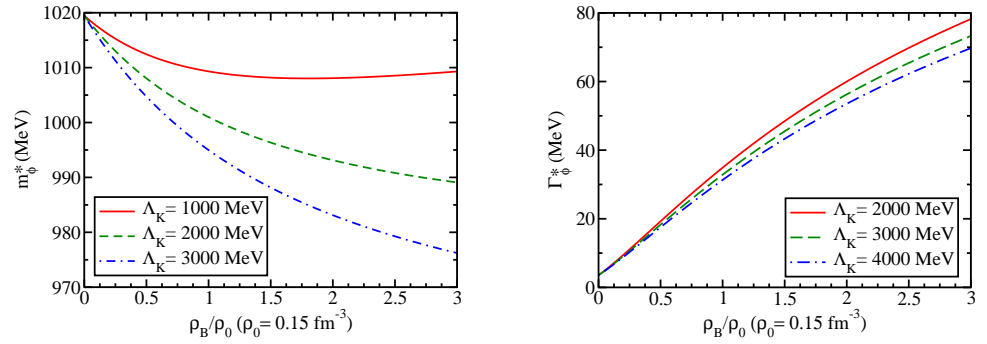


**Figure 4.** In-medium mass (left panel) and decay width (right panel) of the  $\phi$  meson in symmetric nuclear matter versus baryon density  $\rho_B/\rho_0$ .

To calculate the width and mass of the in-medium  $\phi$  meson,  $\Gamma_\phi^*$  and  $m_\phi^*$ , respectively, we solve the corresponding equations (16) and (17) in symmetric nuclear matter by replacing  $m_K$  by  $m_K^*$  and  $m_\phi$  by  $m_\phi^*$  in the self-energy of the  $\phi$  meson. In Fig. 4, we present our results [100] for the  $\phi$  meson mass (left panel) and decay width (right panel) in nuclear matter up to  $\rho_B = 3\rho_0$ . As can be seen in Fig. 4, the effect of the in-medium change in kaon mass gives a negative change in  $\phi$  meson mass. However, even for the largest value of density considered in this study, the downward mass shift is only a few percent for all values of the cutoff parameter  $\Lambda_K$ . In Table 1, we present the values for  $m_\phi^*$  and  $\Gamma_\phi^*$  at normal nuclear density  $\rho_0$ . More quantitatively, from Table 1 we see that the negative kaon mass shift of 13% induces only  $\approx 2\%$  downward mass shift of the  $\phi$  meson [100]. On the other hand, from Fig. (4) we see that  $\Gamma_\phi^*$  is very sensitive to the change in the kaon mass. It increases rapidly with increasing nuclear density, up to a factor of  $\sim 20$  enhancement for the largest nuclear density considered,  $\rho_B = 3\rho_0$  [100]. As can be seen from Table 1, the broadening of the  $\phi$  meson decay width becomes an order of magnitude larger than its vacuum value at normal nuclear density.

	$\Lambda_K = 1000$	$\Lambda_K = 2000$	$\Lambda_K = 3000$
$m_\phi^*$	1009.3	1000.9	994.9
$\Gamma_\phi^*$	37.7	34.8	32.8

**Table 1.**  $\phi$  meson mass and width at normal nuclear density,  $\rho_0$ . The  $\phi$  meson mass decreases by a few percent (1.8% in average), while the decay width increases by an order of magnitude, with respect to the corresponding vacuum values. All quantities are given in MeV.

#### 4.2. $\eta_c$ and $J/\psi$ mesons

The study of interactions of charmonium states, such as  $\eta_c$  and  $J/\psi$ , with atomic nuclei offers the opportunity to gain new insights into the properties of the strong force and strongly interacting matter [67]. Because charmonia and nucleons do not share light quarks the Okubo-Zweig-Iizuka (OZI) rule [94] suppresses the interactions mediated by the exchange of mesons composed of light quarks and/or antiquarks. The situation here is similar to the  $\phi$  meson case and also generally for quarkonia and two-heavy-flavor mesons). Thus, it is important and necessary to explore other possible mechanisms which can provide attractive (repulsive) interaction that could lead to the binding (unbinding) of charmonia to atomic nuclei [67]. For a review on the subject see Refs. [8–11]. Here we employ an effective Lagrangian approach and consider charmed meson loops in the charmonium self-energy [37,38,53,67,95], that light quark-antiquark pair is created from the vacuum.

Note that, recent lattice study using the HAL QCD method with nearly realistic pion mass of  $m_\pi = 146$  MeV, which was also able to reproduce well the physical hadron masses [96,97], found that the  $N$ - $c\bar{c}$  ( $N$ - $J/\psi$  and  $N$ - $\eta_c$ ) interactions to be attractive in all distances. They predicted mass reduction of  $J/\psi$ -meson at normal nuclear density of  $0.17 \text{ fm}^{-3}$  of about  $19(3)$  MeV. This is consistent with our prediction made by the without "gauge term" to be shown later.

For the computation of the  $\eta_c$  Lorentz scalar potential in nuclear matter, we use an effective Lagrangian approach at the hadronic level, which is an SU(4)-flavor extension of light-flavor chiral-symmetric Lagrangians of pseudoscalar and vector mesons [98,99]. When we treat the mesons contain at least one bottom quark (antiquark), we will use an SU(5)-flavor Lagrangian [31]. However one can expect that the SU(5) flavor symmetry breaking is larger than that of SU(4) due to the current quark mass values of the charm and bottom quarks. Thus for the SU(4) flavor sector, we use a flavor SU(4) effective Lagrangian, and determine the relevant coupling constants based the flavor SU(4) symmetry.

We compute the  $\eta_c$  self-energy in vacuum and symmetric nuclear matter, following our previous works [37,38,53,95,100–104], and consider only  $DD^*$  loop. See Ref. [67] for details. The interaction Lagrangian density for the  $\eta_c DD^*$  vertex is given by

$$\mathcal{L}_{\eta_c DD^*} = i g_{\eta_c DD^*} (\partial_\mu \eta_c) [\bar{D}^{*\mu} D - \bar{D} D^{*\mu}] - i g_{\eta_c DD^*} \eta_c [\bar{D}^{*\mu} (\partial_\mu D) - (\partial_\mu \bar{D}) D^{*\mu}], \quad (18)$$

where  $D^{(*)}$  represents the  $D^{(*)}$ -meson field isospin doublet, and  $g_{\eta_c DD^*}$  is the coupling constant. The  $\eta_c$  self-energy in the rest frame of  $\eta_c$  meson,  $p_{\eta_c}^\mu = (m_{\eta_c}, \mathbf{0})$  is given by [67]

$$\Sigma_{\eta_c}(m_{\eta_c}^2) = \frac{8g_{\eta_c DD^*}^2}{\pi^2} \int_0^\infty dq \, q^2 I(q^2), \quad (19)$$

where

$$I(q^2) = \frac{m_{\eta_c}^2 (-1 + q_0^2)/m_{D^*}^2}{(q_0 + \omega_{D^*})(q_0 - \omega_{D^*})(q_0 - m_{\eta_c} - \omega_D)} \Big|_{q_0=m_{\eta_c}-\omega_{D^*}} + \frac{m_{\eta_c}^2 (-1 + q_0^2)/m_{D^*}^2}{(q_0 - \omega_{D^*})(q_0 - m_{\eta_c} + \omega_D)(q_0 - m_{\eta_c} - \omega_D)} \Big|_{q_0=-\omega_{D^*}}, \quad (20)$$

and  $\omega_{D^{(*)}} = (q^2 + m_{D^{(*)}}^2)^{1/2}$ , with  $q = |\mathbf{q}|$ . The integral in Eq. (19) is divergent, and we regularize it with a phenomenological vertex form factor

$$u_{D^{(*)}}(q^2) = \left( \frac{\Lambda_{D^{(*)}}^2 + m_{\eta_c}^2}{\Lambda_{D^{(*)}}^2 + 4\omega_{D^{(*)}}^2(q^2)} \right)^2, \quad (21)$$



with cutoff parameter  $\Lambda_{D^{(*)}}$ , as in previous works. See Ref. [67] and references therein. Thus, to regularize Eq. (19) we will introduce the form factor  $u_D(k^2)u_{D^*}(k^2)$  into the integrand. As before, the cutoff parameter  $\Lambda_D^{(*)}$  is an unknown input to our calculation (we use  $\Lambda_{D^*} = \Lambda_D$ ). However, it may be fixed phenomenologically, for example, using a quark model. In Ref. [37] the value of  $\Lambda_D$  has been estimated to be  $\Lambda \approx 2500$  MeV, and serves as a reasonable guidance to quantify the sensitivity of our results to its value. Therefore we vary it over the interval 1500-3000 MeV [67].

Because the flavor  $SU(4)$  symmetry is strongly broken (though less than that of  $SU(5)$ ), we use the experimental values for the meson masses [93] and known (extracted) empirical values for the coupling constants, as explained in the following. For the  $D$  meson mass, we take the averaged masses of the neutral and charged states, and similarly for the  $D^*$ . Thus  $m_D = 1867.2$  MeV and  $m_{D^*} = 2008.6$  MeV. For the coupling constants,  $g_{\eta_c DD^*} = 0.60 g_{\psi DD}$  was obtained in Ref. [105], as the residue at the poles of suitable form factors using a dispersion formulation of the relativistic constituent quark model, where  $g_{\psi DD} = 7.64$  was estimated in Ref. [106] using the vector meson dominance (VMD) model and isospin symmetry. In this study we use the coupling constant,  $g_{\eta_c DD^*} = (0.60/\sqrt{2}) g_{\psi DD} \simeq 0.424 g_{\psi DD}$  [67], where the factor  $(1/\sqrt{2})$  is introduced to give a larger  $SU(4)$  symmetry breaking effect than Ref. [105].

In this subsection, we will show the mass shift of  $\eta_c$  with the use of both the  $SU(4)$  symmetry coupling constant as well as that with the broken  $SU(4)$  coupling constant. Furthermore, later we will compare the in-medium masses of  $\eta_c$  and  $J/\psi$  with those of the  $\eta_b, Y, B_c$  and  $B_c^*$ , using the coupling constant value  $g_{\eta_c DD^*} = g_{\psi DD} = 7.64 \rightarrow 7.7$ , without any symmetry breaking factor, i.e.,  $g_{\eta_c DD^*} = (0.60/\sqrt{2}) g_{\psi DD} \simeq 0.424 g_{\psi DD} \rightarrow g_{\eta_c DD} = g_{\psi DD} = 7.7$ , where the tiny difference may be ignored. For the  $J/\psi$  mass shift in this subsection, after  $\eta_c$  mass shift, we will use only the  $SU(4)$  symmetric coupling constant,  $g_{\psi DD} = 7.64$ .

We are interested in the difference between the in-medium,  $m_{\eta_c}^*$ , and vacuum,  $m_{\eta_c}$ , masses of the  $\eta_c$ ,

$$\Delta m_{\eta_c} = m_{\eta_c}^* - m_{\eta_c}, \quad (22)$$

with the masses obtained self-consistently from

$$m_{\eta_c}^2 = (m_{\eta_c}^0)^2 + \Sigma_{\eta_c}(m_{\eta_c}^2) = (m_{\eta_c}^0)^2 - |\Sigma_{\eta_c}(m_{\eta_c}^2)|, \quad (23)$$

where  $m_{\eta_c}^0$  is the bare  $\eta_c$  mass and the  $\eta_c$  self-energy in the rest frame of  $\eta_c$  meson,  $\Sigma_{\eta_c}(m_{\eta_c}^2)$  is given by Eq. (19). The  $\Lambda_D$ -dependent  $\eta_c$ -meson bare mass,  $m_{\eta_c}^0$ , is fixed by fitting the physical  $\eta_c$ -meson mass,  $m_{\eta_c} = 2983.9$  MeV [67].

The in-medium  $\eta_c$  mass is obtained in a similar way, with the self-energy calculated with the medium-modified  $D$  and  $D^*$  meson masses. The nuclear density dependence of the  $\eta_c$ -meson mass is influenced and determined by the intermediate-state  $D$  and  $D^*$  meson interactions with the nuclear medium through their medium-modified masses. The in-medium masses  $m_D^*$  and  $m_{D^*}$  are calculated within the quark-meson coupling (QMC) model [37,38], in which effective scalar and vector meson mean fields couple to the light  $u$  and  $d$  quarks in the charmed mesons [37,38].

In the middle panel of Fig. 1 we present the resulting medium-modified masses for the  $D$  and  $D^*$  mesons, calculated within the QMC model [37], as a function of  $\rho_B/\rho_0$ , where  $\rho_B$  is the baryon density of nuclear matter and  $\rho_0 = 0.15 \text{ fm}^{-3}$  the saturation density of symmetric nuclear matter. The net reductions in the masses of the  $D$  and  $D^*$  mesons are nearly the same as a function of density, with each decreasing by about 60 MeV at  $\rho_0$ . The behavior of the  $D$  meson mass in medium (finite density and/or temperature) has been studied in a variety of approaches, where some of these [107–109] find a decreasing  $D$  meson mass at finite baryon density, while others [110–114], interestingly, find the opposite behavior. However, it is important to note that none of the studies in nuclear matter are constrained by the saturation properties of nuclear matter, despite they are constrained in

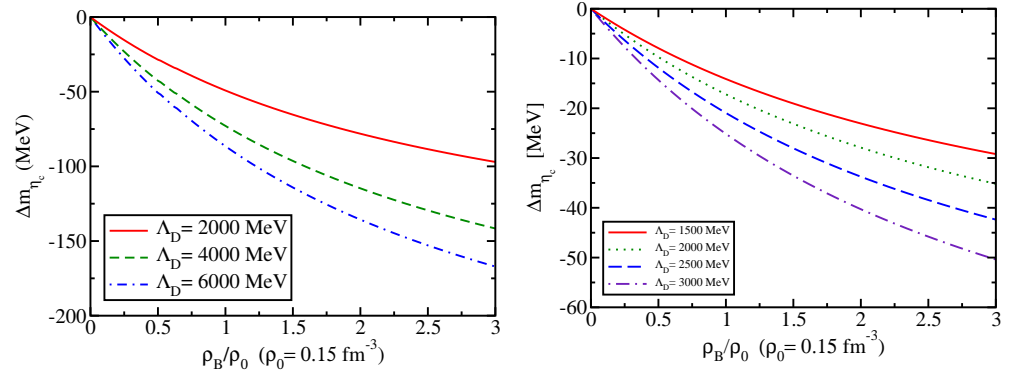


**Figure 5.**  $\eta_c$  mass shift (i) with the SU(4) symmetric coupling [84],  $g_{\eta_c DD} = 7.64$  (left-panel), and (ii) with the broken SU(4) symmetry coupling [67]  $(0.6/\sqrt{2}) \times (g_{\eta_c DD^*} = 7.64)$  (right panel), versus nuclear matter density for various values of the cutoff parameter.

the present work. Furthermore, some of these works employ a non relativistic approach, where relativistic effects might be important.

In Fig. 5, we present the  $\eta_c$ -meson mass shift,  $\Delta m_{\eta_c}$ , as a function of the nuclear matter density,  $\rho_B$  ( $\rho_B/\rho_0$ ), for four values of the cutoff parameter  $\Lambda_D$  [67]. As can be seen from the figure, the effect of the in-medium  $D$  and  $D^*$  mass changes is to shift the  $\eta_c$  mass downwards. This is because the reduction in the  $D$  and  $D^*$  masses enhances the  $DD^*$ -loop contribution in nuclear matter relative to that in vacuum. This effect increases the larger the cutoff mass  $\Lambda_D$  becomes.

The results described above with the two values of the  $g_{\eta_c DD^*}$  coupling constants, both support a small downward mass shift for the  $\eta_c$  in nuclear matter, and open the possibility to study the binding of  $\eta_c$  meson to nuclei [67].

We now turn to the discussion of the  $J/\psi$  vector meson [124,125], following the same procedure as in the  $\phi$  meson. In Refs. [11,37,38], the  $J/\psi$  self-energy intermediate states involved the  $D$ ,  $\bar{D}$ ,  $D^*$ , and  $\bar{D}^*$  mesons. However, it was found that the  $J/\psi$  self-energy has larger contributions from the loops involving the  $D^*$  and  $\bar{D}^*$  mesons, which is unexpected; see Ref. [11,37,38] for details on the issues and possible explanations. As explained in Ref. [11], this is related to the divergent behavior of the vector meson propagator. We present results for the  $J/\psi$  mass shift in nuclear matter and nuclei considering only the lightest intermediate state mesons in the  $J/\psi$  self-energy, namely the  $D\bar{D}$  loop [124,125].

We use the following phenomenological effective Lagrangian densities at the hadronic level, which are similar to those used above for the  $\phi$ -meson,

$$\mathcal{L}_{int} = \mathcal{L}_{\psi DD} + \mathcal{L}_{\psi\psi DD}, \quad (24)$$

$$\mathcal{L}_{\psi DD} = ig_{\psi DD} \psi^\mu [\bar{D}(\partial_\mu D) - (\partial_\mu \bar{D})D], \quad (25)$$

$$\mathcal{L}_{\psi\psi DD} = g_{\psi DD}^2 \psi_\mu \psi^\mu \bar{D}D. \quad (26)$$

where  $g_{\psi DD}$  is the  $J/\psi$   $D\bar{D}$  coupling constant and we use the convention

$$D = \begin{pmatrix} D^0 \\ D^+ \end{pmatrix}, \quad \bar{D} = (\bar{D}^0 \quad \bar{D}^-). \quad (27)$$

For notational simplicity we have written  $\psi$  the field representing the  $J/\psi$  vector meson. We note that the Lagrangians are an  $SU(4)$  extension of light-flavor chiral-symmetric Lagrangians of pseudoscalar and vector mesons. In the light flavor sector, they have been motivated by a local gauge symmetry, treating vector mesons either as massive gauge bosons or as dynamically generated gauge bosons. Local gauge symmetry implies in the contact interaction in Eq. (26) involving two pseudoscalar and two vector mesons.

In view of the fact that  $SU(4)$  flavor symmetry is strongly broken in nature, and in order to stay as close as possible to phenomenology, we use experimental values for the charmed meson masses and use the empirically known meson coupling constants. For these reasons we do not use gauged Lagrangians for the study of  $J/\psi$  nuclear bound states – a similar attitude was followed in Ref. [99] in a study of hadronic scattering of charmed mesons. However, in order to compare results with Ref. [52] and assess the impact of a contact term of the form Eq. (26), we also present results for the  $J/\psi$  mass shift including such a term.

We are interested in the difference of the in-medium,  $m_\psi^*$ , and vacuum,  $m_\psi$ ,

$$\Delta m_\psi = m_\psi^* - m_\psi, \quad (28)$$

with the masses obtained from

$$m_\psi^2 = (m_\psi^0)^2 + \Sigma_{D\bar{D}}(m_\psi^2) = (m_\psi^0)^2 - |\Sigma_{D\bar{D}}(m_\psi^2)|. \quad (29)$$

Here  $m_\psi^0$  is the bare mass and  $\Sigma_{D\bar{D}}(k^2)$  is the total  $J/\psi$  self-energy obtained from the  $D\bar{D}$ -loop contribution only. The in-medium mass,  $m_\psi^*$ , is obtained likewise, with the self-energy calculated with medium-modified  $D$  meson mass calculated by the QMC model (see again the middle panel of Fig. 1).

The scalar self-energy for the  $J/\psi$  meson in the rest frame of  $J/\psi$ ,  $\Sigma_{D\bar{D}}(m_\psi^2)$ , is obtained from Eq. (25). The Feynman diagram contributing to  $J/\psi$  self-energy  $\mathcal{O}(g_\psi^2)$  is identical to the one in Fig. 3 with the replacements  $\phi \rightarrow J/\psi$ ,  $K \rightarrow D$  and  $\bar{K} \rightarrow \bar{D}$ .

For a  $J/\psi$  meson at rest, the self-energy is given by

$$\Sigma_{D\bar{D}}(m_\psi^2) = -\frac{g_{\psi DD}^2}{3\pi^2} \int_0^\infty dq q^2 F_{D\bar{D}}(q^2) K_{D\bar{D}}(q^2), \quad (30)$$

where  $q = |\mathbf{q}|$ , and  $F_{D\bar{D}}(q^2) = u_D(q^2)u_{\bar{D}}(q^2)$  is the product of vertex form-factors with  $u_D(q^2)$  and  $u_{\bar{D}}$  given as in Eq. (21) with cutoff parameters  $\Lambda_D$  and  $\Lambda_{\bar{D}}$ , respectively (we use  $\Lambda_D = \Lambda_{\bar{D}}$ ); and  $K_{D\bar{D}}(q^2)$  for the  $D\bar{D}$  loop contribution is given by

$$K_{D\bar{D}}(q^2) = \frac{q^2}{\omega_D} \left( \frac{q^2}{\omega_D^2 - m_\psi^2/4} - \xi \right), \quad (31)$$

where  $\omega_D = (q^2 + m_D^2)^{1/2}$ ,  $\xi = 0$  for the non-gauged Lagrangian of Eq. (25) and  $\xi = 1$  with Eq. (26), for the gauged Lagrangian of Ref. [52].

As before, the cutoff parameter  $\Lambda_D$  is an unknown input to our calculation. However, it may be fixed phenomenologically. In Ref. [37] the value of  $\Lambda_D$  has been estimated to be  $\Lambda_D \approx 2500$  MeV, and serves as a reasonable guidance to quantify the sensitivity of our results to its value. Since this is a somewhat rough estimate, and it is made solely to obtain an order of magnitude estimate, we allow the value of  $\Lambda_D$  vary in the range  $2000 \text{ MeV} \leq \Lambda_D \leq 6000 \text{ MeV}$ ; see Ref. [11,37,38].

There remain to be fixed the bare  $J/\psi$  mass  $m_\psi^0$  and the coupling constants. The bare mass is fixed by fitting the physical mass  $m_{J/\psi} = 3096.9$  MeV using Eq. (29). As before, because the flavor symmetry  $SU(4)$  is strongly broken we use experimental values for the meson masses and known empirical values for the coupling constants. For the  $D$  meson mass, we take the averaged masses of the neutral and charged  $D$  mesons. Thus  $m_D = 1867.2$  MeV [93]. For the coupling constants we use  $g_{\psi DD} = 7.64$ , which is obtained by the use of isospin symmetry [106]. Note that, for  $J/\psi$  we use only the  $SU(4)$  coupling constant extracted, different from that of the  $\eta_c$  case (no extra  $SU(4)$  breaking effect on the coupling constant).

The nuclear density dependence of the  $J/\psi$ -meson mass is influenced and determined by the intermediate-state  $D$  and  $\bar{D}$  meson interactions with the nuclear medium through

their medium-modified masses. The in-medium masses  $m_D^*$  and  $m_{\bar{D}}^* = m_{D^*}^*$  are calculated within the quark-meson coupling (QMC) model [37,38], in which effective scalar and vector meson mean fields couple to the light  $u$  and  $\bar{d}$  quarks in the charmed mesons [37,38]. However in the self-energy of  $D\bar{D}$  loop, the vector potentials cancel out, and no need of considering the effects.

See again the middle panel of Fig. 1 we present the medium-modified masses for the  $D$  and  $\bar{D}$  mesons ( $m_{\bar{D}}^* = m_D^*$ ), calculated within the QMC model [37], as a function of  $\rho_B/\rho_0$ . In Fig. 6 we show the contribution of the  $D\bar{D}$ -loop to the  $J/\psi$  mass shift for  $\xi = 0$ . As the cutoff mass value increases in the form factor, obviously the  $D\bar{D}$ -loop contribution becomes larger.

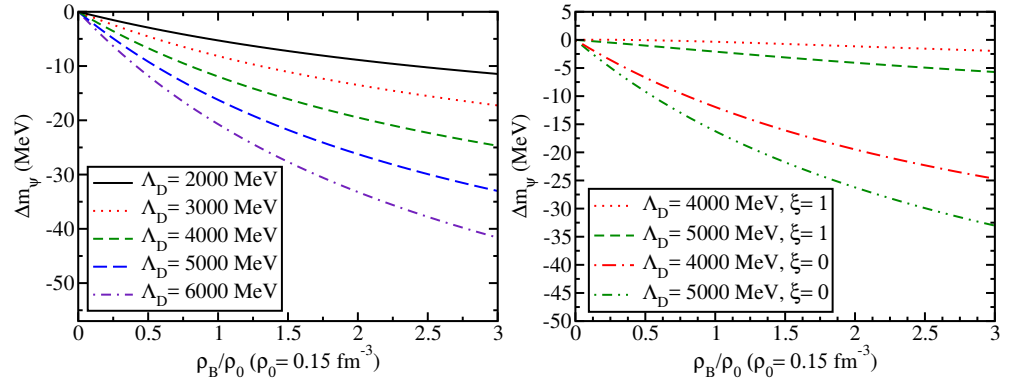


**Figure 6.** Contribution from the  $D\bar{D}$ -loop to the  $J/\psi$  mass shift in symmetric nuclear matter without the gauge term ( $\xi = 0$ ) for five different values of the cutoff  $\Lambda_D$  (left panel), and the comparison with including the gauge term ( $\xi = 1$ ) for two values of  $\Lambda_D$  (right panel).

First, from the result shown in the left panel of Fig. 6 without the gauge term ( $\xi = 0$ ), one can see that the  $J/\psi$  gets the attractive potential for all the values of the cutoff  $\Lambda_D$ , 2000 – 6000 MeV [124,125]. In contrast, one can see from the right panel in Fig. 6, that the effect of the gauge term tends to oppose the effect (repulsion) of the contribution of the  $D\bar{D}$ -loop as noticed in Ref. [37] [124,125]. When the value of  $\Lambda_D$  is smaller, the mass shift actually becomes positive. The results shown in Fig. 6 reveal a negative mass shift (attractive potential) for the  $J/\psi$  meson in symmetric nuclear matter for all values of the cutoff mass parameter  $\Lambda_D$  when  $\xi = 0$  and, as in the  $\eta_c$  meson case, open the possibility to study the binding of  $J/\psi$  mesons to nuclei [124,125].

#### 4.3. $Y$ and $\eta_b$ mesons

First, we discuss the  $Y$  (vector) meson. The  $Y$  mass shift in nuclear matter originates from the modifications of the  $BB$ ,  $BB^*$ , and  $B^*B^*$  meson loops contributions to the  $Y$  self-energy, relative to those in free space; the lowest order Feynman diagrams associated with these contributions are similar to Fig. 3. The  $Y$  self-energy is calculated using an effective SU(5)-flavor symmetric Lagrangian at the hadronic level [31,72], where mesons are considered to be point like, for the interaction vertices  $YBB$ ,  $YB^*B^*$ , and  $YBB^*$  neglecting any possible imaginary part. In Ref. [72] we made an extensive analysis of these contributions to the  $Y$  self-energy and found that, for example, the  $B^*B^*$  loop gives an unexpectedly large contribution, similar to the case of  $J/\psi$ . For this reason, and to be consistent with the  $\eta_b$  case studied below, we consider only the  $BB$  loop contribution to the  $Y$  self-energy [72], leaving for the future a full study of all three contributions. This treatment is also consistent with the  $J/\psi$  self-energy calculation with the lowest  $D\bar{D}$  loop contribution, and we can compare the amounts of mass shift for the  $Y$  and  $J/\psi$  based on a similar footing. The interaction Lagrangian for the  $YBB$  vertex is given by [72]

$$\mathcal{L}_{YBB} = ig_{YBB} Y^\mu [\bar{B} \partial_\mu B - (\partial_\mu \bar{B}) B], \quad (32)$$

where  $g_{YBB}$  is the coupling constant for the vertex  $YBB$  vertex, and the following convention is adopted for the isospin doublets of the  $B$  mesons

$$B = \begin{pmatrix} B^+ \\ B^0 \end{pmatrix}, \quad \bar{B} = \begin{pmatrix} B^- & \bar{B}^0 \end{pmatrix}.$$

The coupling constant  $g_{YBB}$  is calculated from the experimental data for  $\Gamma(Y \rightarrow e^+e^-)$  using the vector meson dominance (VMD) model. This gives  $g_{YBB} = 13.2$ ; see Refs. [31,72] and references therein for details. We note that a similar approach was taken in Refs. [37,106] to determine the coupling constant  $g_{J/\psi DD} = 7.64$  for the vertex  $J/\psi DD$ .

Including only the  $BB$  loop, Eq. (32), the  $Y$  self-energy  $\Sigma_Y$  for an  $Y$  at rest is given by [72]

$$\Sigma_Y(m_Y^2) = -\frac{g_{YBB}^2}{3\pi^2} \int_0^\infty dq q^2 I(q^2) \quad (33)$$

where

$$I(q^2) = \frac{1}{\omega_B} \left( \frac{q^2}{\omega_B - m_Y^2/4} \right), \quad (34)$$

with  $q = |\mathbf{q}|$  and  $\omega_B = (q^2 + m_B^2)^{1/2}$ . As is always the case in an effective Lagrangian approach, when mesons are treated as point-like particle, the self-energy loop integrals like Eq. (33) are divergent and therefore need to be regularized. To this end, we introduce into the integrand of Eq. (33) a phenomenological vertex form factor  $u_B(q^2)$  with cutoff parameter  $\Lambda_B$  [37,38,53,95,100–104], for to each  $YBB$  vertex, as we did in previous cases; see Eq. (21). We recall that form factors are necessary to take into account the finite size of the mesons participating in the vertices, while the cutoff  $\Lambda_B$ , which is an unknown input to our calculation, may be associated with energies needed to probe the internal structure of the mesons. Thus, in order to reasonably include these effects, and to quantify the sensitivity of our results to its value, we vary  $\Lambda_B$  over the interval 2000–6000 MeV (roughly up to around the mass of the  $B$  meson); see Ref. [72] for a more extensive discussion.

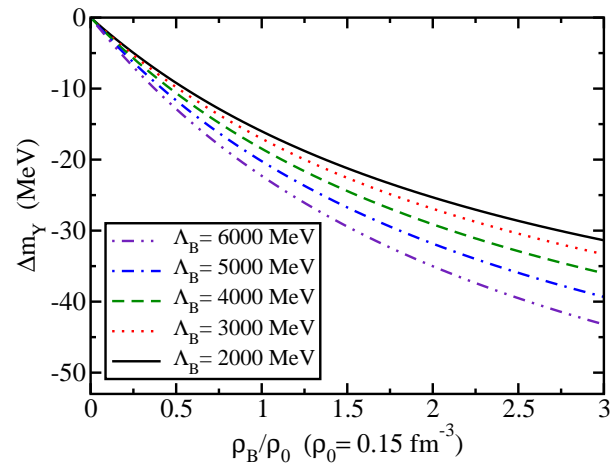


**Figure 7.**  $Y$  mass shift in symmetric nuclear matter as a function of the nuclear matter density ( $\rho_B/\rho_0$ )

The  $Y$  mass shift in nuclear matter,  $\Delta m_Y$ , is calculated from the difference between its mass in the medium,  $m_Y^*$ , and its value in vacuum,  $m_Y$ , in the rest frame of the  $Y$ , namely,

$$\Delta m_Y = m_Y^* - m_Y, \quad (35)$$

where these masses are computed self-consistently from

$$m_Y^2 = (m_Y^0)^2 + \Sigma_Y(m_Y^2) = (m_Y^0)^2 - |\Sigma_Y(m_Y^2)|, \quad (36)$$

with  $m_Y^0$  the bare Y mass and the Y self-energy  $\Sigma_Y(m_Y^2)$  is given in Eq. (33). The  $\Lambda_B$ -dependent Y bare mass,  $m_Y^0$ , is fixed with the physical Y mass, namely  $m_Y = 9640$  MeV.

The in-medium Y mass  $m_Y^*$  is obtained by solving Eq. (36) with the self-energy calculated with medium-modified B mass. This medium-modified mass was calculated using the quark-meson coupling (QMC) model as a function of the nuclear matter density  $\rho_B$ , and the results are shown in Fig. 1 (left panel). From Fig. 1, it can be seen that the QMC model gives a similar downward mass shift for the B and  $B^*$  in symmetric nuclear matter. For example, at the saturation density  $\rho_0 = 0.15 \text{ fm}^{-3}$ , the mass shift for the B and  $B^*$  mesons are respectively,  $(m_B^* - m_B) = -61$  MeV and  $(m_{B^*}^* - m_{B^*}) = -61$  MeV, where the difference in their mass shift values appears in the decimal place. The values for the masses in vacuum for the B and  $B^*$  mesons used are  $m_B = 5279$  MeV and  $m_{B^*} = 5325$  MeV, respectively.

The nuclear density dependence of the Y mass is driven by the intermediate  $B\bar{B}$  state interactions with the nuclear medium, where the effective scalar and vector meson mean fields couple to the light  $u$  and  $d$  quarks in the bottom mesons, B and  $B^*$ . In Fig. 7 we show the results for the Y mass shift as a function of the nuclear density,  $\rho_B/\rho_0$ , for five values of the cutoff parameter  $\Lambda_B$ . As can be seen in Figs. 1 (left panel) and 7, a decreasing of the in-medium B meson mass induces a negative mass shift for Y. As expected, the mass shift amount of the Y is dependent on the value of the cutoff mass  $\Lambda_B$  used, being larger for larger  $\Lambda_B$ ; see Ref. [72] for further details. For example, for the values of the cutoff shown in Fig. 7, the Y mass shift amount varies from -16 to -22 MeV, at  $\rho_B = \rho_0$ .

For the calculation of the  $\eta_b$  mass shift in nuclear matter, we proceed similarly to the Y case and take into account only the  $BB^*$  loop (pseudoscalar-pseudoscalar-vector) contribution to the  $\eta_b$  self-energy. In Ref. [72] we have also studied the mass shift including the  $\eta_b B^* B^*$  interaction in the  $\eta_b$  self-energy, and found that its contribution to the mass shift amount turned out to be negligible. Thus, in order to be consistent with the Y case above, in both cases we consider only the minimal contribution, and here we only give results for the  $BB^*$  loop in the  $\eta_b$  self-energy. This is also a consistent treatment with the  $\eta_c$  mass shift calculation, and later we can compare based on a similar footing of the self-energy calculation.

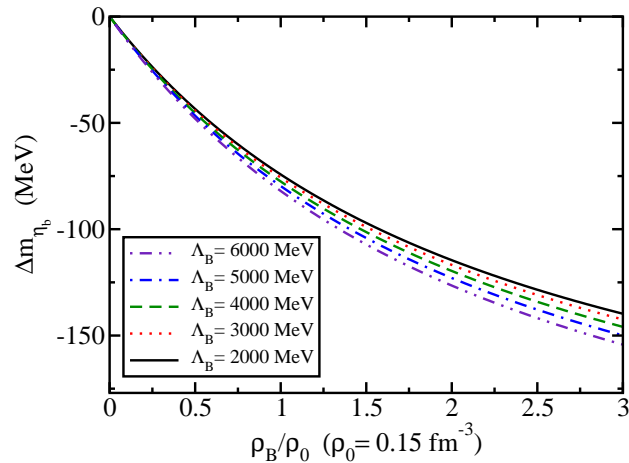


**Figure 8.**  $\eta_b$  mass shift in nuclear matter as a function of the nuclear density  $\rho_B/\rho_0$ .



For the calculation of the  $\eta_b$  mass shift in symmetric nuclear matter, we proceed similarly to the  $Y$  and  $\eta_c$  cases, and take into account only the  $BB^*$  loop contribution to the  $\eta_b$  self-energy. As already mentioned, in Ref. [72], we have also studied including the  $\eta_b B^* B^*$  interaction in the  $\eta_b$  self-energy and found that its contribution to the mass shift amount is negligible.

The effective Lagrangian for the  $\eta_b BB^*$  interaction is [72]

$$\mathcal{L}_{\eta_b BB^*} = ig_{\eta_b BB^*} \left[ (\partial^\mu \eta_b) (\bar{B}_\mu^* B - \bar{B} B_\mu^*) - \eta_b (\bar{B}_\mu^* (\partial^\mu B) - (\partial^\mu \bar{B}) B_\mu^*) \right], \quad (37)$$

where  $g_{\eta_b BB^*}$  is the coupling constant for the  $\eta_b BB^*$  vertex. We will use its value in the SU(5) scheme [72], namely  $g_{\eta_b BB^*} = g_{YBB} = g_{YB^*B^*} = \frac{5g}{4\sqrt{10}}$ . Using Eq. (37), the  $\eta_b$  self-energy for an  $\eta_b$  at rest is given by [67]

$$\Sigma_{\eta_b} = \frac{8g_{\eta_b BB^*}^2}{\pi^2} \int_0^\infty dq q^2 I(q^2), \quad (38)$$

where

$$\begin{aligned} I(q^2) &= \frac{m_{\eta_b}^2 (-1 + q_0^2/m_{B^*}^2)}{(q_0^2 - \omega_{B^*}^2)(q_0 - m_{\eta_b} - \omega_B)} \Big|_{q_0=m_{\eta_b}-\omega_B} \\ &+ \frac{m_{\eta_b}^2 (-1 + q_0^2/m_{B^*}^2)}{(q_0 - \omega_{B^*})((q_0 - m_{\eta_b})^2 - \omega_B^2)} \Big|_{q_0=-\omega_{B^*}}, \end{aligned} \quad (39)$$

with  $q = |\mathbf{q}|$  and  $\omega_{B^*} = \sqrt{q^2 + m_{B^*}^2}$ . The mass of the  $\eta_b$  meson, in vacuum and in nuclear matter, is computed similarly to the  $Y$  case [72]. First, we introduce form factors, as in Eq. (21), into each  $\eta_b BB^*$  vertex, with  $\Lambda_B = \Lambda_{B^*}$ , to regularize the divergent integral in the self-energy Eq. (38). Second, we fix the value of the  $\eta_b$  bare mass using the physical (vacuum) mass of the  $\eta_b$ , namely  $m_{\eta_b} = 9399$  MeV, using Eq. (36) appropriately written for the  $\eta_b$  case. Then, for the calculation of the  $\eta_b$  mass shift in nuclear matter, the self-energy  $\Sigma_{\eta_b}$  is computed using the medium-modified  $B$  and  $B^*$  masses calculated with the QMC model and shown in Fig. 1 (left panel). The results for the  $\eta_b$  mass shift behavior in nuclear matter are shown in Fig. 8 as a function of the nuclear matter density  $\rho_B/\rho_0$ , for the same range of values for the cutoff mass  $\Lambda_B$  as for the  $Y$  [72]. As can be seen from Fig. 8, the mass of the  $\eta_b$  is shifted downwards in nuclear matter for all values of the cutoff  $\Lambda_B$ , similarly to the  $Y$ . For example, at the normal density of symmetric nuclear matter  $\rho_0$ , the mass shift value varies from -75 MeV to -82 MeV when the cutoff varies from  $\Lambda_B = 2000$  MeV to  $\Lambda_B = 6000$  MeV. Similarly to the  $Y$  mass shift, the dependence of the  $\eta_b$  mass shift amount on the values of the cutoff is small, for example, just -7 MeV when the cutoff is increased by a factor of 3 at  $\rho_B = \rho_0$  [72].

#### 4.4. $B_c$ and $B_c^*$ mesons

The  $B_c$  ( $B_c^*$ ) in-medium downwards mass shift comes from the enhanced  $B^*D + BD^*$  ( $BD$ ) loop contribution to the self-energy, relative to those in free space. See Fig. 3 but replacing the  $K\bar{K}$  loop properly by  $B^*D$  and  $BD^*$  loops ( $BD$  loop). See Refs. [84] for details. By expanding the SU(5) flavor symmetric effective meson Lagrangian [31] in terms of the components of pseudoscalar ( $P$ ) and vector ( $V$ )  $5 \times 5$  matrices, we obtain the following Lagrangians for the interactions  $B_c B^* D$ ,  $B_c B D^*$  and  $B_c^* B D$  [84]:

$$\begin{aligned} \mathcal{L}_{B_c B^* D} &= ig_{B_c B^* D} [(\partial_\mu B_c^-) D - B_c^- (\partial_\mu D)] B^{*\mu} + h.c., \\ \mathcal{L}_{B_c B D^*} &= ig_{B_c B D^*} [(\partial_\mu B_c^+) \bar{B} - B_c^+ (\partial_\mu \bar{B})] \bar{D}^{*\mu} + h.c., \\ \mathcal{L}_{B_c^* B D} &= -ig_{B_c^* B D} B_c^{*+\mu} [\bar{B} (\partial_\mu \bar{D}) - (\partial_\mu \bar{B}) \bar{D}] + h.c., \end{aligned} \quad (40)$$

where the conventions for the  $B, D$  and  $B^*$  mesons have been already given.

The SU(5) symmetric universal coupling  $g$  yields the relations,  $g_{B_c B^* D} = g_{B_c B D^*} = g_{B_c^* B D}$ . The value of  $g$  is fixed by  $g_{YBB} = \frac{5g}{4\sqrt{10}} \approx 13.2$  by the  $Y$  decay data  $\Gamma(Y \rightarrow e^+ e^-)$  with the vector meson dominance (VMD) model [31,72], and thus we get,

$$g_{B_c B^* D} = \frac{2}{\sqrt{5}} g_{YBB}, \quad g_{B_c B^* D} = g_{B_c B D^*} = g_{B_c^* B D} = \frac{g}{2\sqrt{2}} \approx 11.9. \quad (41)$$

The in-medium mass shift of the  $B_c$  meson,  $\Delta m_{B_c}$ , is computed by the difference of the in-medium  $m_{B_c}^*$  and the free space  $m_{B_c}$  masses

$$\Delta m_{B_c} = m_{B_c}^* - m_{B_c}, \quad (42)$$

where, the free space mass  $m_{B_c}$  (input) is used to determine the bare mass  $m_{B_c}^0$  by

$$m_{B_c}^2 = \left(m_{B_c}^0\right)^2 + \Sigma_{B_c}(m_{B_c}^2) = \left(m_{B_c}^0\right)^2 - |\Sigma_{B_c}(m_{B_c}^2)|. \quad (43)$$

Note that, the total self-energy  $\Sigma_{B_c}$  is calculated by the sum of the  $B^* D$  and  $BD^*$  meson loop contributions in free space ignoring the possible  $B_c$  meson as well as all the other meson widths (or imaginary part) in the self-energy. The in-medium  $B_c$  mass  $m_{B_c}^{*2}$  is similarly calculated, with the same bare mass value  $m_{B_c}^0$  determined in free space, and the in-medium masses of the  $(B, B^*, D, D^*)$  mesons  $(m_B^*, m_{B^*}^*, m_D^*, m_{D^*}^*)$ , namely,

$$m_{B_c}^2 = \left[m_{B_c}^0(B^* D + BD^*)\right]^2 - |\Sigma_{B_c}(B^* D) + \Sigma_{B_c}(BD^*)|(m_{B_c}^2), \quad (44)$$

$$m_{B_c}^{*2} = \left[m_{B_c}^0(B^* D + BD^*)\right]^2 - |\Sigma_{B_c}^*(B^* D) + \Sigma_{B_c}^*(BD^*)|(m_{B_c}^{*2}). \quad (45)$$

We note that, when the self-energy graphs contain different contributions, as  $\Sigma_{B_c}(\text{total}) = \Sigma(B^* D) + \Sigma(BD^*)$ ,  $m^0$  depends on both  $\Sigma(B^* D)$  and  $\Sigma(BD^*)$  to reproduce the physical mass  $m_{B_c}$ . Thus, one must be careful when discussing the  $B_c$  in-medium mass and mass shift of each loop contribution  $\Sigma(B^* D)$  and  $\Sigma(BD^*)$ , since  $m^0(B^* D + BD^*) \neq m^0(B^* D) \neq m^0(BD^*)$ , and  $m^0(B^* D + BD^*) \neq m^0(B^* D) + m^0(BD^*)$ . The dominant loop contribution can be known by the decomposition of the self-energy  $\Sigma_{B_c}^{(*)}(B^* D + BD^*) = \Sigma_{B_c}^{(*)}(B^* D) + \Sigma_{B_c}^{(*)}(BD^*)$ . It turned out that the dominant contribution is from the  $BD^*$  loop [84]. This is due to the dominant contribution from the lighter vector meson  $D^*$  due to the vector meson propagator Lorentz structure.

As an example, in the case considering solely the  $B^* D$  loop without the  $BD^*$  loop, the "in-medium"  $B_c$  self-energy in the rest frame of  $B_c$  is given by

$$\Sigma_{B_c}^{B^* D}(m_{B_c}^*) = \frac{-4g_{B_c B^* D}^2}{\pi^2} \int dq q^2 I_{B_c}^{B^* D}(q^2) F_{B_c B^* D}(q^2), \quad (46)$$

with  $q = |\mathbf{q}|$ , and  $I_{B_c}^{B^* D}(q^2)$  is expressed, after the Cauchy integral with respect to  $q^0$  complex plane shifting  $q^0$  variable for the vector potentials as,

$$I_{B_c}^{B^* D}(q^2) = \frac{m_{B_c}^{*2}(-1 + q_0^2/m_{B^*}^{*2})}{(q_0 - \omega_{B^*}^*)(k_0 - m_{B_c}^* + \omega_D^*)(q_0 - m_{B_c}^* - \omega_D^*)} \Big|_{q_0 = -\omega_{B^*}^*} + \frac{m_{B_c}^{*2}(-1 + q_0^2/m_{B^*}^{*2})}{(q_0 + \omega_{B^*}^*)(q_0 - \omega_{B^*}^*)(q_0 - m_{B_c}^* - \omega_D^*)} \Big|_{q_0 = m_{B_c}^* - \omega_D^*}, \quad (47)$$

where,  $F_{B_c B^* D}$  in Eq. (46) is the product of vertex form factors in medium to regularize the divergence in the loop integral,  $F_{B_c B^* D}(q^2) = u_{B_c B^*}(q^2) u_{B_c D}(q^2)$ . They are given by

using the corresponding meson in-medium masses,  $u_{B_c B^*} = \left( \frac{\Lambda_{B^*}^2 + m_{B_c}^{*2}}{\Lambda_{B^*}^2 + 4\omega_{B^*}^2(q^2)} \right)^2$  and  $u_{B_c D} = \left( \frac{\Lambda_D^2 + m_{B_c}^{*2}}{\Lambda_D^2 + 4\omega_D^2(q^2)} \right)^2$  with  $\Lambda_{B^*}$  and  $\Lambda_D$  being the cutoff masses associated with the  $B^*$  and  $D$  mesons, respectively. We use the common value  $\Lambda = \Lambda_{B^*} = \Lambda_D$ . A similar calculation is performed to obtain the  $BD^*$  loop contribution, namely, in Eqs. (46) and (47), as well as in the form factors, by replacing  $(B^*, D) \rightarrow (B, D^*)$ .

The choice of cutoff value has nonegligible impacts on the results. We use the common cutoff  $\Lambda \equiv \Lambda_{B, B^*, D, D^*, K, K^*}$  by varying the  $\Lambda$  value. The  $\Lambda$  value may be associated with the energies to probe the internal structure of the mesons. In the previous study [72] it was observed that when the values of the cutoff becomes close to the masses of the mesons in calculating the self-energies, a certain larger cutoff mass value range did not make sense to serve as the form factors. This is because the Compton wavelengths of the corresponding cutoff mass values reach near and/or smaller than those of the meson sizes. Therefore, we need to constrain the cutoff  $\Lambda$  value in such a way that the form factors reflect properly the finite size of the mesons. Based on the heavy quark and heavy meson symmetry, we use the same range of values for  $\Lambda$  as it was practiced for the quarkonia [72]. Thus, we use the values,  $\Lambda = 2000, 3000, 4000, 5000$  and  $6000$  MeV.

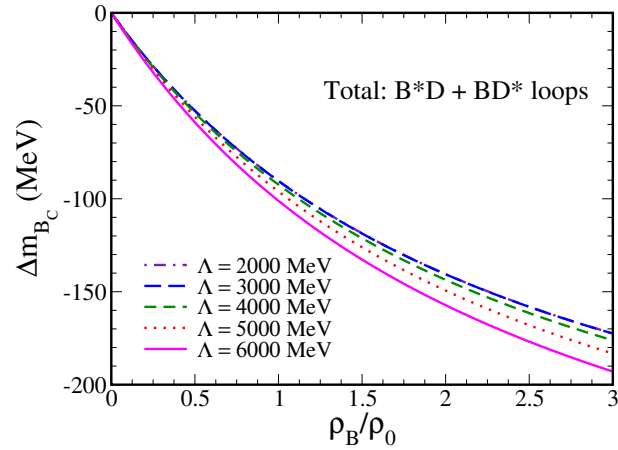


**Figure 9.** Total  $(B^*D + BD^*)$  loop contribution for the in-medium  $B_c$  mass shift versus baryon density ( $\rho_B/\rho_0$ ) for five different values of the cutoff mass  $\Lambda$ .

Including the total  $(BD^* + B^*D)$  loop contributions, the  $B_c$  mass shift amount  $\Delta m_{B_c}(BD^* + B^*D)$  at  $\rho_0$  ranges from -90.4 to -101.1 MeV ( $m_{B_c}^*(BD^* + B^*D) = 6184.1$  to  $6173.4$  MeV). Later, we will compare the  $B_c$  mass shift and those of the  $\eta_b$  and  $\eta_c$ .

Next, we study the in-medium mass shift of the  $B_c^*$  meson calculated in the rest frame of  $B_c^*$ . For the  $B_c^*$  self-energy, we include only the  $BD$  loop contribution, as already commented based on the  $Y$  and  $J/\psi$  self-energies [72],

$$\Sigma_{B_c^*}^{BD}(m_{B_c^*}^*) = \frac{-4g_{B_c^* BD}^2}{3\pi^2} \int dq q^4 I_{B_c^*}^{BD}(q^2) F_{B_c^* BD}(q^2), \quad (48)$$

where  $I_{B_c^*}^{BD}(q^2)$  is expressed by,

$$I_{B_c^*}^{BD}(q^2) = \frac{1}{(q_0 - \omega_B^*)(q_0 - m_{B_c^*}^* + \omega_D^*)(q_0 - m_{B_c^*}^* - \omega_D^*)} \Big|_{q_0 = -\omega_B^*} + \frac{1}{(q_0 + \omega_B^*)(q_0 - \omega_B^*)(q_0 - m_{B_c^*}^* - \omega_D^*)} \Big|_{q_0 = m_{B_c^*}^* - \omega_D^*}, \quad (49)$$

with  $q = |\mathbf{q}|$ . In Eq. (48),  $F_{B_c^* BD}(q^2)$  is given by the product of the form factors,  $F_{B_c^* BD}(q^2) = u_{B_c^* B}(q^2)u_{B_c^* D}(q^2)$ , with  $u_{B_c^* B}$  and  $u_{B_c^* D}$  being

$$u_{B_c^* B} = \left( \frac{\Lambda_B^2 + m_{B_c^*}^2}{\Lambda_B^2 + 4\omega_B^2(q^2)} \right)^2 \text{ and } u_{B_c^* D} = \left( \frac{\Lambda_D^2 + m_{B_c^*}^2}{\Lambda_D^2 + 4\omega_D^2(q^2)} \right)^2.$$

Again we use  $\Lambda = \Lambda_B = \Lambda_D$  ranging 2000 to 6000 MeV.

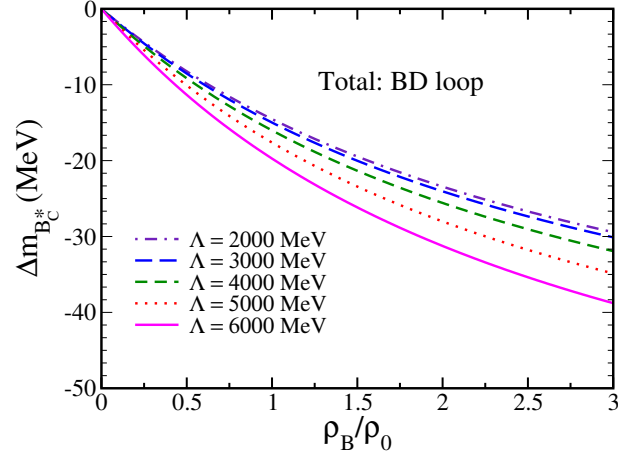


**Figure 10.**  $BD$  loop (total) contribution for the in-medium  $B_c^*$  mass shift versus baryon density ( $\rho_B/\rho_0$ ) for five different values of the cutoff mass  $\Lambda$ .

#### 4.5. Comparison with heavy quarkonia

We now compare in Fig. 11 the results of  $B_c$  and  $B_c^*$  [84], with those of the heavy quarkonia [11,37,67,72]. Since the  $B_c$  meson is a pseudoscalar meson, we compare with the bottomonium  $\eta_b$  and charmonium  $\eta_c$  (upper panel), while for the  $B_c^*$  meson, we compare with those of the  $Y$  and  $J/\psi$  (lower panel).

For the comparison, we would like to emphasize that we use the empirically extracted SU(4) sector coupling constants for the charm sector ( $\eta_c$  and  $J/\psi$ ), which would be more reasonable than using the empirically extracted SU(5) sector coupling constant from the  $\Gamma(Y \rightarrow e^+e^-)$ , since the SU(5) flavor symmetry breaking is expected to be much larger than that of the SU(4) based on the quark masses.

The value for the coupling constant of the vertex  $J/\psi DD$  used in the calculation of  $J/\psi$  mass shift, was obtained from the experimental data for  $\Gamma(J/\psi \rightarrow e^+e^-)$  by the VMD hypothesis (note that the slight difference,  $7.64 \rightarrow 7.7$  below, but the difference is negligible)

$$g_{J/\psi DD} = \frac{g}{\sqrt{6}} \approx 7.7, \quad (50)$$

where  $g$  is the universal SU(4) coupling constant.

For the coupling constant  $g_{\eta_c DD^*}$  used in the calculation of the  $\eta_c$  mass shift, we also adopt the SU(4) symmetry for the charm sector, which gives the relation

$$g_{\eta_c DD^*} = g_{J/\psi DD} = \frac{g}{\sqrt{6}} \approx 7.7. \quad (51)$$

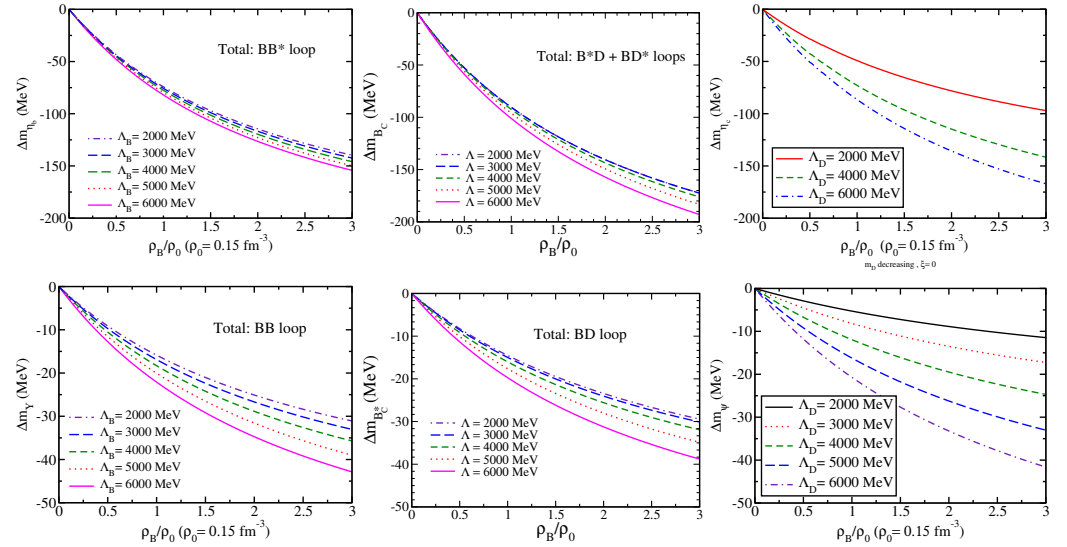
A comprehensive list of the values used for the coupling constants is presented in Table. 2.

Although we make this comparison, we repeat that this is not done based on a rigorous SU(5) symmetry of the same footing. Namely, the coupling constant  $g$  is calculated for the charm sector ( $J/\psi$ ,  $\eta_c$ ) based on the SU(4) symmetry, and for the bottom sector ( $Y$ ,  $\eta_b$ ) and ( $B_c$ ,  $B_c^*$ ) based on the SU(5) symmetry. This comparison would make a sense based on the fact that SU(5) symmetry is much more broken by the quark masses than that of SU(4).

**Table 2.** Coupling constant values in SU(4) and SU(5) symmetries.

	SU(4)
$g$	18.9
$g_{J/\psi DD}$	7.7
$g_{\eta_c DD^*}$	7.7
	SU(5)
$g$	33.4
$g_{YBB}$	13.2
$g_{\eta_b BB^*}$	13.2
$g_{B_c B^* D}$	11.9
$g_{B_c^* BD}$	11.9

Note that, although for the mass shift amount  $\Delta m_{\eta_c}$  [67], the cutoff mass values  $\Lambda = \Lambda_D = \Lambda_{D^*} = 3000$  and  $5000$  MeV are missing, it is irrelevant to see the mass shift range for the cutoff range between the  $2000$  MeV and  $6000$  MeV.

**Figure 11.** Comparison of the mass shift of  $B_c$  with  $\eta_b$  and  $\eta_c$  (upper panel) as well as of  $B_c^*$  with  $Y$  and  $J/\psi$  (lower panel).

In the study of the  $\eta_c$  mass shift, only the  $DD^*$  loop contribution was included, and it corresponds to the mass shift value  $\Delta m_{\eta_c}(DD^*)$  at  $\rho_0$  ranges  $-49.2$  to  $-86.5$ , for the cutoff mass values  $\Lambda_D = \Lambda_{D^*}$  of  $2000$ ,  $4000$  and  $6000$  MeV. The estimated values for the  $\eta_b$  mass shift  $\Delta m_{\eta_b}(BB^*)$  at  $\rho_0$  including only the  $BB^*$  loop, ranges from  $-74.2$  to  $-82.0$  MeV, where the same range of the cutoff mass value is applied for the present study. The total  $B^*D + BD^*$  loop contributions for the  $B_c$  mass shift give more negative mass shift than those of the  $\eta_b$  and  $\eta_c$ . This fact indicates that the  $B_c$  mass shift value does not show the middle range mass shift value between those of the  $\eta_c$  and  $\eta_b$ , may be different from one's naive expectation.

Next, we compare the mass shift behaviors of  $Y$ ,  $B_c^*$  and  $J/\psi$  in Fig 11 (lower panel). The  $Y$  and  $J/\psi$  mass shift values are calculated by taking respectively only the (minimal)  $BB$ , and  $DD$  loop contributions corresponding to the present  $B_c^*$  meson treatment with only the  $BD$  loop. The mass shift value  $\Delta m_Y(BB)$  at  $\rho_0$  ranges from  $-15.9$  to  $-22.1$  MeV, while  $\Delta m_{J/\psi}(DD)$  at  $\rho_0$  ranges from  $-5.3$  to  $-20.7$ , when the common range of the  $\Lambda$  ( $2000$  to  $6000$  MeV) is used. The corresponding  $B_c^*$  mass shift value  $\Delta m_{B_c^*}(BD)$  at  $\rho_0$  ranges from  $-14.5$  to  $-19.7$  MeV. The  $B_c^*$  meson in-medium mass shift value is less dependent on the cutoff mass value than that of the  $J/\psi$ . Although the mass shift behavior is depend on the cutoff mass

value, the global trend shown in the lower panel of Fig. 11 indicates that the  $\Delta m_{B_c^*}$  is more or less the middle of the corresponding  $\Delta m_Y$  and  $\Delta m_{J/\psi}$ .

### 5. Meson-nucleus potential

The baryon density dependence of the mass shift behaviors of the  $\eta$ ,  $\eta'$ ,  $\phi$ ,  $\eta_c$ ,  $J/\psi$ ,  $\eta_b$ ,  $Y$ ,  $B_c$ , and  $B_c^*$  mesons in nuclear matter, shown in Figs. 2, 4 (left panel), 5, 6, 7, 8, 9, and 10 indicate that the nuclear medium provides attraction to these mesons, and opens the possibility for their binding to nuclei.

Therefore, we now consider the nuclear bound states for several of these mesons, which we generally denote the meson as  $h$ , when the mesons have been produced nearly at rest inside nucleus  $A$ , and study the following nuclei in a wide range of masses, namely  $^4\text{He}$ ,  $^{12}\text{C}$ ,  $^{16}\text{O}$ ,  $^{40}\text{Ca}$ ,  $^{48}\text{Ca}$ ,  $^{90}\text{Zr}$ ,  $^{197}\text{Au}$ , and  $^{208}\text{Pb}$ .

In a local density approximation, the meson  $h$  potential within a nucleus  $A$  is given by

$$V_{hA}(r) = U_{hA}(r) - \frac{i}{2}W_{hA}(r), \quad (52)$$

where  $r$  is the distance from the center of the nucleus;  $U_{hA}(r) = \Delta m_h(\rho_B(r))$ , with  $\Delta m_h(\rho_B)$  the value of mass shift computed previously for meson  $h$  as a function of nuclear density  $\rho_B$ ; and  $\rho_B^A(r)$  is the baryon density distribution in the nucleus  $A$ . The imaginary part of the potential  $W_{hA}(r)$ , is related to the absorption of the meson  $h$  in the nuclear medium, is included only for the  $\phi$ ,  $\eta$ , and  $\eta'$  mesons in the present study. For the  $\phi$  meson it is given by  $W_{\phi A}(r) = \Gamma_{\phi}(\rho_B^A(r))$  where  $\Gamma_{\phi}(\rho_B)$  is the  $\phi$  decay width in a nucleus  $A$ , Eq. (16). For the  $\eta$  and  $\eta'$  mesons  $W_{hA}(r) = -\gamma\Delta m_h(\rho_B(r)) + \gamma_h^{\text{vac}}$ . Here  $\Gamma_h^{\text{vac}}$  the meson decay width in vacuum ( $\Gamma_{\eta}^{\text{vac}} = 1.31$  keV and  $\Gamma_{\eta'}^{\text{vac}} = 0.188$  MeV [91]), and  $\gamma$  is a phenomenological parameter used to simulate the strength of the absorption of the meson in the nuclear medium. The values of the  $\gamma$  parameter used below cover the estimated widths of the  $\eta$  and  $\eta'$  mesons in the nuclear medium [123]. The nuclear density distributions  $\rho_B^A(r)$  for the nuclei listed above are calculated using the QMC model [116], except for  $^4\text{He}$ , which we take from Ref. [117]. Before proceeding, a comment on the use of the local density approximation might be useful, in particular for  $^4\text{He}$  nuclei. At the position  $r$  inside nucleus  $A$ , the nuclear density is  $\rho_A(r)$ , and the potentials (effective masses) are taken from the uniform (constant) nuclear density calculation in nuclear matter. For small nuclei, such as  $^4\text{He}$ , this might appear problematic at first sight since for such nucleus the  $r$ -dependence of the nuclear density is expected to be relatively rapid (strong). Because the  $r$ -dependence of the nuclear density can be faster than for larger nuclei, depending on the interval value  $\Delta r$ , to use the local density approximation, it might not be good enough to assume the uniform nuclear density between the interval  $\Delta r$ . However, our calculation uses  $\Delta r = 0.04$  fm with the interpolation, and we expect the local density approximation even for the  $^4\text{He}$  nucleus is sufficiently good. For the  $^4\text{He}$  nucleus, the nuclear density change within the interval 0.04 fm is very small and thus can be regarded as a constant density.

In the following figures we present the meson-nucleus potentials for some selected nuclei computed using Eq. (52).

In Figs. 12 and 13 we present the  $\phi$ -meson potentials calculated for some nuclei, for three values of the cutoff parameter  $\Lambda_K$ , 2000, 4000 and 6000 MeV. One can see that the depth of the real part of the potential,  $U_{\phi}(r)$ , is sensitive to the cutoff parameter, from -20 MeV to -35 MeV for  $^4\text{He}$  and from -20 MeV to -30 MeV for  $^{208}\text{Pb}$  [101]. In addition, one can see that the imaginary part does not vary much with  $\Lambda_K$ . Furthermore, note the imaginary part of the potential is repulsive. This observation may well have consequences for the feasibility of experimental observation of the expected bound states [101].

In Figs. 14 and 15 we present, respectively, the  $\eta_c$ -meson potentials for selected nuclei listed above and various values of the cutoff parameter  $\Lambda_D$  [67], with the SU(4) breaking parameter of  $0.6/\sqrt{2}$  for the coupling constant as explained in Sec. 4.2. From the figures one can see that the  $\eta_c$  and  $J/\psi$  potentials in nuclei are attractive in all cases but its depth depends on the value of the cutoff parameter, being deeper the larger  $\Lambda_D$  becomes. This



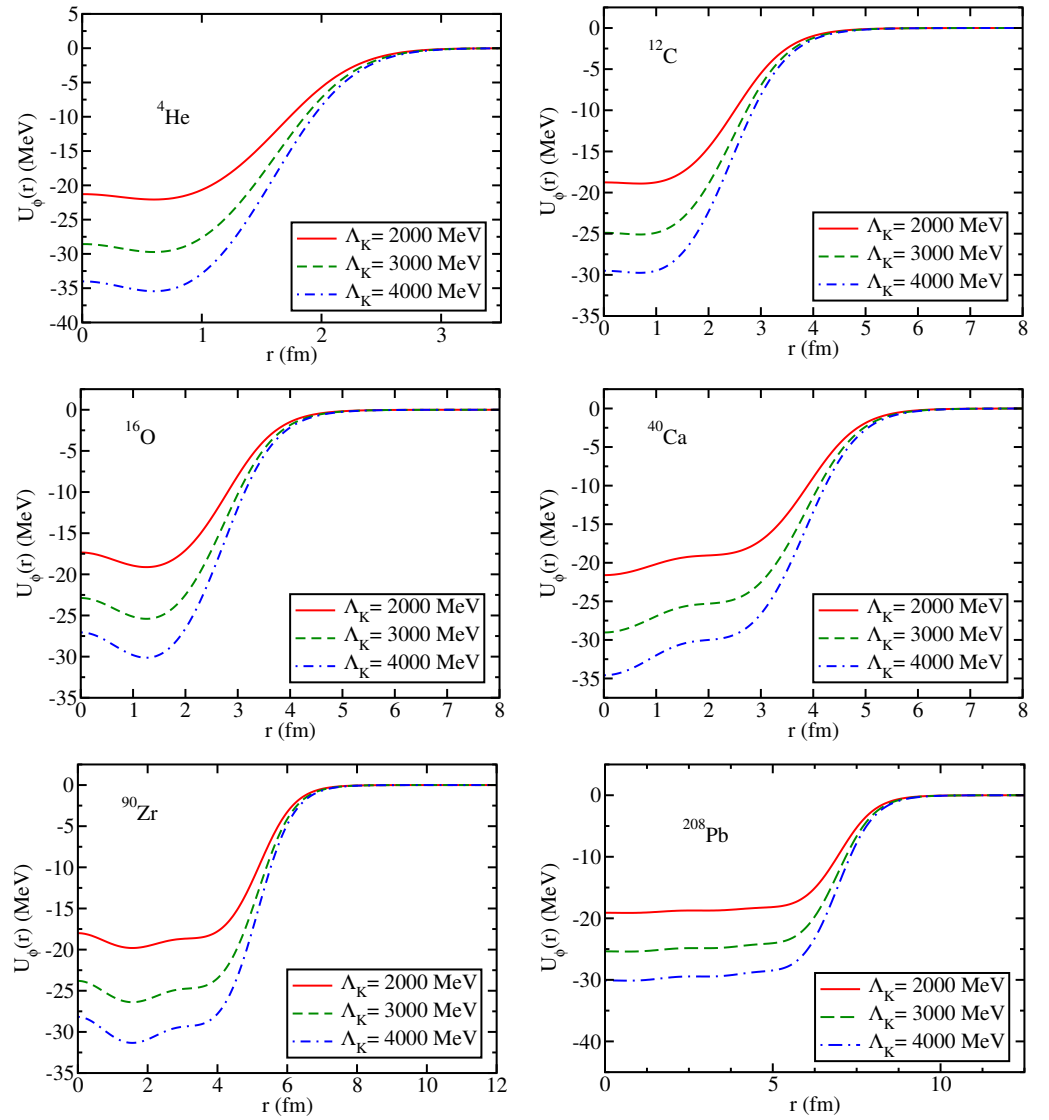


**Figure 12.** Real  $[U_\phi(r)](r)$  part of the  $\phi$ -meson-nucleus potentials in some nuclei selected, for three values of the cutoff parameter  $\Lambda_K$ .

dependence is, indeed, an uncertainty in the results obtained in our approach, when using an effective Lagrangian approach. Note that this is the same conclusion we reached from the mass shift computed in the previous section 4.2 [67].

In Figs. 16 and 17 we present the bottomonium-nucleus potentials for some of the nuclei listed above and the same values of the cutoff parameter  $\Lambda_B$  that were used in the computation of the mass shift in the previous section 4.3 [75]. We can see from Figs. 16 and 17 that the  $V_{hA}$  potentials, for  $h = Y$  and  $\eta_b$ , respectively, are attractive for all nuclei and all values of the cutoff mass parameter used [75]. However, for each nuclei, the depth of the potential depends on the value of the cutoff parameter, being more attractive the larger  $\Lambda_B$  becomes. This dependence is expected and is, indeed, an uncertainty in the results obtained in our approach [75].

Next, the calculated potentials for the  $\eta$  and  $\eta'$  mesons in nuclei are shown in Figs. 18 and 19 [123]. These figures show that all potentials for the  $\eta$  and  $\eta'$  in nuclei are attractive. This is so because the corresponding value of the mass shift (in nuclear matter) is negative for both mesons (see Sec. 2). The differences in the potentials, for a given meson, reflect the differences in the baryon density distributions for the nuclei studied [123]. Furthermore,

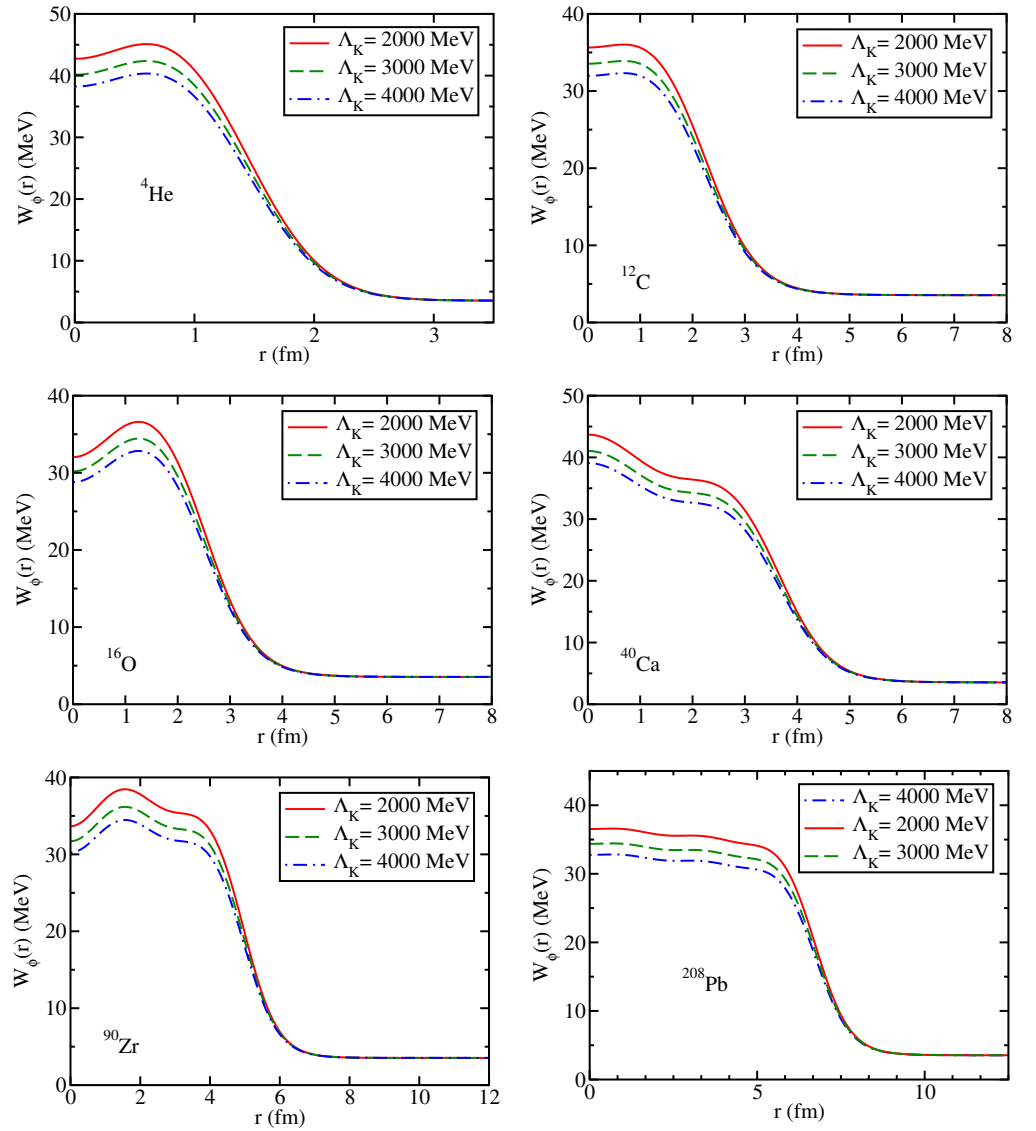


**Figure 13.** Imaginary  $[W_\phi(r)]$  part of the  $\phi$ -meson-nucleus potentials in some nuclei, for three values of the cutoff parameter  $\Lambda_K$ .

note that for a given nucleus, the potentials for the  $\eta$  and  $\eta'$  are very similar, the reason for this is that values of the mass shift for the are very similar, as shown in Fig. 2 [123].

Finally, the nuclear strong interaction potentials for the  $B_c^\pm$ -A systems are presented in Fig. 20, together with the attractive and repulsive Coulomb potentials, where the Coulomb potentials are not added, but they will be included in calculating the bound state energies in next section.

## 6. Numerical results for the meson-nucleus bound state energies

We now compute the meson  $h$ -nucleus  $A$  bound state energies, for  $h = \eta, \eta', \phi, \eta_c, J/\psi, \eta_b, Y$  and  $B_c^\pm$ , in a wide range of nuclear masses  $A = {}^4\text{He}, {}^{12}\text{C}, {}^{16}\text{O}, {}^{40}\text{Ca}, {}^{48}\text{Ca}, {}^{90}\text{Zr}, {}^{197}\text{Au}$ , and  ${}^{208}\text{Pb}$  by solving the Klein-Gordon equation (KGE)

$$\left(-\nabla^2 + (m + V(\mathbf{r}))^2\right)\psi(\mathbf{r}) = \mathcal{E}^2\psi(\mathbf{r}) \quad (53)$$

where  $V(\mathbf{r}) = V(r)$  is the scalar nuclear potential associated with mass shift, given by Eq. (52),  $r = |\mathbf{r}|$  is the distance from the nucleus, and  $m$  is the reduced mass of the

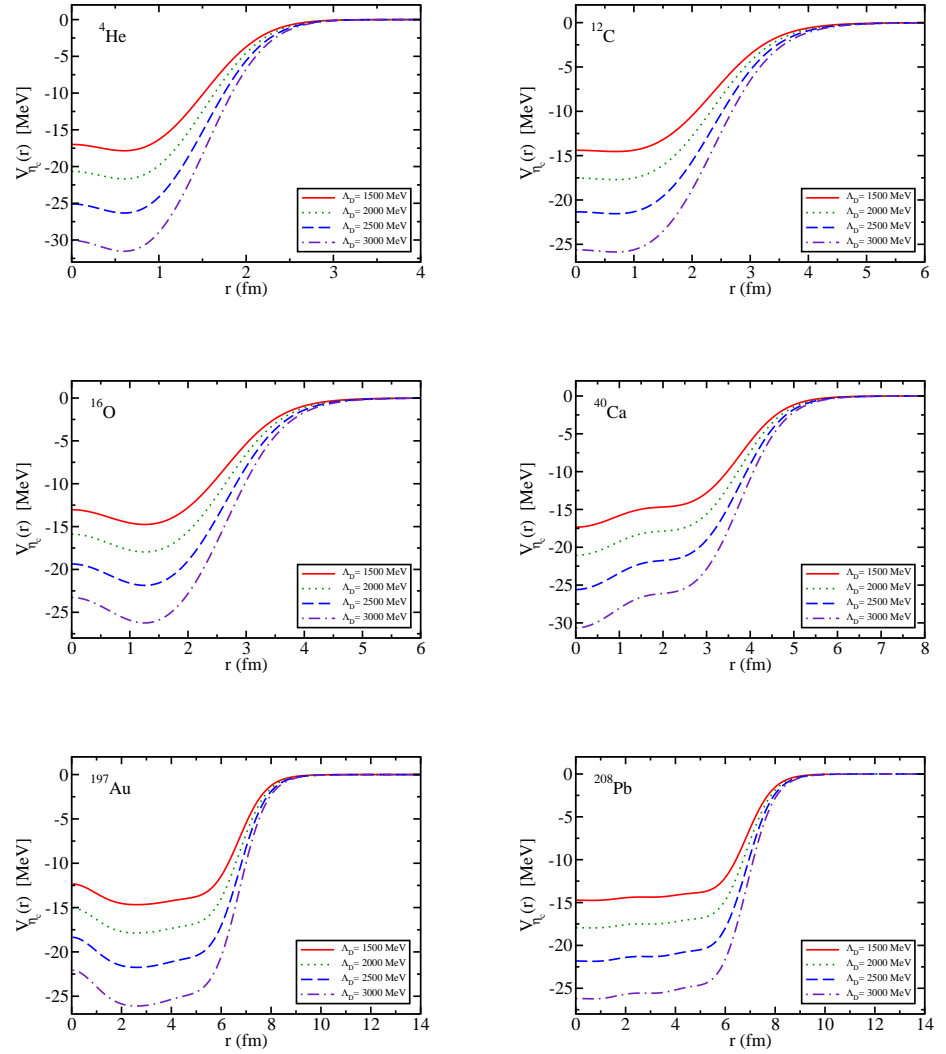


**Figure 14.**  $\eta_c$ -nucleus potentials for various nuclei and values of the cutoff parameter  $\Lambda_D$  [67]. Note that the potentials are calculated with the SU(4) breaking parameter,  $0.6/\sqrt{2}$  for the coupling constant, as explained in Sec. 4.2.

meson  $h$ -nucleus  $A$  system  $m_h m_A / (m_h + m_A)$ , in vacuum. The bound state energies  $E$  and widths  $\Gamma$  are given by  $E = \mathcal{E} - m$  and  $\Gamma = -2\text{Im } \mathcal{E}$ , respectively, where  $\mathcal{E}$  is the energy eigenvalue in Eq. (53). Note that, when the Coulomb or vector potential is relevant, the right hand side of Eq. (53) must be modified properly as  $\mathcal{E}^2 \rightarrow (\mathcal{E} - V_{V,\text{Coul}})^2$  with  $V_{V,\text{Coul}}$  being the vector and Coulomb potentials, respectively. See Ref. [115] for details.

Before proceeding to solve Eq. (53) we note that we have also solved to approximations of Eq. (53), namely the Schrödinger equation and also the KGE dropping the  $V^2(\mathbf{r})$  term in Eq. (53) for some meson-nucleus systems. In all cases we obtain essentially the same results, which do not change the conclusions about the existence of the bound states.

We solve the Klein-Gordon equation using the momentum space methods [118]. Here, Eq. (53) is first converted to momentum space representation via a Fourier transform, followed by a partial wave-decomposition of the Fourier-transformed potential, or we obtain directly the partial wave decomposition in momentum space by a double Spherical Bessel transform. For  $\eta$ ,  $\eta'$ ,  $\phi$ ,  $\eta_c$  and  $J/\psi$ , the method used is the partial wave-decomposition of the Fourier-transformed potential. For the  $B_c^\pm$  we employ the direct double Spherical Bessel transform, and for  $Y$  and  $\eta_b$  we use both methods. Then, for a given value of angular

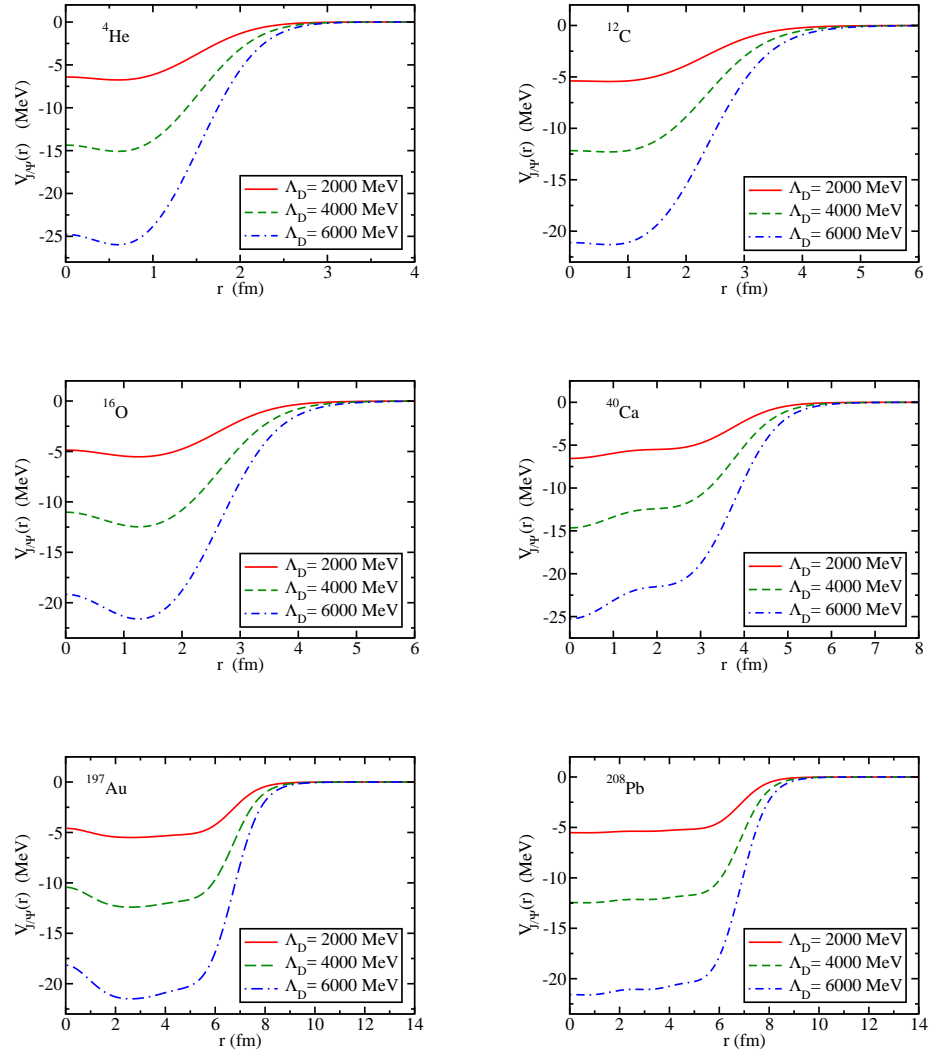


**Figure 15.**  $J/\psi$ -nucleus potentials for various nuclei and values of the cutoff parameter  $\Lambda_D$ .

momentum  $\ell$ , the eigenvalues of the resulting equation are found by the inverse iteration eigenvalue algorithm. The detailed comparison and discussions were made in Ref. [115], and it turned out that the main conclusions remain valid in both methods. The calculated bound state energies are similar, with, at most, few MeV difference, which we would think within the desired experimental accuracy for the strong interaction bound state energy measurement.

In Table 3 we show our results for the  $\phi$ -nucleus bound state energies and half widths, obtained with and without the imaginary part of the potential, for three values of the cutoff parameter [101].

We first analyse the case in which the imaginary part of the  $\phi$ -nucleus potential,  $W_\phi(r)$ , is set to zero. These results are shown in parenthesis in Table 3. From the values shown in parenthesis, we see that the  $\phi$ -meson is expected to form bound states with all the seven nuclei selected, for all values of the cutoff parameter  $\Lambda_K$  studied. However, the bound state energy is obviously dependent on  $\Lambda_K$ , increasing in magnitude with  $\Lambda_K$  [101].

Next, we discuss the results obtained when the imaginary part of the potential is retained. Adding the absorptive part of the potential, the situation changes considerably. From the results presented in Table 3 we note that for the largest value of the cutoff parameter, which yields the deepest attractive potentials, the  $\phi$ -meson is expected to form

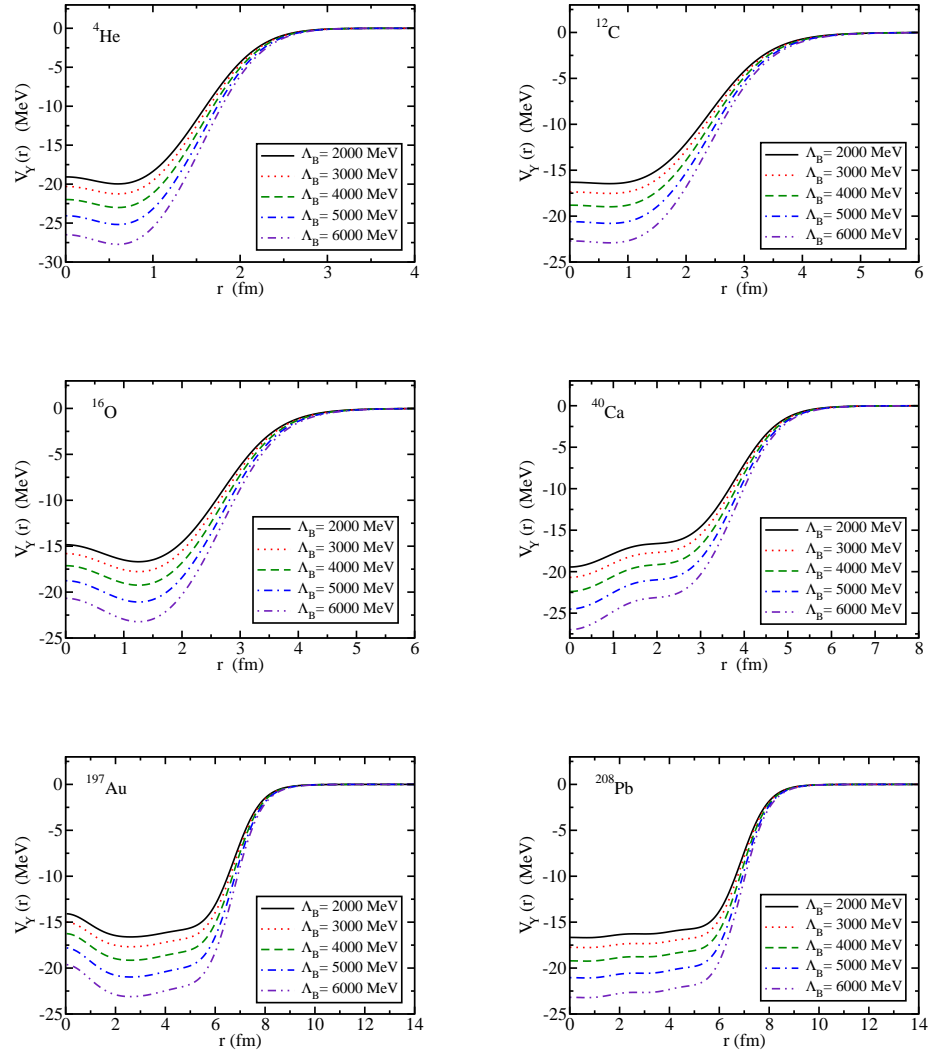


**Figure 16.** Y-nucleus potentials for various nuclei with several values of the cutoff parameter  $\Lambda_B$ .

bound states in all the nuclei selected, including the lightest  ${}^4\text{He}$  nucleus. However, in this case, whether or not the bound states can be observed experimentally, is sensitive to the value of the cutoff parameter  $\Lambda_K$  [101]. Given that the widths are large, the signal for the formation of the  $\phi$ -nucleus bound states may be difficult to identify experimentally.

We also observe that the width of the bound state is insensitive to the values of  $\Lambda_K$  for all nuclei. Furthermore, since the so-called dispersive effect of the absorptive potentials are repulsive, the bound states disappear completely in some cases, even though they were found when the absorptive part was set to zero [101]. This feature is obvious for the  ${}^4\text{He}$  nucleus, making it especially relevant to the future experiments, planned at J-PARC and JLab using light and medium-heavy nuclei [119–122].

The bound state energies  $E$  of the  $\eta_c$ -nucleus system were calculated for four values of the cutoff parameter  $\Lambda_D$  and are listed in Table 4 [67]. Note that, the  $\eta_c$  bound state energies are calculated with the SU(4) broken coupling constant by  $(0.6/\sqrt{2})g_{\eta_c DD}$ , thus the values shown below are expected to be smaller in magnitude than those calculated with the SU(4) symmetric coupling constant,  $g_{\eta_c DD}$ . (See Sec. 4.2.) These results show that the  $\eta_c$ -meson is expected to form bound states with all the nuclei studied, and this prediction is independent of the value of the cutoff parameter  $\Lambda_D$  [67]. However, the particular values for the bound state energies are clearly dependent on  $\Lambda_D$ , namely, each of them increases

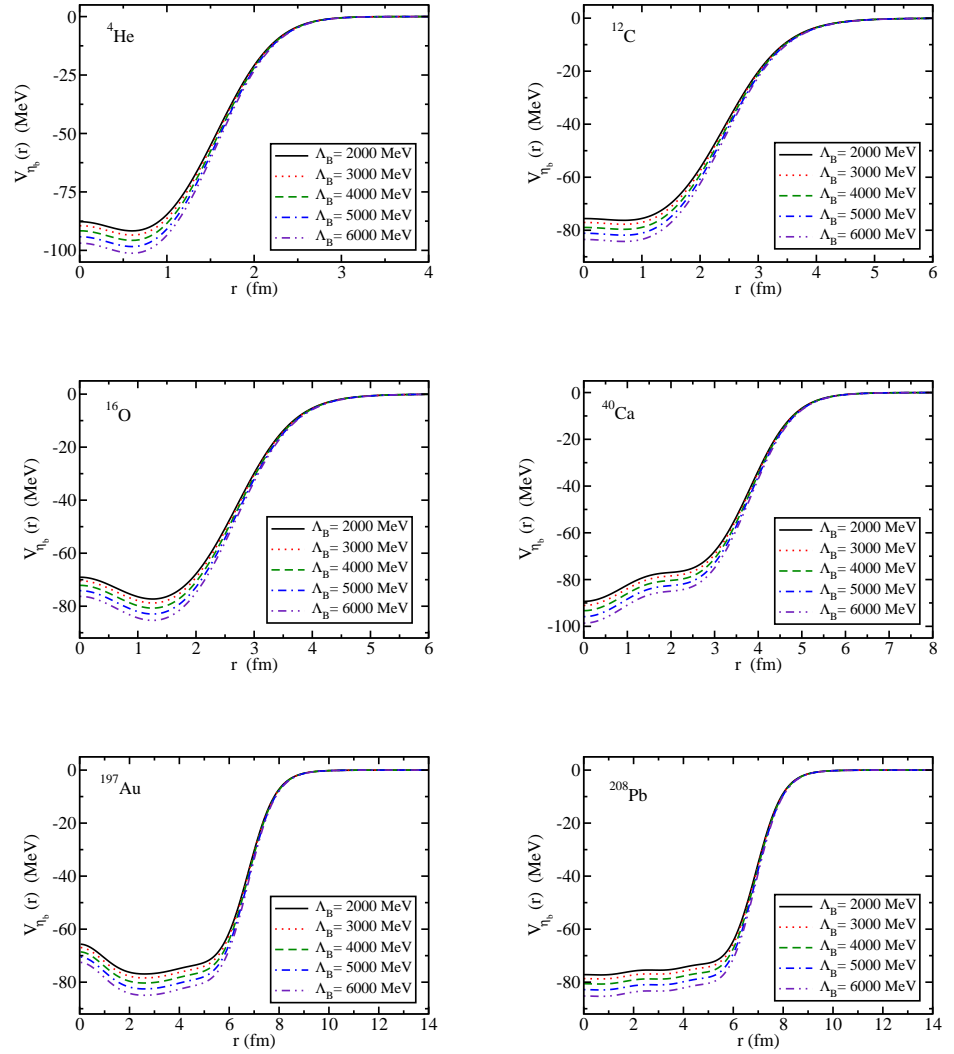


**Figure 17.**  $\eta_b$ -nucleus potentials for various nuclei with several values of the cutoff parameter  $\Lambda_B$ .

in absolute value as  $\Lambda_D$  increases. This was expected from the behavior of the  $\eta_c$  potentials, since these are deeper for larger values of the cutoff parameter. Note also that the  $\eta_c$  bounds more strongly to heavier nuclei [67].

We remind that we have ignored the natural width of  $\sim 31$  MeV [126], in free space of the  $\eta_c$  and this could be an issue related to the observability of the predicted bound states. Furthermore, we have no reason to believe the width will be suppressed in medium. Thus, even though it could be difficult to resolve the individual states, it should be possible to see that there are bound states which is the main point here. It remains to be seen by how much the inclusion of a repulsive imaginary part will affect the predicted bound states. We believe this can be done in future work.

The results for the  $J/\psi$ -nucleus bound states are presented in Table 5. These results show that the  $J/\psi$  is expected to form  $J/\psi$ -nuclear bound states for nearly all the nuclei considered, except some cases for  ${}^4\text{He}$ , for all values of the cutoff parameter  $\Lambda_D$  [124,125]. Therefore, it will be possible to search for the bound states, for example, in a  ${}^{208}\text{Pb}$  nucleus at JLab the 12 GeV upgraded facility. In addition, one can expect quite rich spectra for medium and heavy mass nuclei. Of course, the main issue is to produce the  $J/\psi$  meson with nearly stopped kinematics, or nearly zero momentum relative to the nucleus. Since the present



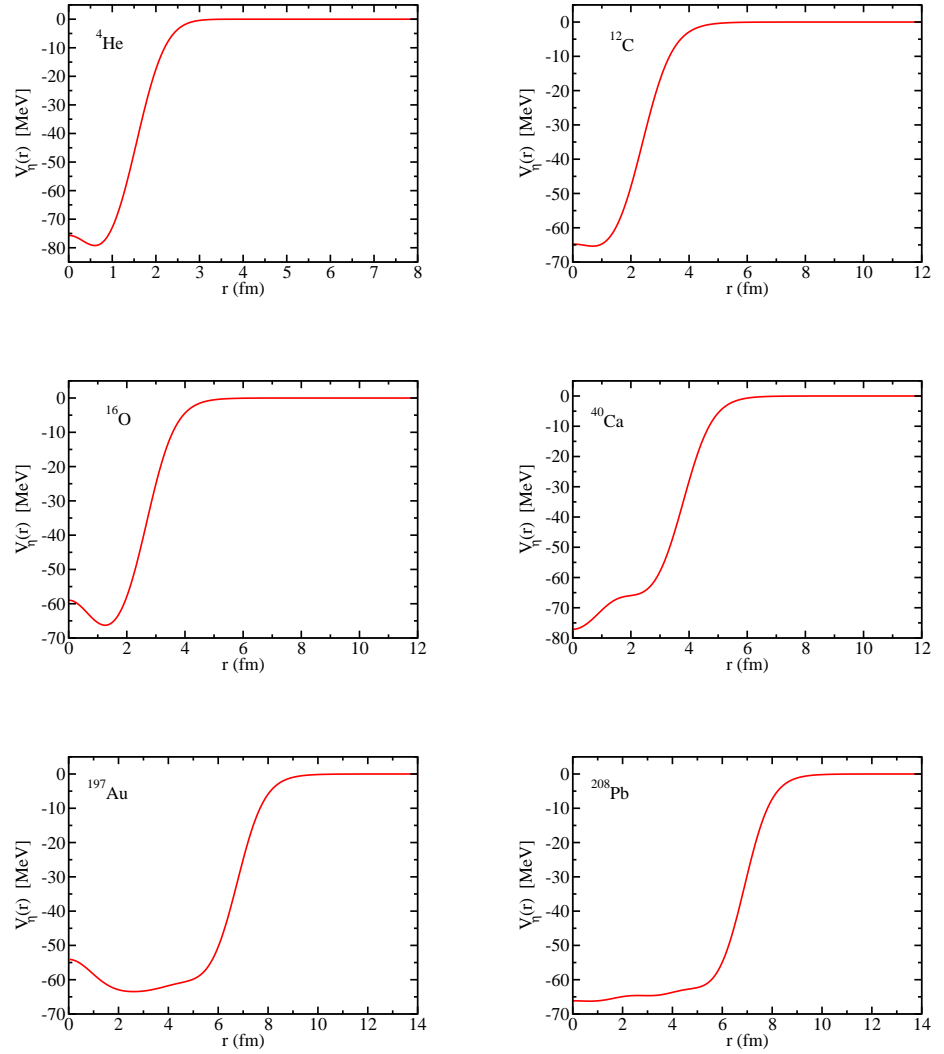


**Figure 18.**  $\eta$ -nucleus potentials for several nuclei.

results imply that many nuclei should form  $J/\psi$ -nuclear bound states, it may be possible to find such kinematics by careful selection of the beam and target nucleus [124,125].

The bound state energies  $E$  of the  $Y$ -nucleus and  $\eta_b$ -nucleus systems are listed in Tables 6 to 9, respectively, for all nuclei listed at the beginning of this section and the same range of values for the cutoff mass parameter as used in the mass shift calculation (see Sec. 4.3) [75]. We note that for the  $Y$ -nucleus systems we have only listed a few bound states for each nucleus, since that number increases with the mass of the nucleus and for the heaviest of these,  ${}^{208}\text{Pb}$ , the number of bound states is quite large. For the  ${}^{208}\text{Pb}$  nucleus we have found  $\sim 70$  states [75].

In Table 8 we show the  $\eta_b$ -nucleus bound state energies for the same nuclei and range of values of the cutoff mass parameter as in Table 6 [75]. Furthermore, as in the case of the  $Y$ -nucleus bound state energies, for each nucleus we have listed only a few bound states. For the  ${}^{208}\text{Pb}$  nucleus we have  $\sim 200$  states and clearly it is not practical to show them all [75].

These results given in Tables 6 to 9 show that the  $Y$  and  $\eta_b$  mesons are expected to form bound states with all the nuclei studied, independent of the value of the cutoff parameter  $\Lambda_B$ . However, the particular values for the bound state energies are dependent on the cutoff parameter values, increasing in absolute value as the cutoff parameter increases. This dependence was expected from the behavior of the bottomonium-nucleus potentials,

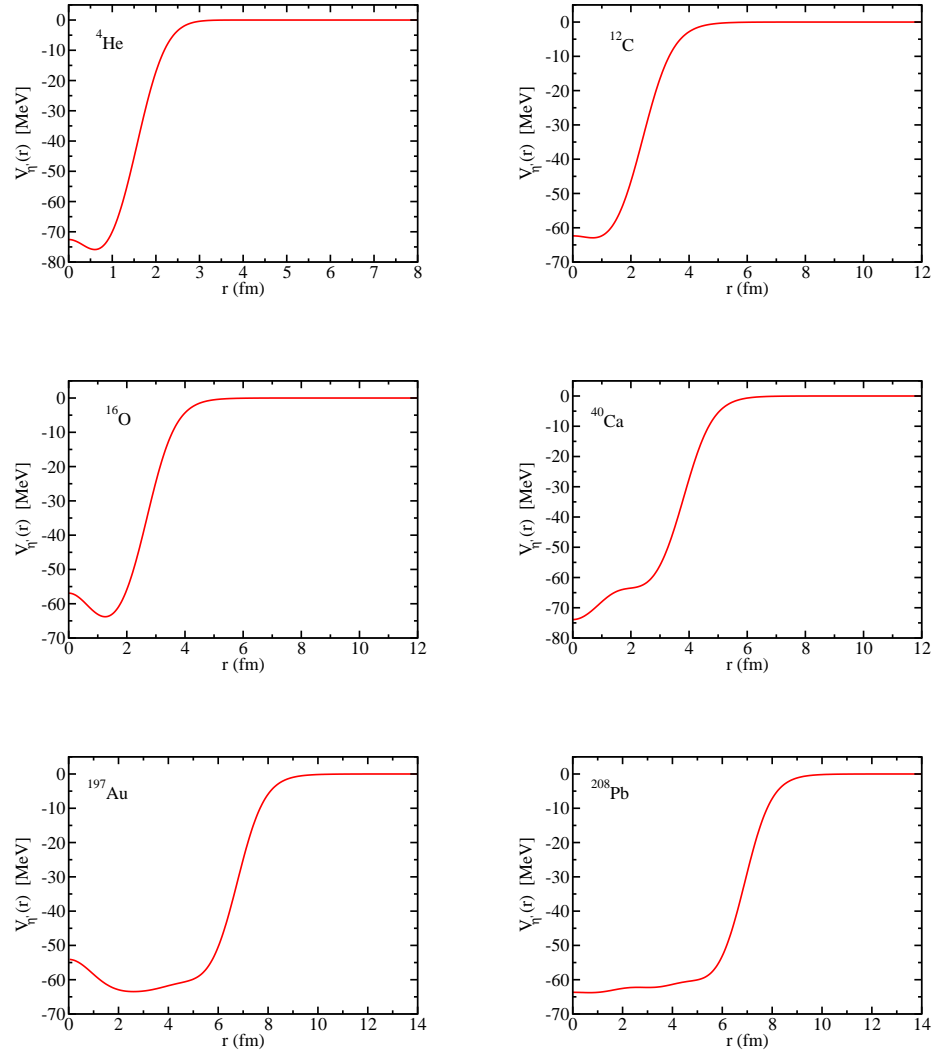


**Figure 19.**  $\eta'$ -nucleus potentials for several nuclei.

since these are more attractive for larger values of the cutoff parameter. Note also that bottomonium ( $\eta_b$  or  $Y$ ) binds more strongly to heavier nuclei and therefore a richer spectrum is expected for these nuclei [75].

However, from Tables 6 to 9, we see that the bound state energies for the  $\eta_b$  are larger than those of the  $Y$  for the same nuclei and range of cutoff values explored. These differences are probably due to two reasons: (a) the couplings  $g_{\eta_b BB^*}$  and  $g_{Y BB^*}$  are very different. Indeed, the results obtained in Ref. [67] on the  $\eta_c$  nuclear bound state energies are closer to those of the  $J/\psi$  when the  $SU(4)$  flavor symmetry is broken, such that  $g_{\eta_c DD^*} = (0.6/\sqrt{2}) g_{J/\psi DD} \simeq 0.424 g_{J/\psi DD}$  [67,105]. Thus, a reduced coupling  $g_{\eta_b BB^*}$  can bring the  $\eta_b$  nuclear bound state energies closer to those the  $Y$ , since the  $\eta_b$  self-energy is proportional to  $g_{\eta_b BB^*}^2$ . (b) the form factors are not equal for the vertices  $YBB$  and  $\eta_b BB^*$ , and we have to readjust the cutoff values, which means  $\Lambda_B \neq \Lambda_{B^*}$ , and the comparisons for the mass shift values and bound state energies have to be made for different values of the cutoff parameters.

The bound-state energies associated with each energy level can be confirmed by analyzing the number of nodes in the corresponding coordinate space wave function as described in Ref. [115]. We present the wave functions of some meson-nucleus systems

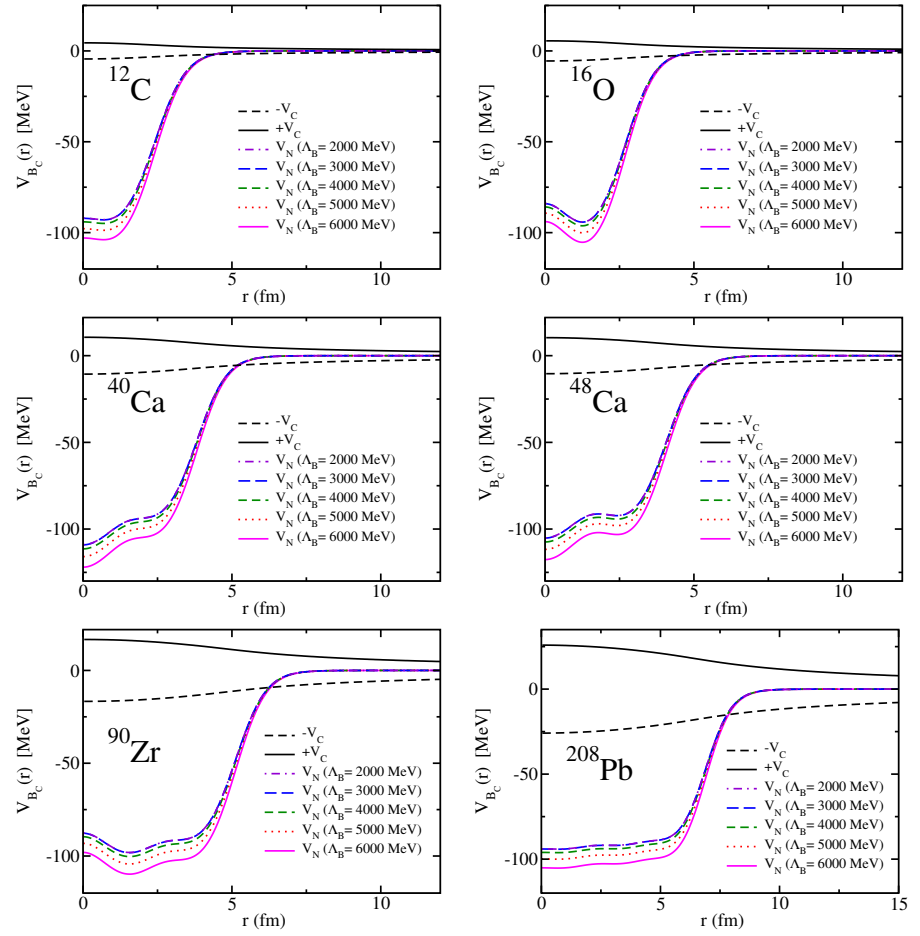


**Figure 20.** Attractive and repulsive Coulomb potentials, together with the strong nuclear potentials for the  $B_c^\pm$ - $A$  systems.

and cutoff values in Appendix A, which will help to understand better the meson-nucleus bound systems.

In Tables 10 and 11, we show, respectively, the results for the bound state energies ( $E$ ) and full widths ( $\Gamma$ ) of the  $\eta$ - and  $\eta'$ -mesic nuclei of mass number  $A$ , obtained by solving the Klein-Gordon equation, for various values of the strength of the imaginary part of the potential  $\gamma = 0.0, 0.25, 0.5, 1.0$ . (See below Eq. (52) about the  $\gamma$ .) The results for  $\gamma = 0$ , for both the  $\eta$  and  $\eta'$  mesons, correspond to the case where the imaginary part of the potential has been ignored. The bound state energies and full widths are obtained from the complex energy eigenvalue  $\mathcal{E}$  as  $\mathcal{E} = E + m - i\Gamma/2$ . We also note that for each nucleus, we have computed all bound states but have only listed up to four. In fact, the number of bound states increases with the mass of the nucleus such that for the heavier nuclei we have a richer structure of bound states. Furthermore, we note that the relativistic corrections shallower the bound state energies for the  $\eta$  and  $\eta'$  by approximately 2 MeV and 1 MeV, respectively.

From Tables 10 and 11, (column with  $\gamma = 0$ ) we conclude that the  $\eta$  and  $\eta'$  are expected to form bound states with all the nuclei considered.

However, the situation changes appreciably once we take into account the absorption effects of these mesons by nuclei, which we simulate with nonzero phenomenological parameter  $\gamma$ . We study the values  $\gamma = 0.25, 0.5, 1.0$ , where a larger values means a stronger absorption of the meson by the nuclear medium. When  $\gamma \neq 0$ , some of the bound states that present when  $\gamma = 0$  disappear. The columns with  $\gamma = 0.25, \gamma = 0.5$ , and  $\gamma = 1.0$  in Tables 10 and 11 show the results for the bound state energies  $E$  and full widths  $\Gamma$  of the  $\eta$ -

**Table 3.**  $\phi$ -nucleus single-particle energies,  $E$ , and half widths,  $\Gamma/2$ , obtained with and without the imaginary part of the potential, for three values of the cutoff parameter  $\Lambda_K$ . When only the real part is included, where the corresponding single-particle energy  $E$  is given in parenthesis and  $\Gamma = 0$  for all nuclei. “n” indicates that no bound state is found. All quantities are given in MeV.

		$\Lambda_K = 2000$		$\Lambda_K = 3000$		$\Lambda_K = 4000$	
		$E$	$\Gamma/2$	$E$	$\Gamma/2$	$E$	$\Gamma/2$
${}^4_\phi\text{He}$	1s	n (-0.8)	n	n (-1.4)	n	-1.0 (-3.2)	8.3
${}^{12}_\phi\text{C}$	1s	-2.1 (-4.2)	10.6	-6.4 (-7.7)	11.1	-9.8 (-10.7)	11.2
${}^{16}_\phi\text{O}$	1s	-4.0 (-5.9)	12.3	-8.9 (-10.0)	12.5	-12.6 (-13.4)	12.4
	1p	n (n)	n	n (n)	n	n (-1.5)	n
${}^{40}_\phi\text{Ca}$	1s	-9.7 (-11.1)	16.5	-15.9 (-16.7)	16.2	-20.5 (-21.2)	15.8
	1p	-1.0 (-3.5)	12.9	-6.3 (-7.8)	13.3	-10.4 (-11.4)	13.3
	1d	n (n)	n	n (n)	n	n (-1.4)	n
${}^{48}_\phi\text{Ca}$	1s	-10.5 (-11.6)	16.5	-16.5 (-17.2)	16.0	-21.1 (-21.6)	15.6
	1p	-2.5 (-4.6)	13.6	-7.9 (-9.2)	13.7	-12.0 (-12.9)	13.6
	1d	n (n)	n	n (-0.8)	n	-2.1 (-3.6)	11.1
${}^{90}_\phi\text{Zr}$	1s	-12.9 (-13.6)	17.1	-19.0 (-19.5)	16.4	-23.6 (-24.0)	15.8
	1p	-7.1 (-8.4)	15.5	-12.8 (-13.6)	15.2	-17.2 (-17.8)	14.8
	1d	-0.2 (-2.5)	13.4	-5.6 (-6.9)	13.5	-9.7 (-10.6)	13.4
	2s	n (-1.4)	n	-3.4 (-5.1)	12.6	-7.4 (-8.5)	12.7
	2p	n (n)	n	n (n)	n	n (-1.1)	n
${}^{208}_\phi\text{Pb}$	1s	-15.0 (-15.5)	17.4	-21.1 (-21.4)	16.6	-25.8 (-26.0)	16.0
	1p	-11.4 (-12.1)	16.7	-17.4 (-17.8)	16.0	-21.9 (-22.2)	15.5
	1d	-6.9 (-8.1)	15.7	-12.7 (-13.4)	15.2	-17.1 (-17.6)	14.8
	2s	-5.2 (-6.6)	15.1	-10.9 (-11.7)	14.8	-15.2 (-15.8)	14.5
	2p	n (-1.9)	n	-4.8 (-6.1)	13.5	-8.9 (-9.8)	13.4
	2d	n (n)	n	n (-0.7)	n	-2.2 (-3.7)	11.9

**Table 4.**  $\eta_c$ -nucleus bound state energies for different values of the cutoff parameter  $\Lambda_D$ . All dimensional quantities are in MeV.

	$n\ell$	Bound state energies			
		$\Lambda_D = 1500$	$\Lambda_D = 2000$	$\Lambda_D = 2500$	$\Lambda_D = 3000$
${}^4_{\eta_c}\text{He}$	1s	-1.49	-3.11	-5.49	-8.55
${}^{12}_{\eta_c}\text{C}$	1s	-5.91	-8.27	-11.28	-14.79
	1p	-0.28	-1.63	-3.69	-6.33
${}^{16}_{\eta_c}\text{O}$	1s	-7.35	-9.92	-13.15	-16.87
	1p	-1.94	-3.87	-6.48	-9.63
${}^{40}_{\eta_c}\text{Ca}$	1s	-11.26	-14.42	-18.31	-22.73
	1p	-7.19	-10.02	-13.59	-17.70
	1d	-2.82	-5.22	-8.36	-12.09
	2s	-2.36	-4.51	-7.44	-10.98
${}^{48}_{\eta_c}\text{Ca}$	1s	-11.37	-14.46	-18.26	-22.58
	1p	-7.83	-10.68	-14.23	-18.32
	1d	-3.88	-6.40	-9.63	-13.41
	2s	-3.15	-5.47	-8.54	-12.17
${}^{90}_{\eta_c}\text{Zr}$	1s	-12.26	-15.35	-19.14	-23.43
	1p	-9.88	-12.86	-16.53	-20.70
	1d	-7.05	-9.87	-13.38	-17.40
	2s	-6.14	-8.87	-12.29	-16.24
	1f	-3.90	-6.50	-9.81	-13.65
${}^{197}_{\eta_c}\text{Au}$	1s	-12.57	-15.59	-19.26	-23.41
	1p	-11.17	-14.14	-17.77	-21.87
	1d	-9.42	-12.31	-15.87	-19.90
	2s	-8.69	-11.53	-15.04	-19.02
	1f	-7.39	-10.19	-13.70	-17.61
${}^{208}_{\eta_c}\text{Pb}$	1s	-12.99	-16.09	-19.82	-24.12
	1p	-11.60	-14.64	-18.37	-22.59
	1d	-9.86	-12.83	-16.49	-20.63
	2s	-9.16	-12.09	-15.70	-19.80
	1f	-7.85	-10.74	-14.30	-18.37

**Table 5.**  $J/\psi$ -nucleus bound state energies taking into account the change in the self-energy in medium, calculated with the Schrödinger equation. All dimensioned quantities are given in MeV.

		Bound state energies				
		$\Lambda_D = 2000$	$\Lambda_D = 3000$	$\Lambda_D = 4000$	$\Lambda_D = 5000$	$\Lambda_D = 6000$
$^4_{J/\psi}\text{He}$	1s	n	n	-0.70	-2.70	-5.51
$^{12}_{J/\psi}\text{C}$	1s	-0.52	-1.98	-4.47	-7.67	-11.26
	1p	n	n	n	-1.38	-3.84
$^{16}_{J/\psi}\text{O}$	1s	-1.03	-2.87	-5.72	-9.24	-13.09
	1p	n	n	-0.94	-3.48	-6.60
$^{40}_{J/\psi}\text{Ca}$	1s	-2.78	-5.44	-9.14	-13.50	-18.12
	1p	-0.38	-2.32	-5.43	-9.32	-13.56
	1d	n	n	-1.52	-4.74	-8.49
	2s	n	n	-1.27	-4.09	-7.60
$^{48}_{J/\psi}\text{Ca}$	1s	-2.96	-5.62	-9.28	-13.55	-18.08
	1p	-0.73	-2.83	-6.03	-9.95	-14.18
	1d	n	n	-2.46	-5.87	-9.73
	2s	n	-0.07	-1.90	-5.00	-8.65
$^{90}_{J/\psi}\text{Zr}$	1s	-3.64	-6.40	-10.12	-14.41	-18.92
	1p	-1.93	-4.42	-7.92	-12.03	-16.40
	1d	-0.03	-2.13	-5.31	-9.18	-13.37
	2s	-0.02	-1.56	-4.51	-8.26	-12.37
	2p	n	n	-1.52	-4.71	-8.45
$^{208}_{J/\psi}\text{Pb}$	1s	-4.25	-7.08	-10.82	-15.11	-19.60
	1p	-3.16	-5.86	-9.52	-13.74	-18.18
	1d	-1.84	-4.38	-7.90	-12.01	-16.37
	2s	-1.41	-3.81	-7.25	-11.30	-15.61
	2p	-0.07	-1.95	-5.10	-8.97	-13.14

and  $\eta'$ -mesic nuclei of mass number  $A$ , obtained by solving the Klein-Gordon equation, for some values of the strength of the imaginary part of the potential  $\gamma = 0.25, 0.5, 1.0$ .

Considering only the ground states, adding and absorptive part of the potential changes the situation appreciably, where the effects are larger the larger  $\gamma$  is. Clearly, the imaginary part of the potential is repulsive, being more repulsive for  $\gamma = 1$ . Whether or not the bound states can be observed experimentally is sensitive to the value of the parameter  $\gamma$ , since  $\Gamma$  increases with increasing  $\gamma$ . Furthermore, because the so-called dispersive effect of the absorptive potential is repulsive, the binding energies for all nuclei decrease with  $\gamma$ . However, they decrease very little. Even for the largest value of  $\gamma$ , there is at least one bound state. We have found similar results for the  $\phi$  meson in our past work [101]. Note that, the width of the ground state increases with  $\gamma$  for all nuclei, as expected, since a larger  $\gamma$  means that the strength of the imaginary part of the potential is larger.

Finally, in Tables 12 and 13 we present the  $B_c^\pm$ -nucleus bound state energies for several nuclei restricting to the 1s and 1p states, where we certainly expect more shallower bound states. (More detailed results will be presented elsewhere in the near future.) For details of the momentum space and the Coulomb potential treatment focusing on the  $^{12}_{B_c}\text{C}$  case, see Ref. [115]. From Tables 12 and 13 we conclude that the  $B_c^\pm$  are expected to form bound states with all the nuclei studied.

## 7. Summary and Conclusions

We have computed the mass shift amount  $\Delta m_h \equiv m_h^* - m_h$  with being  $m_h$  the meson mass in vacuum and  $m_h^*$  that in nuclear medium, of the mesons  $h = \eta, \eta', \phi, \eta_c, J/\psi, \eta_b, \Upsilon$ , and  $B_c^\pm$ , in symmetric nuclear matter and nuclei. For this, we have used two approaches,

**Table 6.** Y-nucleus bound state energies obtained by the Woods-Saxon Fourier transform for several nuclei  $A$ . All dimensioned quantities are in MeV.

$n\ell$	Bound state energies					
	$\Lambda_B = 2000$	$\Lambda_B = 3000$	$\Lambda_B = 4000$	$\Lambda_B = 5000$	$\Lambda_B = 6000$	
${}^4_Y\text{He}$ 1s	-5.6	-6.4	-7.5	-9.0	-10.8	
${}^{12}_Y\text{C}$ 1s	-10.6	-11.6	-12.8	-14.4	-16.3	
1p	-6.1	-6.8	-7.9	-9.3	-10.9	
1d	-1.5	-2.1	-2.9	-4.0	-5.4	
2s	-1.6	-2.1	-2.8	-3.8	-5.1	
${}^{16}_Y\text{O}$ 1s	-11.9	-12.9	-14.2	-15.8	-17.8	
1p	-8.3	-9.2	-10.4	-11.9	-13.7	
1d	-4.4	-5.1	-6.2	-7.5	-9.2	
2s	-3.7	-4.4	-5.4	-6.7	-8.3	
1f	n	-0.9	-1.8	-2.9	-4.3	
${}^{40}_Y\text{Ca}$ 1s	-15.5	-16.6	-18.2	-20.0	-22.3	
1p	-13.3	-14.4	-15.9	-17.7	-19.8	
1d	-10.8	-11.9	-13.3	-15.0	-17.1	
2s	-10.3	-11.3	-12.7	-14.4	-16.4	
1f	-8.1	-9.1	-10.4	-12.1	-14.0	
${}^{48}_Y\text{Ca}$ 1s	-15.3	-16.4	-17.9	-19.7	-21.8	
1p	-13.5	-14.6	-16.0	-17.8	-19.9	
1d	-11.4	-12.4	-13.8	-15.6	-17.6	
2s	-10.8	-11.8	-13.2	-14.9	-16.9	
1f	-9.1	-10.1	-11.4	-13.1	-15.0	
${}^{90}_Y\text{Zr}$ 1s	-15.5	-16.6	-18.1	-19.9	-22.0	
1p	-14.5	-15.5	-17.0	-18.8	-20.9	
1d	-13.2	-14.2	-15.7	-17.4	-19.5	
2s	-12.7	-13.8	-15.2	-16.9	-19.0	
1f	-11.7	-12.7	-14.1	-15.9	-17.9	
${}^{197}_Y\text{Au}$ 1s	-15.3	-16.3	-17.7	-19.4	-21.5	
1p	-14.7	-15.8	-17.2	-18.9	-20.9	
1d	-14.0	-15.0	-16.4	-18.1	-20.1	
2s	-13.7	-14.7	-16.0	-17.8	-19.8	
1f	-13.2	-14.2	-15.6	-17.3	-19.3	
${}^{208}_Y\text{Pb}$ 1s	-15.7	-16.8	-18.2	-20.0	-22.1	
1p	-15.2	-16.2	-17.7	-19.4	-21.5	
1d	-14.5	-15.5	-16.9	-18.7	-20.8	
2s	-14.1	-15.2	-16.6	-18.3	-20.4	
1f	-13.6	-14.7	-16.1	-17.8	-19.9	

namely the quark-meson coupling model, and an hybrid approach that combines the quark-meson coupling model with an effective Lagrangian, for some meson in this study.

We found in all cases that the mass shift amount (Lorentz scalar potential) is negative, which means that the nuclear medium provides attraction to these mesons (these mesons do not acquire any repulsive vector potentials) and opens the possibility of their binding to nuclei. Even though the precise values for the negative mass shifts reported in this work are based on the quark-meson coupling model and effective lagrangians approach, negative mass shifts have also been observed in other approaches and experimental results. Thus, we believe this is a robust prediction of our approach. Using the baryon density distributions of several nuclei calculated in the quark-meson coupling model except for  ${}^4\text{He}$  nucleus (taken from Ref. [117]), and the mass shift amount computed previously, we have calculated the meson-nucleus potentials in a local density approximation for these mesons in nuclei in a wide range of nuclear masses, namely  $A = {}^4\text{He}$ ,  ${}^{12}\text{C}$ ,  ${}^{16}\text{O}$ ,  ${}^{40}\text{Ca}$ ,  ${}^{48}\text{Ca}$ ,  ${}^{90}\text{Zr}$ ,  ${}^{197}\text{Au}$ , and  ${}^{208}\text{Pb}$ . In all the nucleus cases selected for each meson, the resulting nuclear potentials have turned out to be attractive, reflecting the characteristics of the mass shift in the nuclear medium.

Finally, we have solved the Schrödinger or Klein-Gordon equation with the calculated nuclear potentials to obtain the meson-nucleus bound state energies, and widths when the nuclear potential is complex. Although the details differ for each meson, we have found that all the mesons studied are expected to form bound states with nuclei. For the



**Table 7.** Y-nucleus bound state energies obtained by the Direct Bessel transform for several nuclei  $A$ . All dimensioned quantities are in MeV.

		Bound state energies (MeV)		
		Direct Bessel transform		
	$n\ell$	$\Lambda_B = 2000$	$\Lambda_B = 4000$	$\Lambda_B = 6000$
${}^4_Y\text{He}$	1s	-5.93	-6.25	-6.56
${}^{12}_Y\text{C}$	1s	-13.22	-15.26	-18.41
	1p	-8.30	-9.57	-11.51
${}^{16}_Y\text{O}$	1s	-14.30	-16.57	-20.06
	1p	-10.81	-12.37	-14.73
${}^{40}_Y\text{Ca}$	1s	-18.17	-21.63	-23.16
	1p	-15.22	-18.11	-19.58
${}^{48}_Y\text{Ca}$	1s	-16.74	-19.33	-23.20
	1p	-15.36	-17.76	-21.53
${}^{90}_Y\text{Zr}$	1s	-15.87	-18.24	-21.89
	1p	-12.52	-14.78	-18.32
${}^{208}_Y\text{Pb}$	1s	-15.95	-18.41	-22.23
	1p	-13.23	-15.49	-19.91

nuclear potential is complex, the signal for the formation of the meson-nucleus bound state might be difficult to identify experimentally, depending on the obtained bound state energy imaginary part.

**Author Contributions:** All authors have contributed equally, read the manuscript, and agreed to the published version of the manuscript.

**Data Availability Statement:**

The data are available upon the agreement between the requested party and the authors.

**Acknowledgments:** J.J.C.M acknowledges financial support from Universidad de Sonora under grant USO315009105. G.N.Z. was supported by the Coordenação de Aperfeiçoamento de Pessoal de Nível Superior- Brazil (CAPES), FAPESP Process No. 2023/073-3-6, and Instituto Nacional de Ciência e Tecnologia - Nuclear Physics and Applications (INCT-FNA), Brazil, Process No. 464898/2014-5. The work of K.T. was supported by Conselho Nacional de Desenvolvimento Científico e Tecnológico (CNPq, Brazil), Processes No. 304199/2022-2, and FAPESP No. 2023/07313-6, and his work was also part of the projects, Instituto Nacional de Ciência e Tecnologia - Nuclear Physics and Applications (INCT-FNA), Brazil, Process No. 464898/2014-5.

**Conflicts of Interest:** The authors declare no conflicts of interest.

## Abbreviations

The following abbreviations are used in this manuscript:

MDPI	Multidisciplinary Digital Publishing Institute
DOAJ	Directory of open access journals
TLA	Three letter acronym
LD	Linear dichroism

## Appendix A Wave functions

The results for the  $B_c^\pm$ -nucleus system wave functions, for different cutoff values, are presented in Figs. A1 to A6. The wave functions for the Y- and  $\eta_b$ -nucleus systems, for different methods of partial wave decomposition and cutoff values, are also presented in Figs. A7 to A20.

The wave functions obtained when using the Bessel transform of the original potential and the decomposition of the Fourier transform of the fitted Woods-Saxon potential produce different shapes of wave function distributions at various energy levels. These treatments give slight dependence of the bound-state energies on the method used to obtain the partial-wave decomposition of the momentum space potential. For the future possible

**Table 8.**  $\eta_b$ -nucleus bound state energies obtained by the Woods-Saxon Fourier transform for several nuclei  $A$ . All dimensioned quantities are in MeV.

		Bound state energies				
	$n\ell$	$\Lambda_B = 2000$	$\Lambda_B = 3000$	$\Lambda_B = 4000$	$\Lambda_B = 5000$	$\Lambda_B = 6000$
${}^4_{\eta_b}\text{He}$	1s	-63.1	-64.7	-66.7	-69.0	-71.5
	1p	-40.6	-42.0	-43.7	-45.8	-48.0
	1d	-17.2	-18.3	-19.7	-21.4	-23.2
	2s	-15.6	-16.6	-17.9	-19.4	-21.1
${}^{12}_{\eta_b}\text{C}$	1s	-65.8	-67.2	-69.0	-71.1	-73.4
	1p	-57.0	-58.4	-60.1	-62.1	-64.3
	1d	-47.5	-48.8	-50.4	-52.3	-54.4
	2s	-46.3	-47.5	-49.1	-51.0	-53.0
	1f	-37.5	-38.7	-40.2	-42.0	-43.9
${}^{16}_{\eta_b}\text{O}$	1s	-67.8	-69.2	-71.0	-73.1	-75.4
	1p	-61.8	-63.2	-64.9	-67.0	-69.2
	1d	-54.9	-56.2	-57.9	-59.9	-62.0
	2s	-53.2	-54.6	-56.3	-58.2	-60.3
	1f	-47.3	-48.6	-50.2	-52.1	-54.2
${}^{40}_{\eta_b}\text{Ca}$	1s	-79.0	-80.6	-82.6	-85.0	-87.5
	1p	-75.4	-77.0	-79.0	-81.4	-83.9
	1d	-71.4	-73.0	-74.9	-77.2	-79.7
	2s	-70.5	-72.0	-74.0	-76.3	-78.8
	1f	-67.0	-68.5	-70.4	-72.7	-75.1
${}^{48}_{\eta_b}\text{Ca}$	1s	-76.7	-78.2	-80.2	-82.5	-85.0
	1p	-74.0	-75.5	-77.4	-79.7	-82.1
	1d	-70.8	-72.3	-74.2	-76.4	-78.8
	2s	-69.9	-71.4	-73.3	-75.5	-77.9
	1f	-67.2	-68.6	-70.6	-72.8	-75.1
${}^{90}_{\eta_b}\text{Zr}$	1s	-75.5	-77.0	-78.9	-81.1	-83.5
	1p	-74.1	-75.6	-77.5	-79.7	-82.1
	1d	-72.3	-73.8	-75.7	-77.9	-80.2
	2s	-71.6	-73.0	-74.9	-77.1	-79.5
	1f	-70.2	-71.7	-73.6	-75.8	-78.1
${}^{197}_{\eta_b}\text{Au}$	1s	-72.8	-74.2	-76.1	-78.2	-80.5
	1p	-72.3	-73.7	-75.6	-77.7	-80.0
	1d	-71.3	-72.8	-74.6	-76.7	-79.0
	2s	-70.7	-72.1	-74.0	-76.1	-78.4
	1f	-70.2	-71.7	-73.5	-75.6	-77.9
${}^{208}_{\eta_b}\text{Pb}$	1s	-74.7	-76.2	-78.1	-80.3	-82.6
	1p	-74.2	-75.7	-77.5	-79.7	-82.1
	1d	-73.2	-74.7	-76.6	-78.8	-81.1
	2s	-72.7	-74.1	-76.0	-78.2	-80.5
	1f	-72.1	-73.6	-75.5	-77.6	-80.0

improvements of the treatments, and so that one can compare with different treatments, we present all the wave functions obtained for the two different methods. These will be very useful in the future. However, we believe that the difference originated from the numerical procedure and treatments, the difference will not change our main conclusions, especially in connection with the accuracy required and achieved associated with the strong interaction experimental measurement.

**Table 9.**  ${}^4_{\eta_b}A$  bound state energies obtained by the Direct Bessel transform for several nuclei  $A$ . All dimensioned quantities are in MeV.

		Bound state energies (MeV)		
		Direct Bessel transform		
	$n\ell$	$\Lambda_B = 2000$	$\Lambda_B = 4000$	$\Lambda_B = 6000$
${}^4_{\eta_b}\text{He}$	1s	-68.71	-71.59	-75.44
	1p	-39.97	-41.50	-43.54
	1d	-37.73	-39.56	-42.03
	2s	-29.14	-30.09	-31.38
${}^{12}_{\eta_b}\text{C}$	1s	-63.70	-66.93	-70.27
	1p	-53.17	-55.13	-59.38
	1d	-46.47	-48.50	-51.17
	2s	-34.53	-36.30	-39.43
${}^{16}_{\eta_b}\text{O}$	1s	-68.37	-71.25	-75.14
	1p	-57.02	-59.58	-63.02
	1d	-47.05	-49.37	-52.50
	2s	-23.18	-25.50	-28.69
${}^{40}_{\eta_b}\text{Ca}$	1s	-79.11	-82.59	-87.27
	1p	-70.60	-73.86	-78.26
	1d	-53.31	-55.99	-59.61
	2s	-48.35	-51.31	-55.32
${}^{48}_{\eta_b}\text{Ca}$	1s	-63.94	-66.88	-70.83
	1p	-58.60	-61.10	-64.43
	1d	-34.04	-36.40	-39.60
	2s	-26.35	-28.30	-30.95
${}^{90}_{\eta_b}\text{Zr}$	1s	-71.32	-74.52	-78.85
	1p	-63.78	-67.03	-71.42
	1d	-57.78	-60.82	-64.93
	2s	-51.53	-54.07	-57.46
${}^{208}_{\eta_b}\text{Pb}$	1s	-61.44	-64.25	-68.02
	1p	-59.82	-62.95	-67.18
	1d	-51.36	-54.05	-57.65
	2s	-48.71	-51.25	-54.66

**Table 10.** Bound state energies ( $E$ ) and full widths ( $\Gamma$ ) of  $\eta$  meson in nucleus of mass number  $A$  obtained by solving the Klein-Gordon equation for various values of the parameter  $\gamma$ .

	$n\ell$	$\gamma = 0$		$\gamma = 0.25$		$\gamma = 0.5$		$\gamma = 1.0$	
		$E$	$\Gamma$	$E$	$\Gamma$	$E$	$\Gamma$	$E$	$\Gamma$
${}^4_\eta\text{He}$	1s	-10.99	0	-10.79	8.21	-10.20	16.65	-8.13	34.94
${}^{12}_\eta\text{C}$	1s	-25.25	0	-25.16	10.86	-24.91	21.82	-24.02	44.29
	1p	-0.87	0	-0.43	4.97	N	N	N	N
${}^{16}_\eta\text{O}$	1s	-30.78	0	-30.72	12.00	-30.53	24.07	-29.86	48.67
	1p	-6.47	0	-6.26	7.84	-5.67	15.99	-3.77	33.80
${}^{40}_\eta\text{Ca}$	1s	-46.93	0	-46.89	15.12	-46.79	30.28	-46.43	60.87
	1p	-26.93	0	-26.85	12.67	-26.61	25.44	-25.77	51.59
	1d	-6.67	0	-6.47	9.48	-5.91	19.27	-4.15	40.31
	2s	-5.43	0	-5.09	7.51	-4.18	15.59	N	N
${}^{48}_\eta\text{Ca}$	1s	-47.78	0	-47.75	14.98	-47.66	30.00	-47.38	60.25
	1p	-29.97	0	-29.90	12.99	-29.71	26.06	-29.04	52.71
	1d	-11.08	0	-10.93	10.45	-10.51	21.10	-9.15	43.52
	2s	-8.7	0	-8.11	8.83	-7.42	18.06	N	N
${}^{90}_\eta\text{Zr}$	1s	-52.56	0	-52.54	15.34	-52.50	30.71	-52.34	61.56
	1p	-39.85	0	-39.81	14.17	-39.71	28.40	-39.36	57.11
	1d	-25.32	0	-25.25	12.74	-25.06	25.57	-24.40	51.75
	2s	-21.04	0	-20.94	11.95	-20.65	24.04	-19.70	49.03
${}^{197}_\eta\text{Au}$	1s	-55.12	0	-55.11	15.20	-55.09	30.41	-55.01	60.89
	1p	-47.13	0	-47.11	14.58	-47.06	29.19	-46.90	58.53
	1d	-37.60	0	-37.58	13.83	-37.49	27.69	-37.20	55.67
	2s	-34.01	0	-33.97	13.45	-33.86	26.96	-33.47	54.31
${}^{208}_\eta\text{Pb}$	1s	-56.85	0	-56.84	15.61	-56.82	31.24	-56.75	62.55
	1p	-48.92	0	-48.90	14.99	-48.86	30.01	-48.70	60.17
	1d	-39.81	0	-39.45	14.24	-39.37	28.51	-39.09	57.29
	2s	-35.95	0	-35.91	13.87	-35.80	27.80	-35.43	55.96

## References

1. A. Accardi, P. Achenbach, D. Adhikari, A. Afanasev, C. S. Akondi, N. Akopov, M. Albaladejo, H. Albataineh, M. Albrecht and B. Almeida-Zamora, *et al.* Eur. Phys. J. A **60**, 173 (2024) [arXiv:2306.09360 [nucl-ex]].
2. S. J. Brodsky, A. L. Deshpande, H. Gao, R. D. McKeown, C. A. Meyer, Z. E. Meziani, R. G. Milner, J. Qiu, D. G. Richards and C. D. Roberts, [arXiv:1502.05728 [hep-ph]].
3. U. Heinz, P. Sorensen, A. Deshpande, C. Gagliardi, F. Karsch, T. Lappi, Z. E. Meziani, R. Milner, B. Muller and J. Nagle, *et al.* [arXiv:1501.06477 [nucl-th]].
4. R. Alkofer and L. von Smekal, Phys. Rept. **353**, 281 (2001), [arXiv:hep-ph/0007355 [hep-ph]].
5. N. Brambilla, S. Eidelman, P. Foka, S. Gardner, A. S. Kronfeld, M. G. Alford, R. Alkofer, M. Butenschoen, T. D. Cohen and J. Erdmenger, *et al.* Eur. Phys. J. C **74**, 2981 (2014), [arXiv:1404.3723 [hep-ph]].
6. A. Bashir, L. Chang, I. C. Cloet, B. El-Bennich, Y. X. Liu, C. D. Roberts and P. C. Tandy, Commun. Theor. Phys. **58**, 79 (2012), [arXiv:1201.3366 [nucl-th]].
7. I. C. Cloet and C. D. Roberts, Prog. Part. Nucl. Phys. **77**, 1 (2014), [arXiv:1310.2651 [nucl-th]].
8. A. Hosaka, T. Hyodo, K. Sudoh, Y. Yamaguchi and S. Yasui, Prog. Part. Nucl. Phys. **96**, 88 (2017), [arXiv:1606.08685 [hep-ph]].
9. G. Krein, AIP Conf. Proc. **1701**, 020012 (2016).
10. V. Metag, M. Nanova and E. Y. Paryev, Prog. Part. Nucl. Phys. **97**, 199 (2017), [arXiv:1706.09654 [nucl-ex]].
11. G. Krein, A. W. Thomas and K. Tsushima, Prog. Part. Nucl. Phys. **100**, 161 (2018), [arXiv:1706.02688 [hep-ph]].
12. T. Hatsuda and T. Kunihiro, Phys. Rept. **247**, 221-367 (1994), [arXiv:hep-ph/9401310 [hep-ph]].
13. S. Leupold, V. Metag and U. Mosel, Int. J. Mod. Phys. E **19**, 147-224 (2010), [arXiv:0907.2388 [nucl-th]].
14. R. S. Hayano and T. Hatsuda, Rev. Mod. Phys. **82**, 2949 (2010), [arXiv:0812.1702 [nucl-ex]].
15. T. Nishi *et al.* [piAF], Nature Phys. **19**, 788 (2023), [arXiv:2204.05568 [nucl-ex]].
16. M. Schroedter, R. L. Thews, and J. Rafelski, Phys. Rev. C **62**, 024905 (2000), [arXiv:hep-ph/0004041 [hep-ph]].
17. A. Andronic, F. Arleo, R. Arnaldi, A. Beraudo, E. Bruna, D. Caffarri, Z. C. del Valle, J. G. Contreras, T. Dahms, A. Dainese *et al.*, Eur. Phys. J. C **76**, 107 (2016), [arXiv:1506.03981 [nucl-ex]].
18. Y. S. Li and X. Liu, Phys. Rev. D **108**, 093005 (2023), [arXiv:2309.08191 [hep-ph]].
19. C. Bird, P. Jackson, R. V. Kowalewski and M. Pospelov, Phys. Rev. Lett. **93**, 201803 (2004), [arXiv:hep-ph/0401195 [hep-ph]].
20. W. Altmannshofer and D. M. Straub, Eur. Phys. J. C **75**, 382 (2015), [arXiv:1411.3161 [hep-ph]].
21. A. J. Buras, J. Girrbach-Noe, C. Niehoff and D. M. Straub, JHEP **02**, 184 (2015), [arXiv:1409.4557 [hep-ph]].

**Table 11.** Bound state energies ( $E$ ) and full widths ( $\Gamma$ ) of  $\eta'$  meson in nucleus of mass number  $A$  obtained by solving the Klein-Gordon equation for various values of the parameter  $\gamma$ .

	$n\ell$	$\gamma = 0$		$\gamma = 0.25$		$\gamma = 0.5$		$\gamma = 1.0$	
		$E$	$\Gamma$	$E$	$\Gamma$	$E$	$\Gamma$	$E$	$\Gamma$
${}^4_{\eta'}\text{He}$	1s	-22.11	0	-21.96	11.37	-21.55	22.89	-20.06	46.83
${}^{12}_{\eta'}\text{C}$	1s	-33.88	0	-33.82	12.30	-33.64	24.66	-33.00	49.73
	1p	-12.72	0	-12.57	9.06	-12.15	18.29	-10.67	37.68
${}^{16}_{\eta'}\text{O}$	1s	-38.64	0	-38.59	13.06	-38.46	26.17	-38.00	52.65
	1p	-19.75	0	-19.65	10.76	-19.34	21.64	-18.28	44.07
	2s	-1.39	0	-0.84	4.48	N	N	N	N
	1d	-0.33	0	-0.69	7.20	N	N	N	N
${}^{40}_{\eta'}\text{Ca}$	1s	-52.38	0	-52.35	15.59	-52.28	31.22	-52.00	62.61
	1p	-38.41	0	-38.35	14.18	-38.19	28.41	-37.63	57.22
	1d	-23.12	0	-23.02	12.46	-22.74	25.03	-21.75	50.81
	2s	-20.38	0	-20.25	11.72	-19.87	23.60	-18.58	48.25
${}^{48}_{\eta'}\text{Ca}$	1s	-52.40	0	-52.38	15.29	-52.32	30.60	-52.11	61.35
	1p	-40.30	0	-40.26	14.18	-40.13	28.40	-39.68	57.12
	1d	-26.68	0	-26.59	12.82	-26.37	25.72	-25.58	52.02
	2s	-23.45	0	-23.34	12.19	-23.04	24.51	-22.01	49.85
${}^{90}_{\eta'}\text{Zr}$	1s	-55.20	0	-55.19	15.31	-55.16	30.63	-55.04	61.35
	1p	-47.05	0	-47.02	14.70	-46.96	29.43	-46.72	59.04
	1d	-37.42	0	-37.38	13.96	-37.27	27.96	-36.86	56.22
	2s	-34.19	0	-34.14	13.61	-33.99	27.29	-33.47	54.98
${}^{197}_{\eta'}\text{Au}$	1s	-56.03	0	-56.03	14.94	-56.01	29.89	-55.96	59.83
	1p	-51.12	0	-51.10	14.64	-51.07	29.30	-50.96	58.67
	1d	-45.15	0	-45.14	14.27	-45.08	28.56	-44.89	57.26
	2s	-42.80	0	-42.78	14.10	-42.71	28.22	-42.47	56.63
${}^{208}_{\eta'}\text{Pb}$	1s	-57.65	0	-57.64	15.34	-57.63	30.68	-57.57	61.40
	1p	-52.77	0	-52.76	15.03	-52.73	30.07	-52.62	60.23
	1d	-46.87	0	-46.85	14.66	-46.80	29.33	-46.61	58.80
	2s	-44.56	0	-44.54	14.49	-44.47	29.00	-44.24	58.19

**Table 12.** Bound state energies of  $B_c^-$  in nucleus of mass number  $A$ , obtained by the Direct Bessel transform method. All dimensioned quantities are in MeV.

		Bound state energies (MeV)		
		Direct Bessel transform		
	$n\ell$	$\Lambda_B = 2000$	$\Lambda_B = 4000$	$\Lambda_B = 6000$
${}^{12}_{B_c^-}\text{C}$	1s	-79.12	-80.63	-87.03
	1p	-56.15	-57.53	-63.38
${}^{16}_{B_c^-}\text{O}$	1s	-75.00	-76.16	-80.94
	1p	-54.86	-56.13	-61.55
${}^{40}_{B_c^-}\text{Ca}$	1s	-104.27	-105.69	-111.87
	1p	-81.71	-83.51	-91.34
${}^{48}_{B_c^-}\text{Ca}$	1s	-96.63	-98.37	-105.81
	1p	-72.02	-73.56	-80.24
${}^{90}_{B_c^-}\text{Zr}$	1s	-96.34	-98.32	-106.82
	1p	-83.82	-85.44	-92.35
${}^{208}_{B_c^-}\text{Pb}$	1s	-95.88	-97.39	-103.79
	1p	-70.46	-71.76	-77.34

22. S. Descotes-Genon, L. Hofer, J. Matias and J. Virto, JHEP **06**, 092 (2016), [arXiv:1510.04239 [hep-ph]].
23. R. Dutta and A. Bhol, Phys. Rev. D **96**, 076001 (2017), [arXiv:1701.08598 [hep-ph]].
24. A. Tumasyan *et al.* [CMS], Phys. Rev. Lett. **129**, 032001 (2022), [arXiv:2111.02219 [hep-ex]].

**Table 13.** Bound state energies of  $B_c^+$  in nucleus of mass number  $A$ , obtained by the Direct Bessel transform method. All dimensioned quantities are in MeV.

		Bound state energies (MeV)		
		Direct Bessel transform		
	$n\ell$	$\Lambda_B = 2000$	$\Lambda_B = 4000$	$\Lambda_B = 6000$
$^{12}_{B_c^+}\text{C}$	1s	-71.01	-72.53	-78.94
	1p	-49.11	-50.49	-56.32
$^{16}_{B_c^+}\text{O}$	1s	-64.64	-65.80	-70.59
	1p	-45.94	-47.22	-52.64
$^{40}_{B_c^+}\text{Ca}$	1s	-84.89	-86.31	-92.49
	1p	-62.80	-64.57	-72.23
$^{48}_{B_c^+}\text{Ca}$	1s	-77.09	-78.83	-86.26
	1p	-53.64	-55.13	-61.60
$^{90}_{B_c^+}\text{Zr}$	1s	-65.51	-67.49	-75.99
	1p	-55.11	-56.75	-63.75
$^{208}_{B_c^+}\text{Pb}$	1s	-48.61	-50.13	-56.53
	1p	-29.27	-30.58	-36.22

25. F. Akram, "Hadronic Cross Sections of  $B_c$  Mesons," PhD Punjab U. (2013).
26. M. A. K. Lodhi and R. Marshall, Nucl. Phys. A **790**, 323 (2007),
27. M. A. K. Lodhi, F. Akram and S. Irfan, Phys. Rev. C **84**, 034901 (2011), [arXiv:1309.2912 [nucl-th]].
28. B. Wu, Z. Tang, M. He and R. Rapp, Phys. Rev. C **109**, 014906 (2024), [arXiv:2302.11511 [nucl-th]].
29. A. Tumasyan *et al.* [CMS], Phys. Rev. Lett. **128**, 252301 (2022), [arXiv:2201.02659 [hep-ex]].
30. J. W. Harris and B. Müller, [arXiv:2308.05743 [hep-ph]].
31. Z. w. Lin and C. M. Ko, Phys. Lett. B **503**, 104 (2001), [arXiv:nucl-th/0007027 [nucl-th]].
32. A. M. Sirunyan *et al.* [CMS], Phys. Lett. B **790**, 270 (2019), [arXiv:1805.09215 [hep-ex]].
33. G. Aad *et al.* [ATLAS], Phys. Rev. C **107**, 054912 (2023), [arXiv:2205.03042 [nucl-ex]].
34. B. Aboona *et al.* [STAR], Phys. Rev. Lett. **130**, 112301 (2023), [arXiv:2207.06568 [nucl-ex]].
35. P. A. M. Guichon, Phys. Lett. B **200**, 235 (1988).
36. S. J. Brodsky and G. A. Miller, Phys. Lett. B **412**, 125 (1997), [arXiv:hep-ph/9707382 [hep-ph]].
37. G. Krein, A. W. Thomas and K. Tsushima, Phys. Lett. B **697**, 136 (2011), [arXiv:1007.2220 [nucl-th]].
38. K. Tsushima, D. H. Lu, G. Krein and A. W. Thomas, Phys. Rev. C **83**, 065208 (2011), [arXiv:1103.5516 [nucl-th]].
39. C. M. Ko, P. Levai, X. J. Qiu and C. T. Li, Phys. Rev. C **45**, 1400 (1992).
40. M. Asakawa, C. M. Ko, P. Levai and X. J. Qiu, Phys. Rev. C **46**, R1159 (1992).
41. E. Friedman and G. Soff, J. Phys. G **11**, L37 (1985).
42. Yamazaki, T., Hayano, R.S., Itahashi, K. et al., Z. Physik A **355**, 219 (1996).
43. J. D. Davies, G. J. Pyle, G. T. A. Squier, C. J. Batty, S. F. Biagi, S. D. Hoath, P. Sharman and A. S. Clough, Phys. Lett. B **83**, 55 (1979).
44. C. H. Lee, G. E. Brown, D. P. Min and M. Rho, Nucl. Phys. A **585**, 401 (1995), [arXiv:hep-ph/9406311 [hep-ph]].
45. T. M. Ito, R. S. Hayano, S. N. Nakamura, T. P. Terada, M. Iwasaki, D. R. Gill, L. Lee, A. Olin, M. Salomon and S. Yen, *et al.* Phys. Rev. C **58**, 2366 (1998).
46. C. Curceanu, C. Guaraldo, M. Iliescu, M. Cargnelli, R. Hayano, J. Marton, J. Zmeskal, T. Ishiwatari, M. Iwasaki and S. Okada, *et al.* Rev. Mod. Phys. **91**, 025006 (2019).
47. S. Hirenzaki, Y. Okumura, H. Toki, E. Oset and A. Ramos, Phys. Rev. C **61**, 055205 (2000).
48. R. S. Hayano, S. Hirenzaki and A. Gillitzer, Eur. Phys. J. A **6**, 99 (1999), [arXiv:nucl-th/9806012 [nucl-th]].
49. K. Tsushima, D. H. Lu, A. W. Thomas and K. Saito, Phys. Lett. B **443**, 26 (1998), [arXiv:nucl-th/9806043 [nucl-th]].
50. K. Tsushima, D. H. Lu, A. W. Thomas, K. Saito and R. H. Landau, Phys. Rev. C **59**, 2824 (1999), [arXiv:nucl-th/9810016 [nucl-th]].
51. S. J. Brodsky, I. A. Schmidt and G. F. de Teramond, Phys. Rev. Lett. **64**, 1011 (1990).
52. S. H. Lee and C. M. Ko, Phys. Rev. C **67**, 038202 (2003), [arXiv:nucl-th/0208003 [nucl-th]].
53. G. Krein, J. Phys. Conf. Ser. **422**, 012012 (2013).
54. F. Klingl, S. s. Kim, S. H. Lee, P. Morath and W. Weise, Phys. Rev. Lett. **82** (1999), 3396; **83**, 4224 (1999), [arXiv:nucl-th/9811070 [nucl-th]].
55. A. Hayashigaki, Prog. Theor. Phys. **101** (1999), 923. [arXiv:nucl-th/9811092 [nucl-th]].
56. A. Kumar and A. Mishra, Phys. Rev. C **82**, 045207 (2010), [arXiv:1005.2748 [nucl-th]].

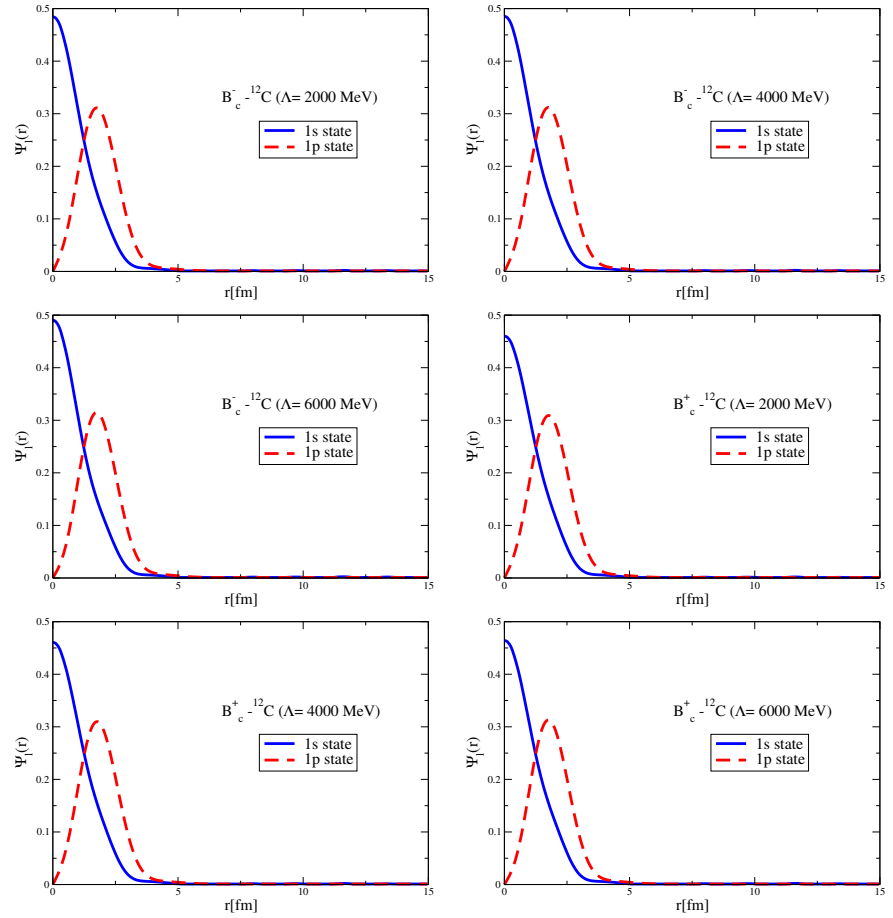


**Figure A1.** Coordinate space wave functions for the 1s and 1p states of the  $B_c^{\pm-12}\text{C}$  systems with the Coulomb potentials for different values of  $\Lambda$ .

57. V. B. Belyaev, N. V. Shevchenko, A. I. Fix and W. Sandhas, Nucl. Phys. A **780**, 100 (2006), [arXiv:nucl-th/0601058 [nucl-th]].
58. A. Yokota, E. Hiyama and M. Oka, PTEP **2013**, 113D01 (2013), [arXiv:1308.6102 [nucl-th]].
59. M. E. Peskin, Nucl. Phys. B **156**, 365 (1979).
60. D. Kharzeev, Proc. Int. Sch. Phys. Fermi **130**, 105 (1996), [arXiv:nucl-th/9601029 [nucl-th]].
61. A. B. Kaidalov and P. E. Volkovitsky, Phys. Rev. Lett. **69**, 3155 (1992).
62. M. E. Luke, A. V. Manohar and M. J. Savage, Phys. Lett. B **288** (1992), 355. [arXiv:hep-ph/9204219 [hep-ph]].
63. G. F. de Teramond, R. Espinoza and M. Ortega-Rodriguez, Phys. Rev. D **58**, 034012 (1998), [arXiv:hep-ph/9708202 [hep-ph]].
64. A. Sibirtsev and M. B. Voloshin, Phys. Rev. D **71**, 076005 (2005), [arXiv:hep-ph/0502068 [hep-ph]].
65. M. B. Voloshin, Prog. Part. Nucl. Phys. **61**, 455 (2008), [arXiv:0711.4556 [hep-ph]].
66. J. Tarrús Castellà and G. Krein, Phys. Rev. D **98**, 014029 (2018), [arXiv:1803.05412 [hep-ph]].
67. J. J. Cobos-Martínez, K. Tsushima, G. Krein and A. W. Thomas, Phys. Lett. B **811**, 135882 (2020), [arXiv:2007.04476 [hep-ph]].
68. K. Yokokawa, S. Sasaki, T. Hatsuda and A. Hayashigaki, Phys. Rev. D **74**, 034504 (2006), [arXiv:hep-lat/0605009 [hep-lat]].
69. T. Kawanai and S. Sasaki, Phys. Rev. D **82**, 091501 (2010), [arXiv:1009.3332 [hep-lat]].
70. U. Skerbis and S. Prelovsek, Phys. Rev. D **99**, 094505 (2019), [arXiv:1811.02285 [hep-lat]].
71. E. Chizzali, Y. Kamiya, R. Del Grande, T. Doi, L. Fabbietti, T. Hatsuda and Y. Lyu, Phys. Lett. B **848**, 138358 (2024), [arXiv:2212.12690 [nucl-ex]].
72. G. N. Zeminiani, J. J. Cobos-Martínez and K. Tsushima, Eur. Phys. J. A **57**, 259 (2021), [arXiv:2012.11381 [hep-ph]].
73. G. N. Zeminiani, [arXiv:2201.09158 [nucl-th]].
74. G. Zeminiani, J. J. Cobos-Martínez and K. Tsushima, PoS PANIC2021, 208 (2022), [arXiv:2109.08636 [hep-ph]].
75. J. J. Cobos-Martínez, G. N. Zeminiani and K. Tsushima, Phys. Rev. C **105**, 025204 (2022), [arXiv:2201.05696 [nucl-th]].
76. J. J. Aubert *et al.* [European Muon], Phys. Lett. B **123**, 275 (1983).
77. For a review, D. F. Geesaman, K. Saito and A. W. Thomas, Ann. Rev. Nucl. Part. Sci. **45**, 337 (1995).
78. S. Dieterich, P. Bartsch, D. Baumann, J. Bermuth, K. Bohinc, R. Bohm, D. Bosnar, S. Derber, M. Ding and M. Distler, *et al.* Phys. Lett. B **500**, 47 (2001), [arXiv:nucl-ex/0011008 [nucl-ex]].
79. S. Strauch (Jefferson Lab E93-049 Collaboration), Eur. Phys. J. A **19**, 153 (2004), S. Strauch *et al.*, Phys. Rev. Lett. **91**, 052301 (2003).



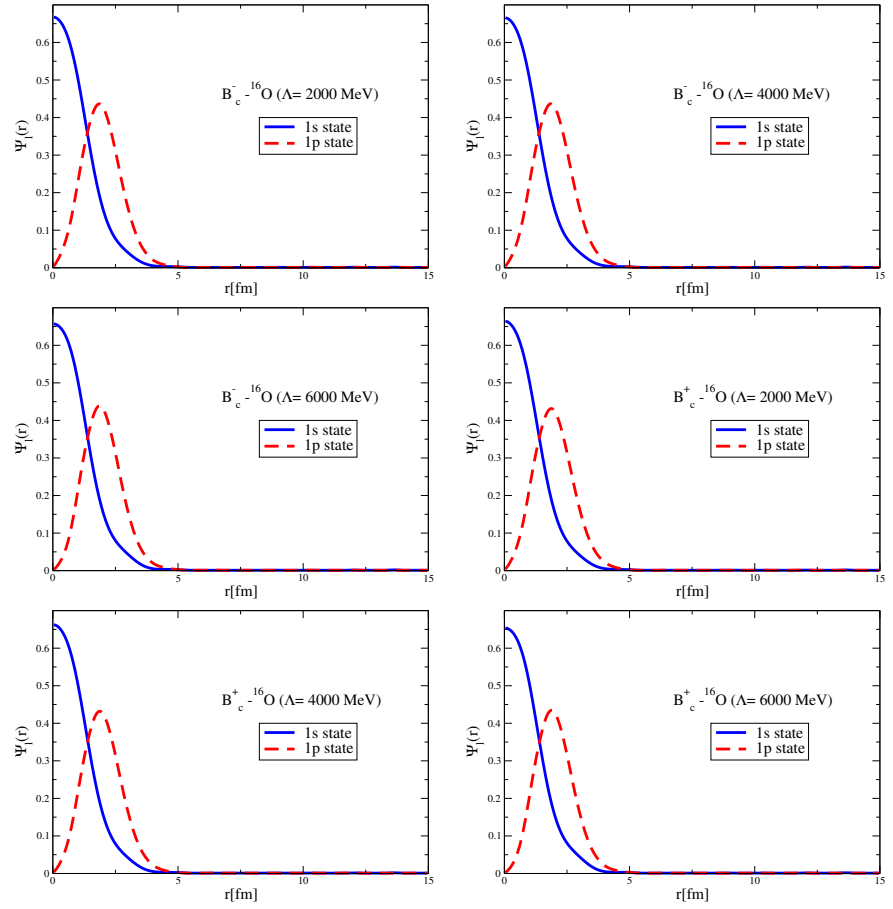


**Figure A2.** Coordinate space wave functions for the 1s and 1p states of the  $B_c^\pm\text{-}^{16}\text{O}$  systems with the Coulomb potentials for different values of  $\Lambda$ .

80. K. Saito, K. Tsushima and A. W. Thomas, *Prog. Part. Nucl. Phys.* **58**, 1 (2007), [arXiv:hep-ph/0506314 [hep-ph]].
81. P. A. M. Guichon, A. W. Thomas and K. Tsushima, *Nucl. Phys. A* **814**, 66 (2008), [arXiv:0712.1925 [nucl-th]].
82. R. Shyam and K. Tsushima, [arXiv:1901.06090 [nucl-th]].
83. P. A. M. Guichon, J. R. Stone and A. W. Thomas, *Prog. Part. Nucl. Phys.* **100**, 262 (2018).
84. G. N. Zeminiani, S. L. P. G. Beres and K. Tsushima, *Phys. Rev. D* **110**, 094045 (2024), [arXiv:2401.00250 [hep-ph]].
85. K. Tsushima, K. Saito, A. W. Thomas and S. V. Wright, *Phys. Lett. B* **429**, 239 (1998), [erratum: *Phys. Lett. B* **436**, 453 (1998)], [arXiv:nucl-th/9712044 [nucl-th]].
86. A. Sibirtsev, K. Tsushima and A. W. Thomas, *Eur. Phys. J. A* **6**, 351 (1999), [nucl-th/9904016].
87. A. Sibirtsev, K. Tsushima, K. Saito and A. W. Thomas, *Phys. Lett. B* **484**, 23 (2000), [nucl-th/9904015].
88. K. Tsushima and F. C. Khanna, *Phys. Lett. B* **552**, 138 (2003), [nucl-th/0207036].
89. P. A. M. Guichon, K. Saito, E. N. Rodionov and A. W. Thomas, *Nucl. Phys. A* **601**, 349 (1996), [arXiv:nucl-th/9509034 [nucl-th]].
90. K. Tsushima, *PTEP* **2022**, 043D02 (2022), [arXiv:2008.03724 [hep-ph]].
91. R. L. Workman *et al.* [Particle Data Group], “Review of Particle Physics,” *PTEP* **2022**, 083C01 (2022).
92. F. Klingl, N. Kaiser and W. Weise, *Z. Phys. A* **356**, 193 (1996), [hep-ph/9607431].
93. M. Tanabashi *et al.* [Particle Data Group], *Phys. Rev. D* **98**, 030001 (2018).
94. S. Okubo, *Phys. Lett.* **5**, 165 (1963), *Phys. Rev. D* **16**, 2336 (1977); G. Zweig, CERN Report No. 8419 TH 412, 1964, (unpublished); J. Iizuka, K. Okada, and O. Shito, *Prog. Theor. Phys.* **35**, 1061 (1966), J. Iizuka, *Prog. Theor. Phys. Suppl.* **37**, 21 (1966).
95. K. Tsushima, D. Lu, G. Krein and A. W. Thomas, *AIP Conf. Proc.* **1354**, 39 (2011), [arXiv:1101.3389 [nucl-th]].
96. Y. Lyu, T. Doi, T. Hatsuda and T. Sugiura, *Phys. Lett. B* **860**, 139178 (2025), [arXiv:2410.22755 [hep-lat]].
97. Y. Lyu, T. Doi, T. Hatsuda and T. Sugiura, [arXiv:2502.00054 [hep-lat]].
98. F. Klingl, N. Kaiser and W. Weise, *Z. Phys. A* **356**, 193 (1996), [hep-ph/9607431].
99. Z. w. Lin, C. M. Ko and B. Zhang, *Phys. Rev. C* **61**, 024904 (2000), [nucl-th/9905003].
100. J. J. Cobos-Martínez, K. Tsushima, G. Krein and A. W. Thomas, *Phys. Lett. B* **771**, 113 (2017), [arXiv:1703.05367 [nucl-th]].
101. J. J. Cobos-Martínez, K. Tsushima, G. Krein and A. W. Thomas, *Phys. Rev. C* **96**, 035201 (2017), [arXiv:1705.06653 [nucl-th]].
102. J. J. Cobos-Martínez, K. Tsushima, G. Krein and A. W. Thomas, *J. Phys. Conf. Ser.* **912**, 012009 (2017), [arXiv:1711.06358 [nucl-th]].
103. J. J. Cobos-Martínez, K. Tsushima, G. Krein and A. W. Thomas, *PoS Hadron2017*, 209 (2018), [arXiv:1711.09895 [nucl-th]].

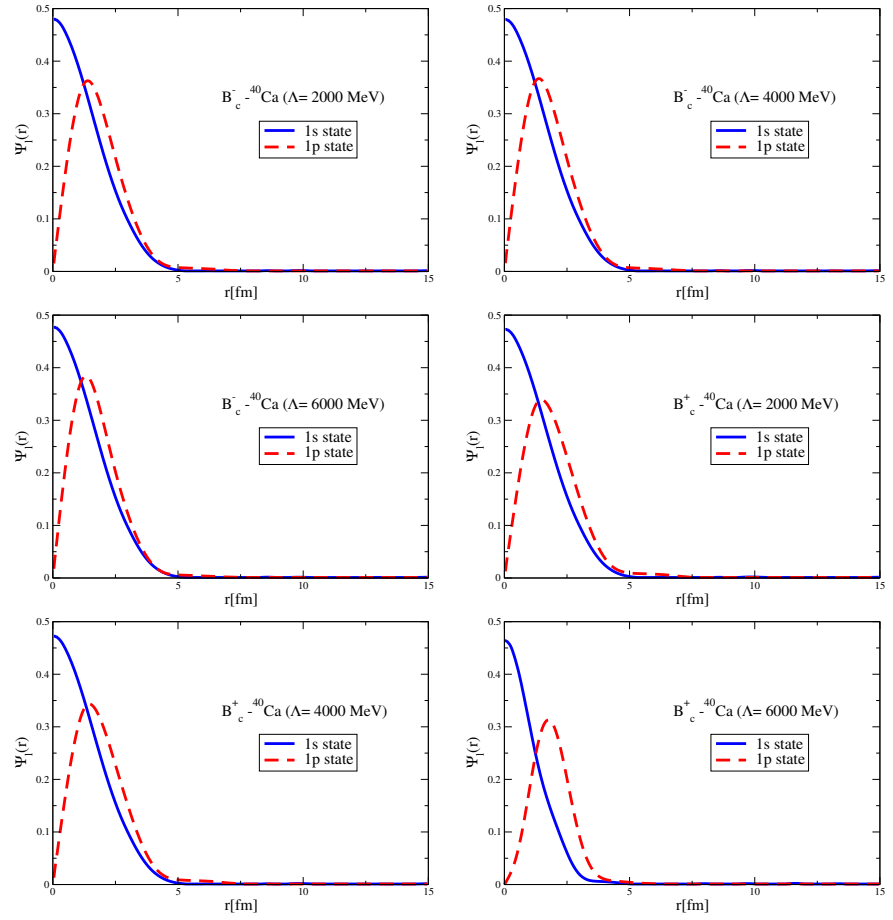


**Figure A3.** Coordinate space wave functions for the 1s and 1p states of the  $B_c^\pm$ - $^{40}\text{Ca}$  systems with the Coulomb potentials for different values of  $\Lambda$ .

104. J. J. Cobos-Martínez, K. Tsushima, G. Krein and A. W. Thomas, JPS Conf. Proc. **26**, 024033 (2019), [arXiv:1901.07404 [hep-ph]].
105. W. Lucha, D. Melikhov, H. Sazdjian and S. Simula, Phys. Rev. D **93**, no. 1, 016004 (2016); Addendum: [Phys. Rev. D **93**, 019902 (2016)], [arXiv:1506.09213 [hep-ph]].
106. Z. w. Lin and C. M. Ko, Phys. Rev. C **62**, 034903 (2000), [nucl-th/9912046].
107. A. Hayashigaki, Phys. Lett. B **487** 96 (2000), [arXiv:nucl-th/0001051 [nucl-th]].
108. K. Azizi, N. Er and H. Sundu, Eur. Phys. J. C **74**, 3012 (2014), [arXiv:1405.3058 [hep-ph]].
109. Z. G. Wang, Phys. Rev. C **92**, 065205 (2015), [arXiv:1501.05093 [hep-ph]].
110. K. Suzuki, P. Gubler and M. Oka, Phys. Rev. C **93**, 045209 (2016), [arXiv:1511.04513 [hep-ph]].
111. A. Park, P. Gubler, M. Harada, S. H. Lee, C. Nonaka and W. Park, Phys. Rev. D **93**, 054035 (2016), [arXiv:1601.01250 [nucl-th]].
112. P. Gubler, T. Song and S. H. Lee, Phys. Rev. D **101**, 114029 (2020), [arXiv:2003.09073 [hep-ph]].
113. T. Hilger, R. Thomas and B. Kampfer, Phys. Rev. C **79**, 025202 (2009), [arXiv:0809.4996 [nucl-th]].
114. T. F. Caramés, C. E. Fontoura, G. Krein, K. Tsushima, J. Vijande and A. Valcarpe, Phys. Rev. D **94**, 034009 (2016), [arXiv:1608.04040 [hep-ph]].
115. G. N. Zeminiani, J. J. Cobos-Martínez and K. Tsushima, [arXiv:2406.11114 [nucl-th]].
116. K. Saito, K. Tsushima and A. W. Thomas, Nucl. Phys. A **609**, 339 (1996), [arXiv:nucl-th/9606020 [nucl-th]].
117. K. Saito, K. Tsushima and A. W. Thomas, Phys. Rev. C **56**, 566 (1997), [nucl-th/9703011].
118. Y. R. Kwan and F. Tabakin, Phys. Rev. C **18**, 932 (1978).
119. P. Buhler *et al.*, Prog. Theor. Phys. Suppl. **186**, 337 (2010).
120. H. Ohnishi *et al.*, Acta Phys. Polon. B **45**, 819 (2014).
121. T. Csörgő, M. Csanád and T. Novák, Proceedings, 10th Workshop on Particle Correlations and Femtoscopy (WPCF 2014) : Gyöngyös, Hungary, August 25-29, 2014, SLAC-conf-C140825.8.
122. [https://www.jlab.org/exp\\_prog/PACpage/PAC42/PAC42\\_FINAL\\_Report.pdf](https://www.jlab.org/exp_prog/PACpage/PAC42/PAC42_FINAL_Report.pdf)
123. J. J. Cobos-Martínez and K. Tsushima, Phys. Rev. C **109**, 2 (2024), [arXiv:2308.07836 [nucl-th]].
124. J. J. Cobos-Martínez, K. Tsushima, G. Krein and A. W. Thomas, PoS CHARM2020, 041 (2021), [arXiv:2109.10995 [nucl-th]].
125. J. Cobos Martinez, K. Tsushima, G. Krein and A. W. Thomas, PoS PANIC2021, 199 (2022), [arXiv:2111.13820 [nucl-th]].

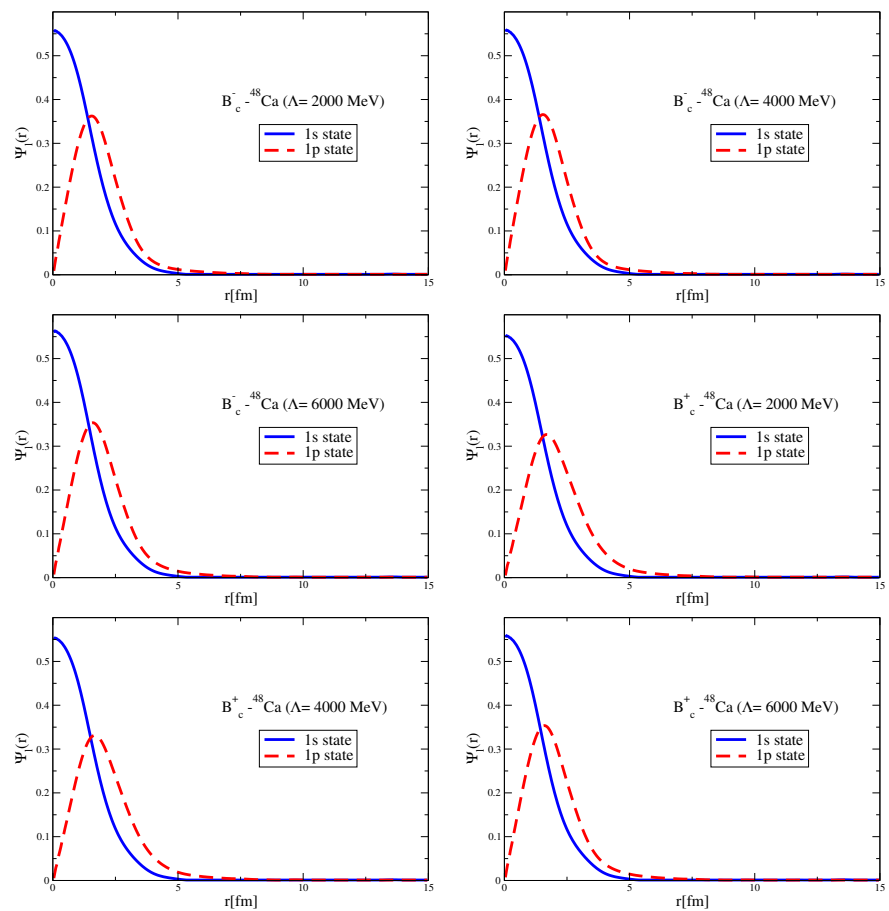


**Figure A4.** Coordinate space wave functions for the 1s and 1p states of the  $B_c^{\pm} - ^{48}\text{Ca}$  systems with the Coulomb potentials for different values of  $\Lambda$ .

126. S. Navas et al. (Particle Data Group), Phys. Rev. D **110**, 030001 (2024).

**Disclaimer/Publisher's Note:** The statements, opinions and data contained in all publications are solely those of the individual author(s) and contributor(s) and not of MDPI and/or the editor(s). MDPI and/or the editor(s) disclaim responsibility for any injury to people or property resulting from any ideas, methods, instructions or products referred to in the content.

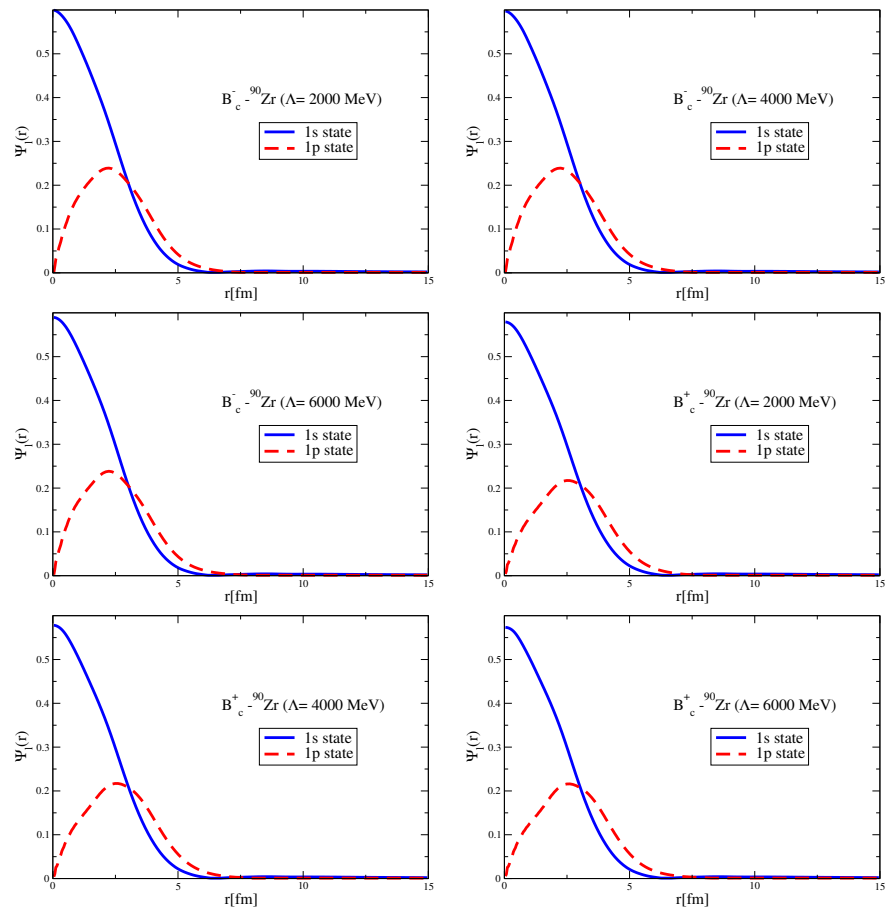


**Figure A5.** Coordinate space wave functions for the 1s and 1p states of the  $B_c^{\pm} - ^{90}\text{Zr}$  systems with the Coulomb potentials for different values of  $\Lambda$ .

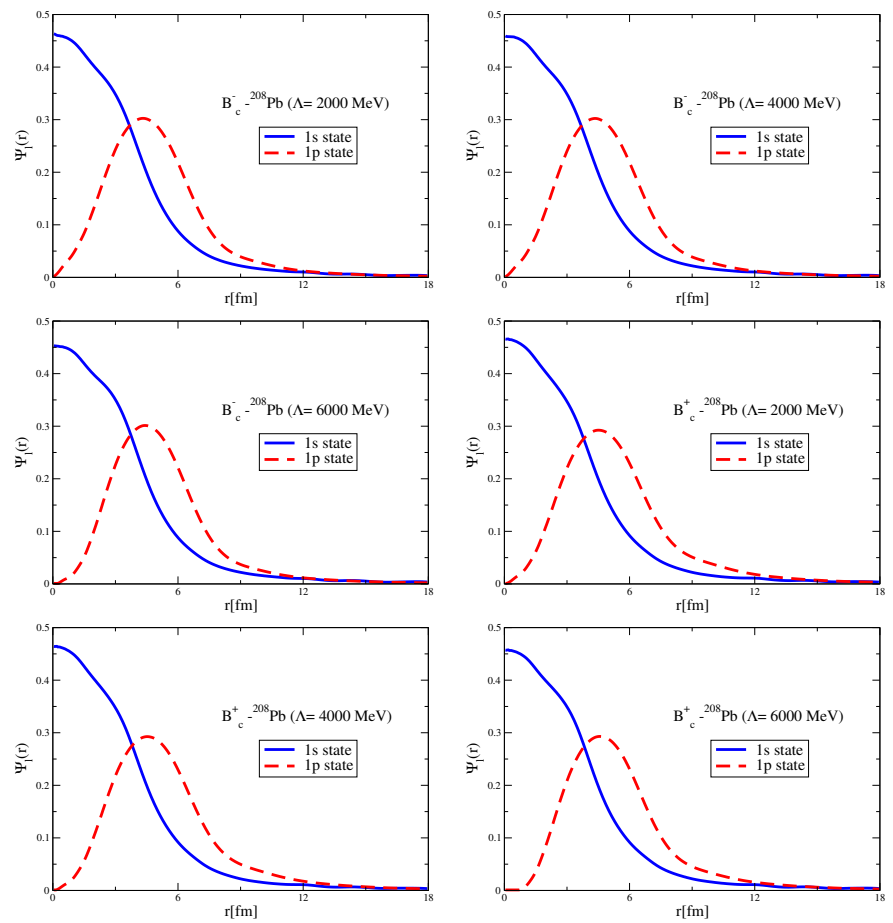


**Figure A6.** Coordinate space wave functions for the 1s and 1p states of the  $B_c^{\pm} - ^{208}\text{Pb}$  systems with the Coulomb potentials for different values of  $\Lambda$ .

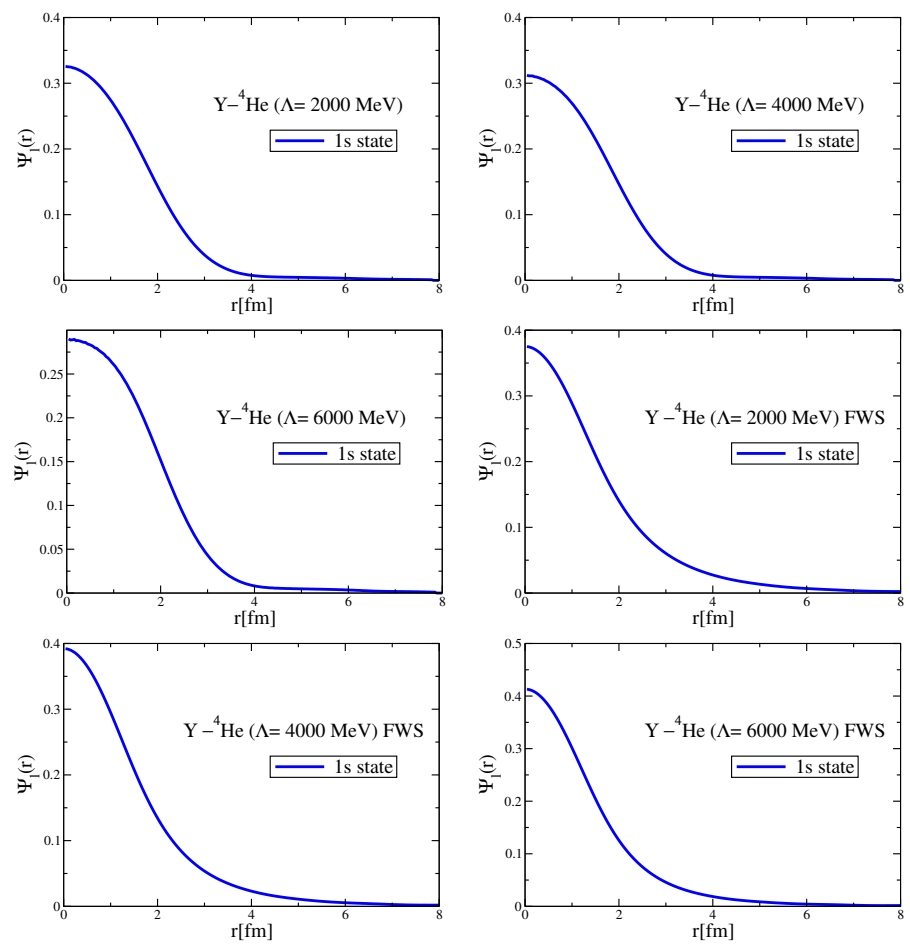


**Figure A7.** Coordinate space 1s state wave functions of the  $Y-^4\text{He}$  system for different values of cutoff  $\Lambda$ , obtained by the direct Bessel transform and by the Fourier transform of the fitted Woods-Saxon form potential (FWS).

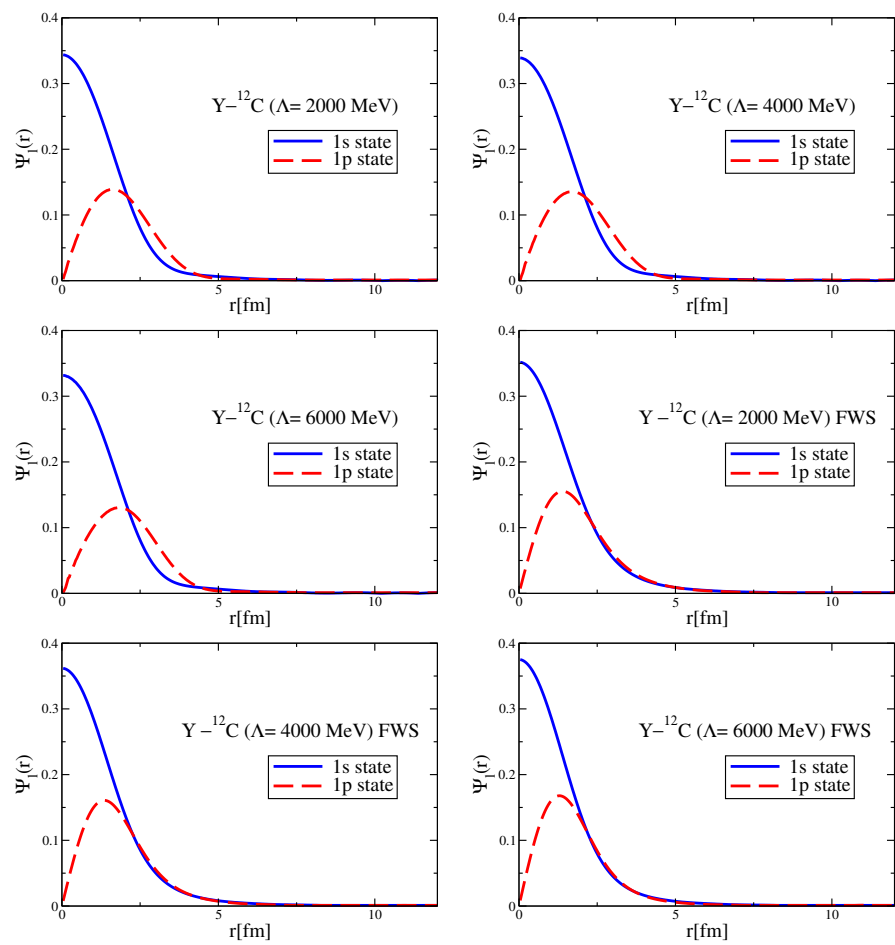


**Figure A8.** Coordinate space 1s and 1p state wave functions of the  $Y-^{12}\text{C}$  system for different values of cutoff  $\Lambda$ , obtained by the direct Bessel transform and by the Fourier transform of the fitted Woods-Saxon form potential (FWS).



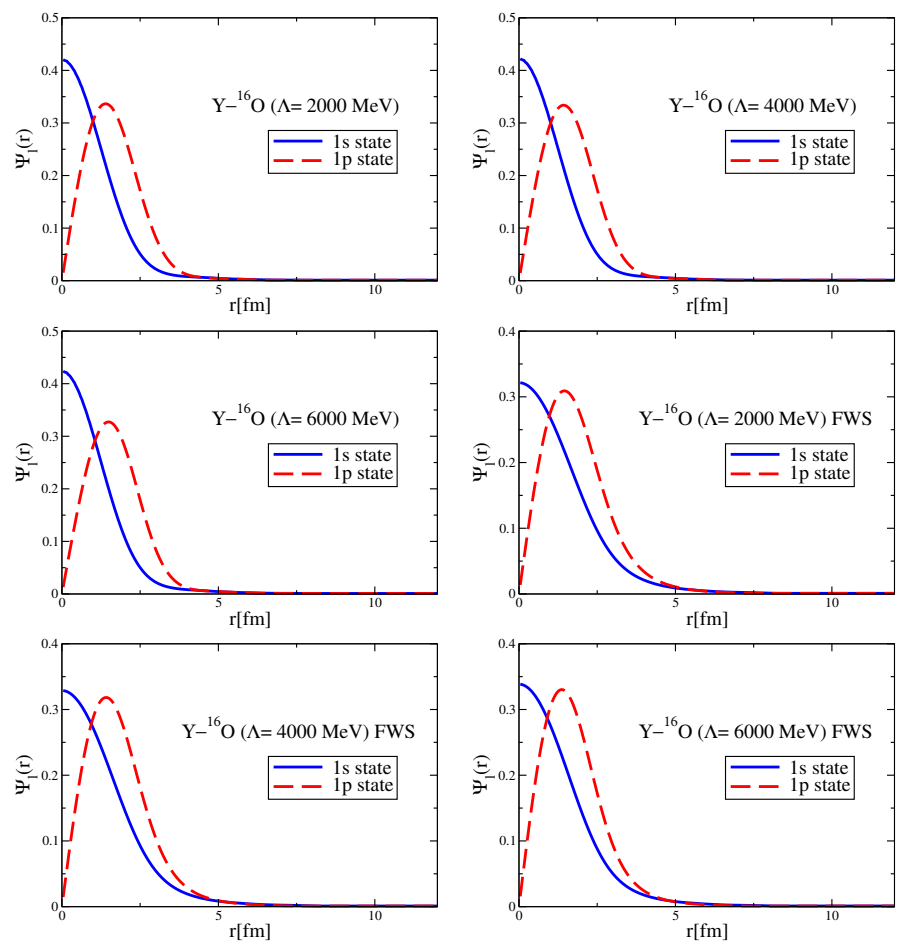


**Figure A9.** Coordinate space 1s and 1p state wave functions of the  $Y-^{16}\text{O}$  system for different values of cutoff  $\Lambda$ , obtained by the direct Bessel transform and by the Fourier transform of the fitted Woods-Saxon form potential (FWS).

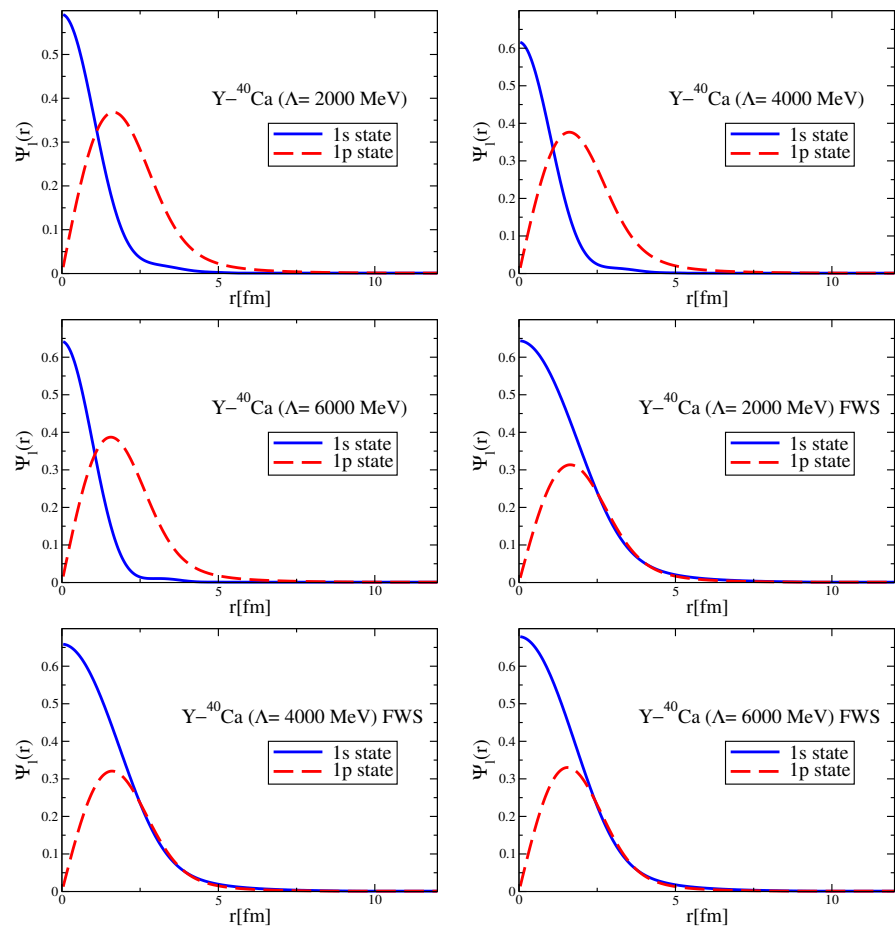


**Figure A10.** Coordinate space 1s and 1p state wave functions of the  $Y-^{40}\text{Ca}$  system for different values of cutoff  $\Lambda$ , obtained by the direct Bessel transform and by the Fourier transform of the fitted Woods-Saxon form potential (FWS).

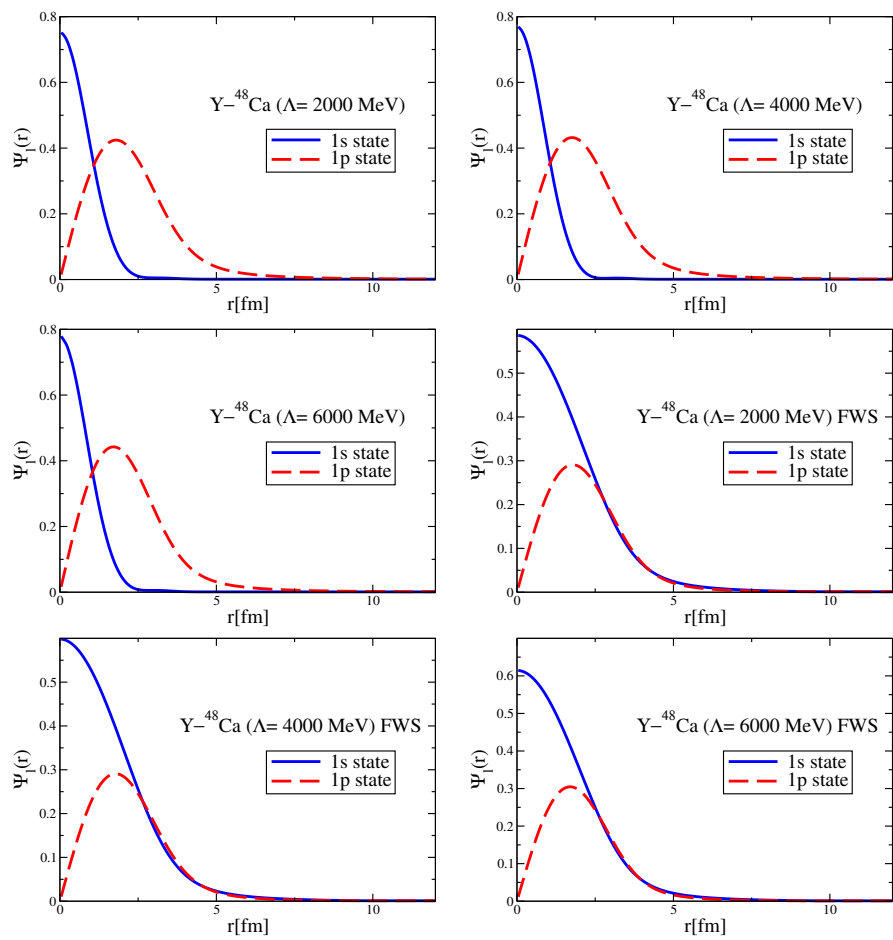


**Figure A11.** Coordinate space 1s and 1p state wave functions of the  $Y-^{48}\text{Ca}$  system for different values of cutoff  $\Lambda$ , obtained by the direct Bessel transform and by the Fourier transform of the fitted Woods-Saxon form potential (FWS).

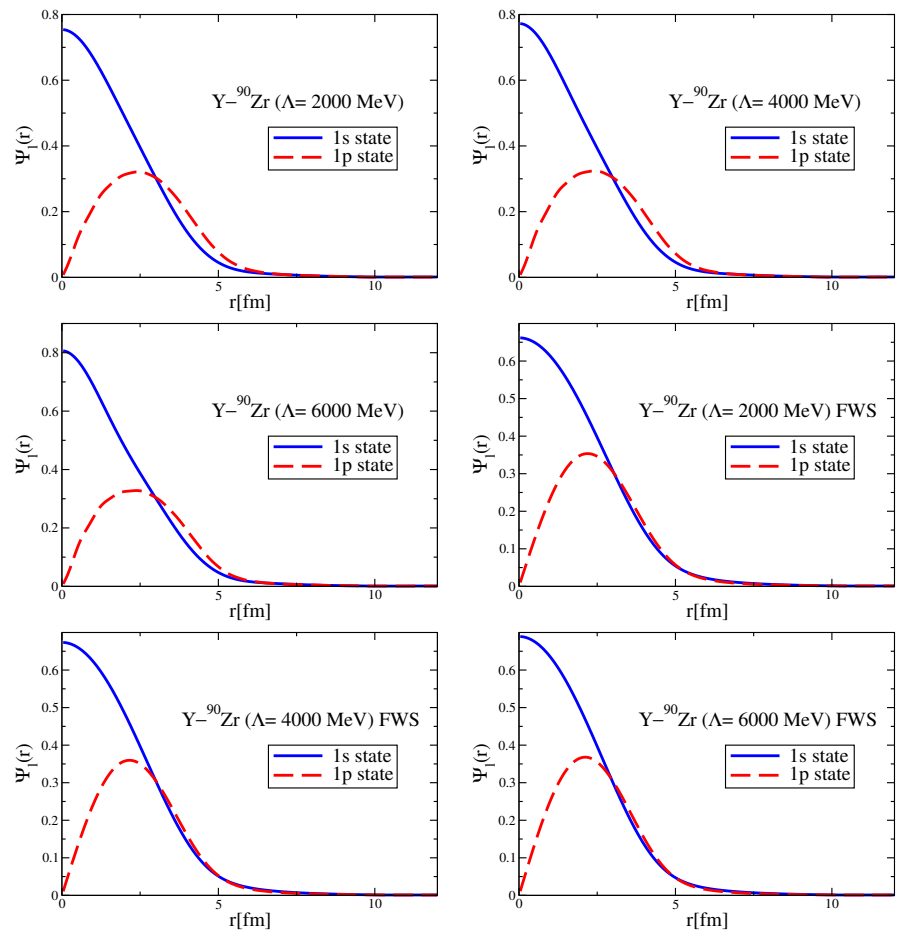


**Figure A12.** Coordinate space 1s and 1p state wave functions of the  $Y-^{90}\text{Zr}$  system for different values of cutoff  $\Lambda$ , obtained by the direct Bessel transform and by the Fourier transform of the fitted Woods-Saxon form potential (FWS).

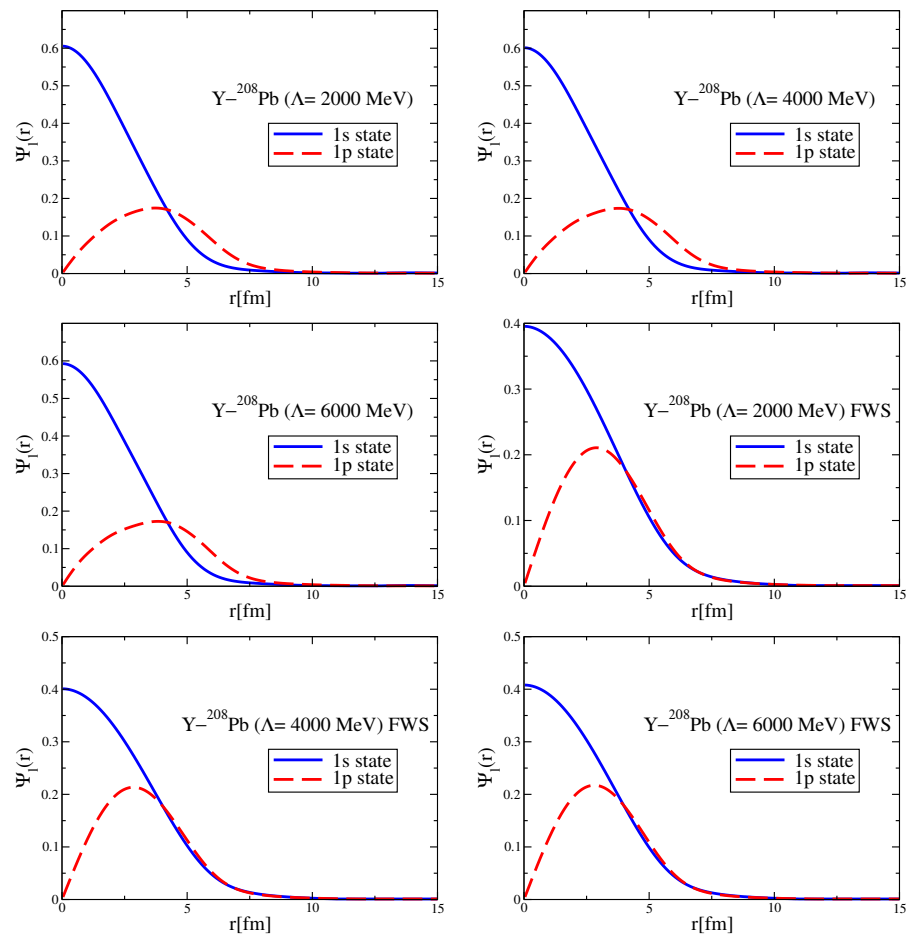


**Figure A13.** Coordinate space 1s and 1p state wave functions of the  $Y-^{208}\text{Pb}$  system for different values of cutoff  $\Lambda$ , obtained by the direct Bessel transform and by the Fourier transform of the fitted Woods-Saxon form potential (FWS).

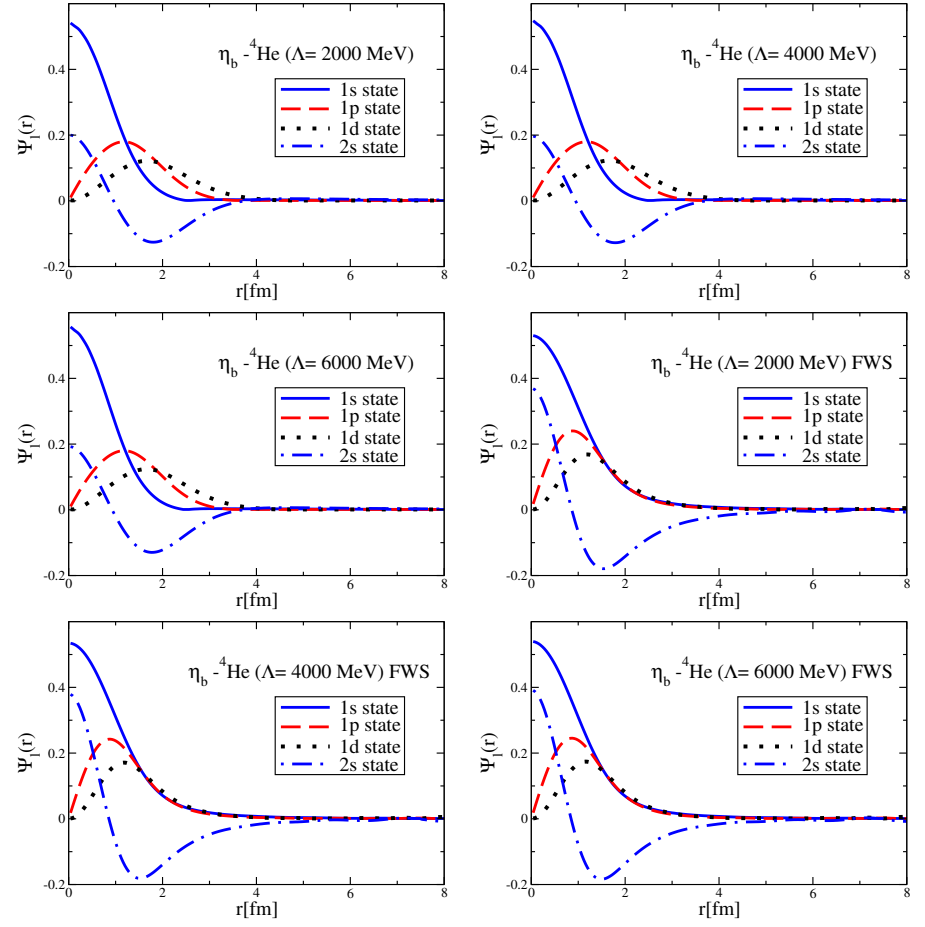


**Figure A14.** Coordinate space wave functions for the 1s to 2s states of the  $\eta_b$ - ${}^4\text{He}$  system for different values of cutoff  $\Lambda$ , obtained by the direct Bessel transform and by the Fourier transform of the fitted Woods-Saxon form potential (FWS).

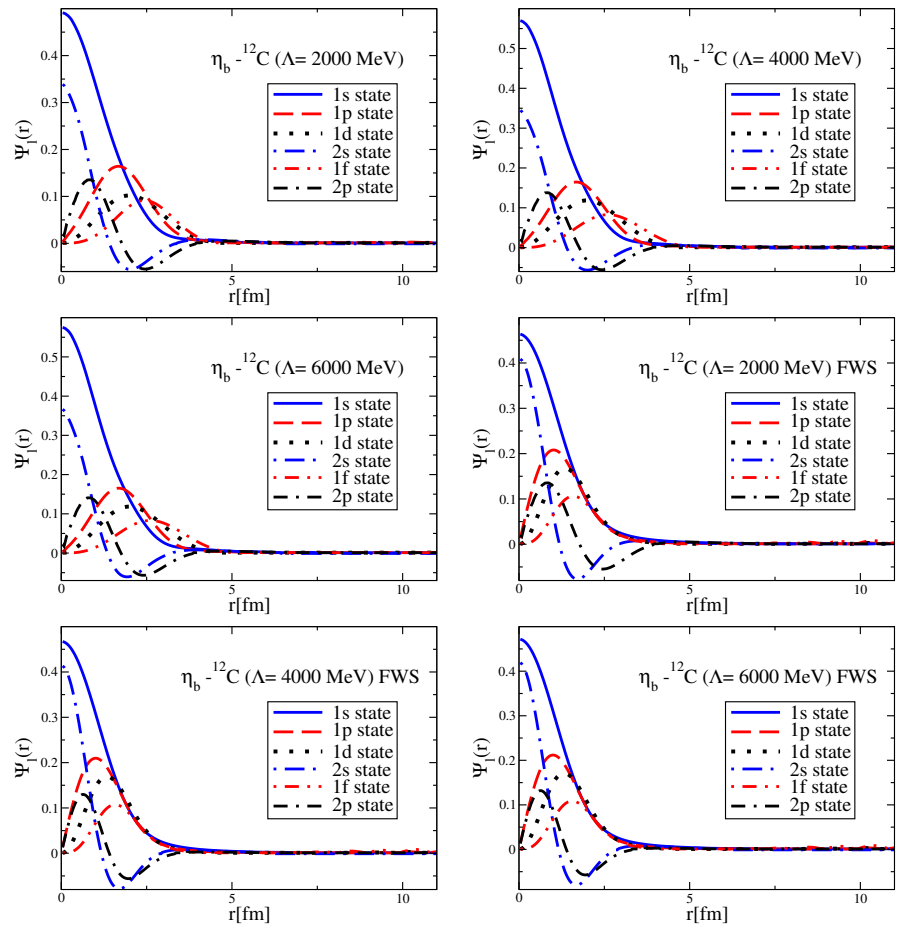


**Figure A15.** Coordinate space wave functions for the 1s to 2p states of the  $\eta_b$ - $^{12}\text{C}$  system for different values of cutoff  $\Lambda$ , obtained by the direct Bessel transform and by the Fourier transform of the fitted Woods-Saxon form potential (FWS).



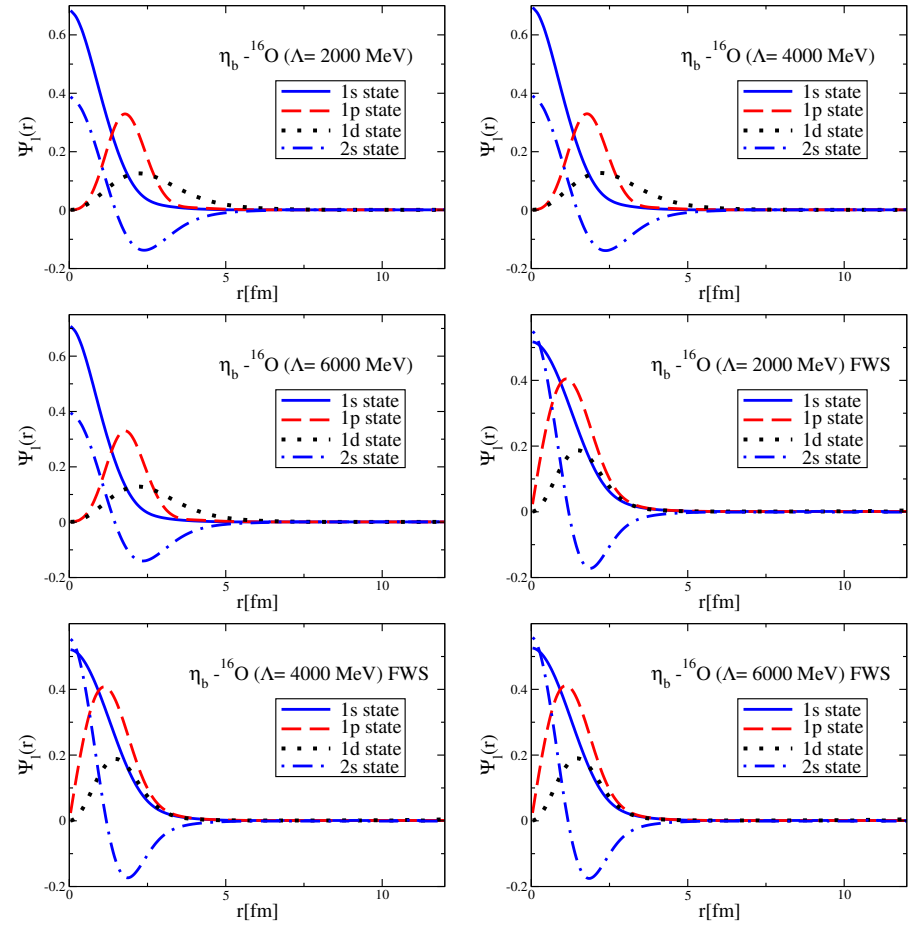


**Figure A16.** Coordinate space wave functions for the 1s to 2s states of the  $\eta_b$ - $^{16}\text{O}$  system for different values of cutoff  $\Lambda$ , obtained by the direct Bessel transform and by the Fourier transform of the fitted Woods-Saxon form potential (FWS).

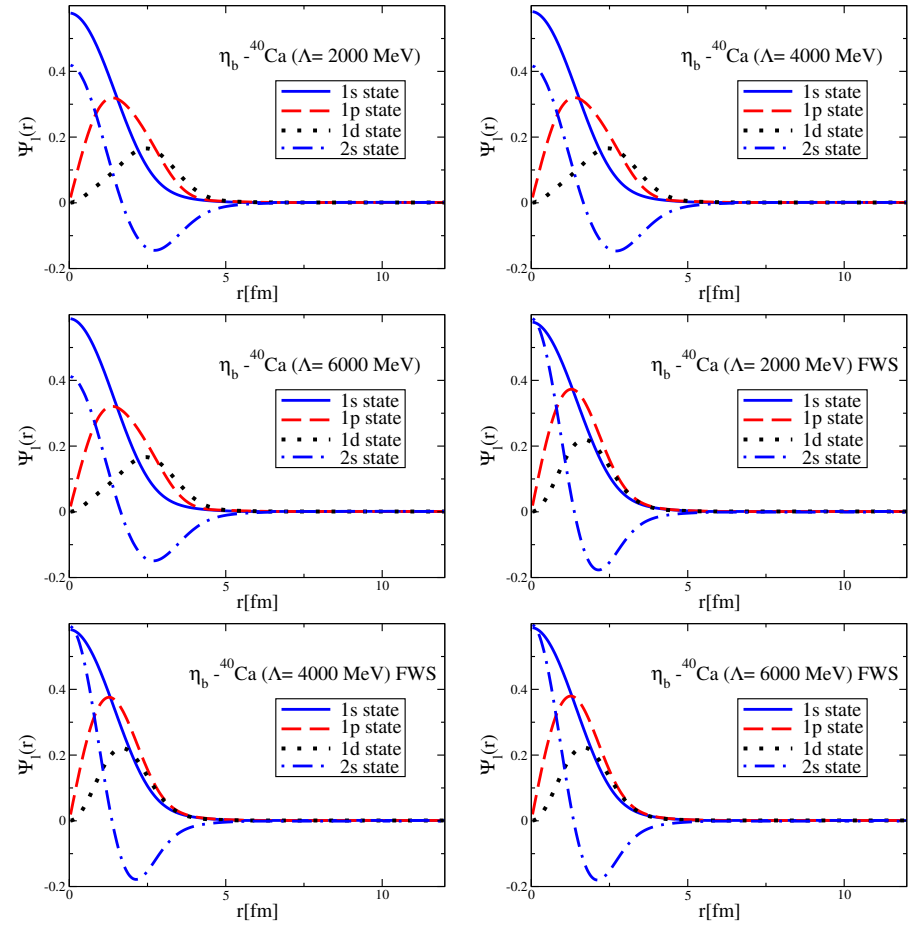


**Figure A17.** Coordinate space wave functions for the 1s to 2s states of the  $\eta_b$ - $^{40}\text{Ca}$  system for different values of cutoff  $\Lambda$ , obtained by the direct Bessel transform and by the Fourier transform of the fitted Woods-Saxon form potential (FWS).

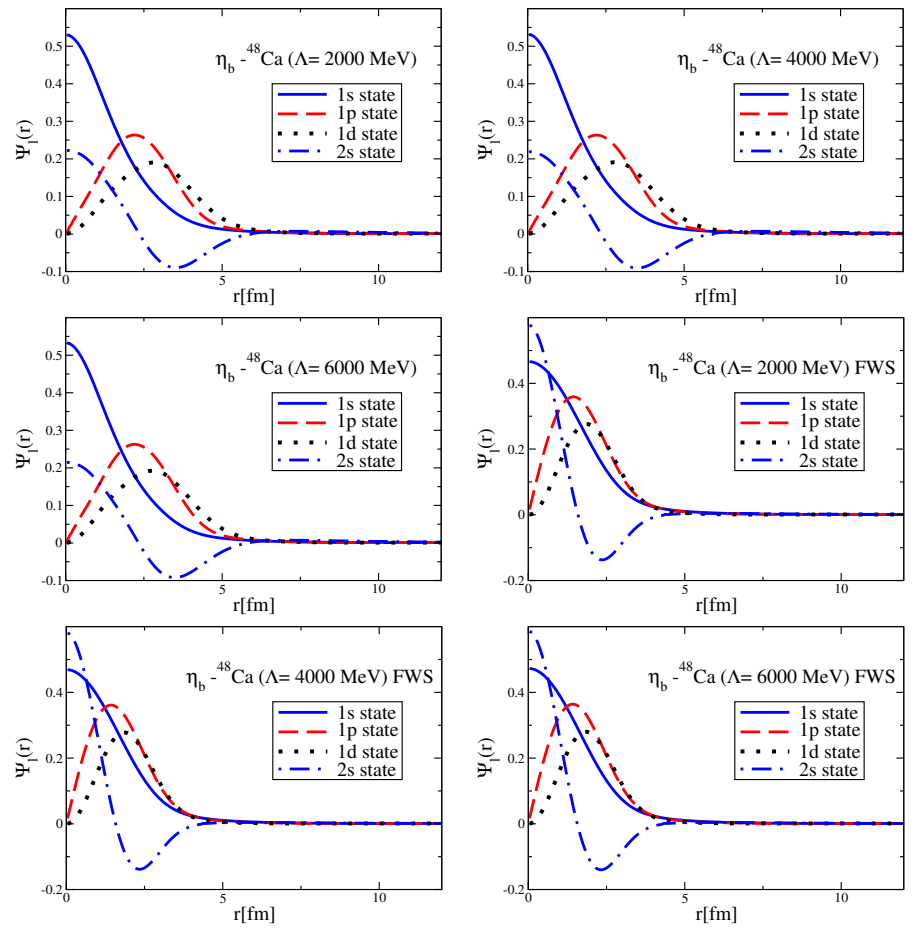


**Figure A18.** Coordinate space wave functions for the 1s to 2s states of the  $\eta_b - {}^{48}\text{Ca}$  system for different values of cutoff  $\Lambda$ , obtained by the direct Bessel transform and by the Fourier transform of the fitted Woods-Saxon form potential (FWS).

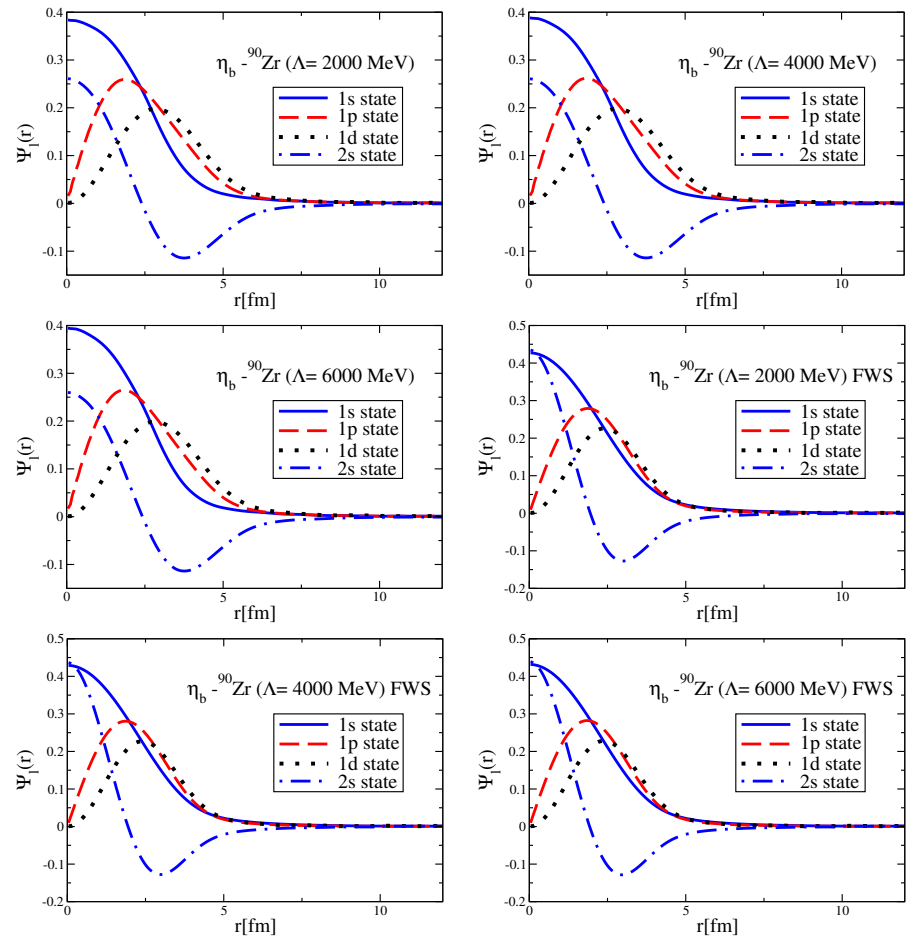


**Figure A19.** Coordinate space wave functions for the  $1s$  to  $2s$  states of the  $\eta_b^- {}^{90}\text{Zr}$  system for different values of cutoff  $\Lambda$ , obtained by the direct Bessel transform and by the Fourier transform of the fitted Woods-Saxon form potential (FWS).

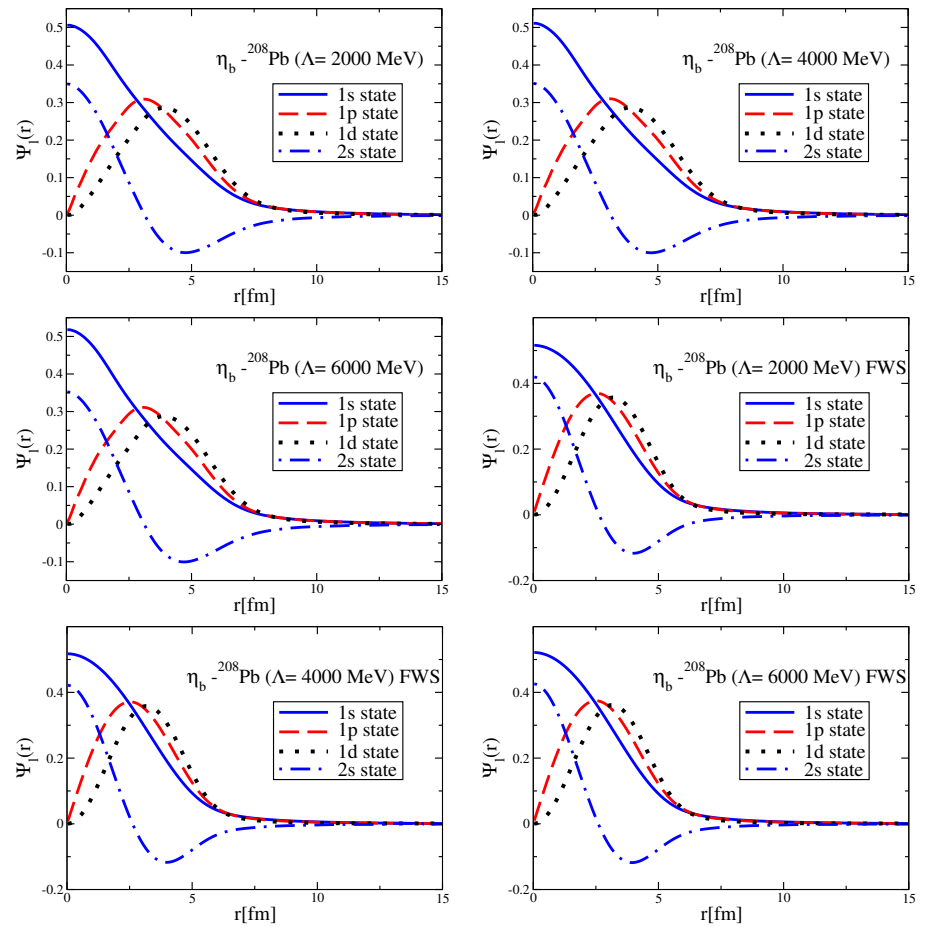


**Figure A20.** Coordinate space wave functions for the 1s to 2s states of the  $\eta_b^-$ - $^{208}\text{Pb}$  system for different values of cutoff  $\Lambda$ , obtained by the direct Bessel transform and by the Fourier transform of the fitted Woods-Saxon form potential (FWS).